UiO : Department of Mathematics
University of Oslo

Normal Pressure with Abnormal Geometry

A Biomechanical Model of Normal Pressure Hydrocephalus During Infusion Tests

Lars Willas Dreyer

Master's Thesis, Spring 2022

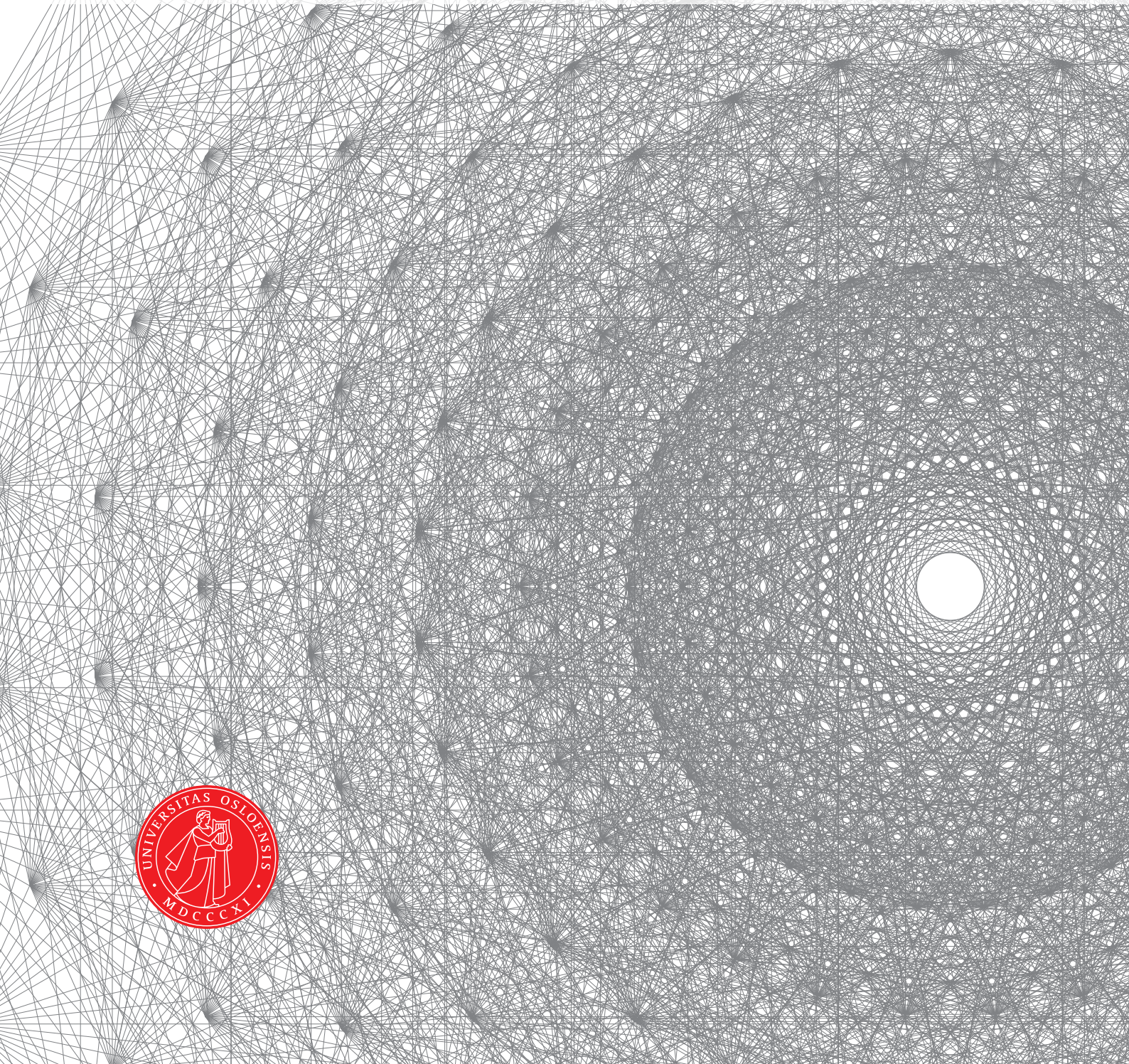

This master's thesis is submitted under the master's programme *Mechanics*, with programme option *Mechanics*, at the Department of Mathematics, University of Oslo. The scope of the thesis is 60 credits.

The front page depicts a section of the root system of the exceptional Lie group E_8, projected into the plane. Lie groups were invented by the Norwegian mathematician Sophus Lie (1842–1899) to express symmetries in differential equations and today they play a central role in various parts of mathematics.

Abstract

Normal pressure hydrocephalus is a variant of reversible dementia. The symptoms manifest themselves in the form of urinary incontinence, gait disturbance and dementia, and it is estimated that at least 22 out of 100 000 people in Norway are afflicted with the disease. In this thesis, a biomechanical model of idiopathic normal pressure hydrocephalus (iNPH) is implemented. We treat the brain as a porous and continuous medium with seven interconnected and fluid filled porous compartments. Our model is based on the MPET framework of Tully and Ventikos (2011) and is implemented to simulate how the brain reacts to an infusion test.

We generate patient specific meshes for 47 patients using MRI images taken by the group of Anders Eklund at Umeå University. In addition, we compute the average fluid pressure, average pore speed for each compartment, and the total inter-compartmental fluid transfer between all connected compartments.

Two sets of simulations are performed, one investigating the effect of brain geometry alone, and another where experimental measurements are included to allow for patient specific boundary conditions. Brain geometry is found to have little effect on the overall results, with average compartmental pressure, fluid velocity and transfer rate being on average less than 10 % different between control and iNPH groups for most compartments. Enforcement of patient specific boundary conditions is, however, shown to be vital, as the variations in all quantities of interest are great both within and across groups when the personalised boundary conditions are applied.

Acknowledgements

Working with the physics of the human brain has been my goal from my first week at the university, and the work with this thesis did not disappoint. It was the most fun, and also most stressful project I have ever worked on. I therefore wish to thank all those who helped me, either emotionally, academically or socially during these past two years.

First, I would like to thank Vegard Vinje for his patience and help these past two years. I could not ask for a better supervisor. Our discussions where always interesting, and your interest and support has been greatly appreciated. Kent-André, you always showed great interest in my work and progress, and your insight was of great help in my work. I would also like to thank Marie for welcoming me to Simula, and for introducing me to the biomechanics of the brain. Finally, many thanks to Karen-Helene Støverud for all the help with brain segmentation and for the good feedback and suggestions, and to Anders Eklund for the permission to use the MRI images and infusion data.

A special thanks goes to Ingrid Dæhlen. Without her support both with proofreading, assurance and patience with long tirades about biomechanics, would not be the same. While the details surrounding numerical solutions of yet another differential equation might not be an exciting thriller, you still listened and that patience was greatly appreciated. Many thanks to my study hall mates at B901 and Simula, my friends, and my fellow master's students in fluid mechanics. The past two years would only have been half as fun without you.

Finally, I would like to thank Håkon, Liv, Bjørn and Harald. You are, and have always been, a great a family to grow up in, and without your help and support I would not have been where I am today. Thank you all for your proofreading, support and skoleboller.

Last but not least, thanks to Lånekassen for allowing me to enjoy six great years at the University of Oslo.

Contents

Abstract i

Acknowledgements ii

Contents iii

1 Introduction 1
- 1.1 Outline . . . 4
- 1.2 List of abbreviations . . . 5
- 1.3 Notation . . . 6

2 Biomedical Background 7
- 2.1 The anatomy of the brain . . . 7
- 2.2 Normal pressure hydrocephalus . . . 10

3 Notation and Mathematical Foundations 13

4 Mathematical Model of the Brain 17
- 4.1 Governing equations . . . 17
- 4.2 The weak formulation . . . 22
- 4.3 Input data and uncertainties . . . 23
- 4.4 Implementing patient specific data . . . 28
- 4.5 Output quantities . . . 30
- 4.6 Software and implementation. . . . 32

5 Meshing 33

6 Model verification 38
- 6.1 Resolution sensitivity tests . . . 38
- 6.2 Sensitivity to changes in arterial inflow . . . 42

7 Results 44
- 7.1 Results under one model . . . 44
- 7.2 Patient specific boundary conditions . . . 58

8 Discussion 74
- 8.1 Summary of results . . . 74
- 8.2 Our results in context . . . 75

8.3 Limitations and further work 83
8.4 Conclusion 85

List of Figures **87**

List of Tables **89**

Bibliography **91**

CHAPTER 1

Introduction

In 1965 the neurologists Salomòn Hakim and Raymond Delacy Adams described a new form of dementia which they named *Normal Pressure Hydrocephalus*, commonly abbreviated as NPH. Hakim and Adams (1965) described the treatment and disease progression of three patients with similar symptoms. In all cases, the afflicted individuals showed a severe reduction in cognitive ability and language capabilites. In addition, urinary incontinence and severely reduced mobility was observed. Out of these three, two of the patients developed the symptoms shortly after a traumatic head injury. The most intriguing case, however, was that of the remaining individual, a middle-aged trombonist whose condition gradually worsened over a longer time period. The patient had not suffered any identifiable head trauma. Still, like the two other patients, he responded well to treatment. Hakim and Adams observed a drastic, but temporary, alleviation of symptoms when the patients were drained of cerebrospinal fluid (CSF), a water-like liquid surrounding our central nervous system. Because of this, they tried to operate in a tube, called a ventricular shunt, connecting the lateral ventricles to the stomach. The aim was aiding CSF clearance from the brain. All patients responded positively.

The term normal pressure hydrocephalus stems from the, perhaps surprisingly, normal intercranial pressure values in afflicted individuals. For iNPH patients, the CSF resting pressure is almost at the same level as for healthy persons, with an average resting pressure difference baseline of about 5 mmHg and a high interpersonal variance (Malm, Kristensen et al. (1995)). The disease is usually divided into two categories, as explained by Malm and Eklund (2006). Two of the patients described by Hakim and Adams had identifiable causes for the development of NPH, and are therefore patients with secondary NPH, abbreviated sNPH. The trombonist, however, due to the unknown origin of his affliction would be the first reported case of *idiopathic normal pressure hydrocephalus*, commonly abbreviated as iNPH. Of these two variants, we will focus on iNPH as we are in possession of experimental data on 14 iNPH patients. The disease usually manifests itself with the triad of symptoms explained in the previous paragraph, and the most dominant change to the brain tissue is significantly enlarged ventricles. Furthermore, Lindstrøm et al. (2018) provides evidence indicating increased CSF flow from the ventricles compared to healthy adults.

The significance of the CSF on our brain health has recently been a topic of great interest in the scientific community. Iliff, M. Wang, Liao et al. (2012) demonstrated that tracers injected into the cerebrospinal fluid of rats entered

the brain at a rate far quicker than what could be attributed to diffusion alone. They proposed that convective flow in the CSF and the interstitial fluid (ISF), constitute a system for clearance of waste products from the brain. This system, dubbed the glymphatic system has since been corroborated by several authors, e.g. Xie et al. (2013), Ringstad et al. (2018), Mestre et al. (2018) and Raghunandan et al. (2021). The exact specifics of the glymphatic hypothesis has changed from the original article, and the current belief of the scientific community seem to converge towards a view where waste is cleared diffusively from the brain interstitium into the perivascular spaces of the brain, through which they are carried out by convective CSF flow, see Abbott et al. (2018), Hablitz and Nedergaard (2021) and Chong et al. (2022). The disease of normal pressure hydrocephalus is believed to disturb the glymphatic system. P. K. Eide, L. M. Valnes et al. (2021) document that CSF clearance from a region in the grey matter, the outermost layer of the brain, is delayed in iNPH patients. The aforementioned article of Lindstrøm et al. (2018) found significant disturbances in the CSF flow from the ventricles in iNPH patients.

Hakim and Adams (1965) treated their patients by a ventricular shunt and reported positive results. It has, however, been shown that far from all patients with NPH benefit from shunt surgery. Vanneste et al. (1992) reported that only 15% experienced significant improvement post operation. Furthermore, the Cochrane review of Esmonde and Cooke (2002) concluded with there being no evidence for the efficacy of shunt surgery in the treatment of NPH. The systematic review done by Toma et al. (2013), however, concluded that shunt surgery is effective and safe if the patients are screened properly, and Williams et al. (2022) reported significant post-operative improvement one year after surgery in a treatment group of 193 patients. Recently, Andrén et al. (2021) found that 40 % of patients who had to wait for more than 6 months before getting shunt surgery, died during the following four years. In the group who were treated only three months after screening, the mortality was reduced to 10 % in the same period. The need for preoperative screening is stressed in most articles that find improvement after surgery. For instance, the meta-analysis of Peterson et al. (2016) found that shunt surgery was the most effective treatment for iNPH. Their analysis gives an explanation for why many observe little to no improvement after surgery, namely methodological errors such as poor selection criteria, inconsistent post-operative follow up with subjective, and unclear improvement metrics. As such, good selection criteria are important to reduce the risk of surgery without benefit.

The most common way to select patients for shunt surgery today is by infusion tests. In infusion tests, the intracranial pressure (ICP) is first measured at rest. Then, a CSF-like liquid is injected at a constant rate into the spinal canal until the system reaches a new equilibrium. Thereafter, it is possible to compute the outflow resistance R_{out} by dividing the pressure increase by the infusion rate. Screening by infusion test has been showed to work well. Ryding, Kahlon and Reinstrup (2018) found that 86 % of patients whose infusion test plateaued in the interval of 22 to 37 mmHg had a significantly improved walk speed post operation. In their meta-analysis, Thavarajasingam et al. (2021) concluded while more accurate diagnostic methods exist, the accessibility of infusion tests makes them an ideal first test to screen patients for operation.

Infusion tests only measure the CSF pressure in the spine and subarachnoid space (SAS), and gives little information about what happens deeper into

the brain parenchyma. There are many observations of how CSF enters the brain, with the leading hypothesis being that it is transported mainly through small channels around the cerebral blood vessels called perivascular spaces (PVS). The review paper of Abbott et al. (2018) concludes that the brain most likely clears waste through perivascular flow. Mestre et al. (2018) and Raghunandan et al. (2021) both showed convective transport in the perivascular spaces of surface cerebral blood vessels in mice. Lastly Pizzo et al. (2018) found that tracer injected into the CSF entered deep into the brain itself alongside perivascular pathways. Hence, the fact that the brain communicates with the spinal and subarachnoid CSF is uncontroversial and widely documented. We would therefore expect the waterscape within the brain to be affected during an infusion test. It is, however, hard to measure how the brain is affected experimentally. As a result, other methods have to be employed to find plausible explanations for how the brain is affected by an infusion test.

A popular method for filling the gaps of experimental data is biomechanical modelling. This approach has been shown to give convincing explanations for some of the mechanisms of the waterscape of the brain. A short, and by no means exhaustive list of examples is: Dutta-Roy, Wittek and Miller (2008), who used poroelastic modelling to investigate the formation of ventriculomegaly in NPH patients. In their article Holter et al. (2017) computed the flow rate in the extracellular space with realistic geometries. Furthermore, Tully and Ventikos (2011) proposed that multiple network poroelastic theory (MPET) could be used to model NPH. Recently, Tithof et al. (2022) computed the pressure gradients needed to reproduce perivascular flow in cerebral blood vessels. Kedarasetti, Drew and Costanzo (2021) used poroelastic theory to find that neuron-activated dilation of cerebral arteries could induce bulk flow in the extracellular space of the brain. Finally, Guo, Vardakis et al. (2020) used multiple network poroelastic theory (MPET) to demonstrate how blood perfusion is reduced in subjects who smoke. The topic of infusion tests have also been a popular topic for biomechanical modelling. Vinje et al. (2020) who developed a model for explaining how CSF clearance routes changed during an infusion test. Vallet et al. (2020) who used statistical analysis to investigate the link between NPH and frailty. Sobey et al. (2010) who modelled the effect of arterial pulsation on classical infusion tests. Finally, Mládek et al. (2022) who used machine learning to help predict which patients would benefit from shunt surgery based on the results of an infusion test.

Despite all the progress and insight obtained by the aforementioned work, an investigation of how the brain itself responds to infusion testing has not been done on a three dimensional domain. We will in this thesis attempt to fill this gap, using a modified MPET model on patient specific geometries. Our analysis will be based on measurements of 47 infusion tests done by the research group of professor Anders Eklund at Umeå University. These patients are divided into two groups, with 33 healthy individuals constituting the control group and 14 individuals diagnosed with iNPH. The dataset consists of full MRI scans of the brain of each subject, the quantities measured during an infusion test and measurements of cerebral blood flow in each patient. The results from the infusion test were published in Qvarlander et al. (2017). We will use this data to compute the pressures in the extracellular space of the brain, as well as the CSF pressure in the PVS and the vascular pressures within the brain. To our knowledge, simulations of infusion tests on this scale has not been performed

before. We will implement our model using a modified version of the MPET framework of Tully and Ventikos (2011), where we have split their combined CSF and ECS compartment into four separate compartments, namely three PVS compartments and one ECS compartment.

Having both patient specific geometries and experimental data for boundary conditions allows us to tailor our model with a higher degree of accuracy than what has been previously done. We investigate whether the changed geometry between control- and iNPH groups affect the flow of CSF and ISF within the brain. In particular, how our computed flow compare to experimental work such as Raghunandan et al. (2021) or numerical simulations like Tithof et al. (2022) and Holter et al. (2017). We also aim to find a model which gives a plausible explanation of why the groups respond differently to infusion, and lastly if a mechanistic approach is suitable to model the disease.

1.1 Outline

Our thesis is structured in the following manner:

- **Chapter 2: Biomedical background** - In this chapter we give a short overview of the anatomy of the human brain, what cerebrospinal and interstitial fluid is, their importance in brain function and what normal pressure hydrocephalus is.
- **Chapter 3: Mathematical background** - The chapter is dedicated to giving a brief summary of partial differential equations, and how to solve one using the finite element method.
- **Chapter 4: The mathematical model of the brain.** - This chapter is where we explain the model we implemented, how we arrived at the chosen values for each parameter, how we can modify the model and how it was implemented.
- **Chapter 5: Meshing** - Here we discuss the meshing procedure in detail. Starting with how the data was controlled to ensure a correct representation of the geometry, then how the meshes were generated before finally discussing which steps we took to verify the meshes.
- **Chapter 6: Model verification** - This chapter is dedicated to presenting the results and methodology we used to verify our model. We tested the model's sensitivity to mesh resolution, time resolution, change in input parameters and order of finite element basis polynomials.
- **Chapter 7: Main findings** - Here we present our main results from our simulation. We start by showing the results for when the boundary conditions are the same for both control and iNPH, and the applied CSF pressure remains the same for both groups. Then, we show how these results change if we also apply a patient specific intercranial pressure conditions.
- **Chapter 8: Discussion and conclusion** - In this final chapter, we summarise our results and discuss if they seem plausible with comparisons to existing literature. We also discuss the implications and uncertainty

associated with the results. Finally, we evaluate the limitations of the model and present possible extensions and modifications for future work.

1.2 List of abbreviations

Here we give a short list over the most common and important abbreviations used in the thesis, as well as a short description of what each listed element is.

- **BBB** - Blood-brain barrier. A semi-permeable membrane regulating what substances that can leave and enter the brain parenchyma through the vascular system.
- **CBV** - Cerebral Blood Volume. Volume of blood in the human brain.
- **CBVf** - Cerebral Blood Volume fraction. The fraction of the total brain volume occupied by blood.
- **CG**n - Lagrange interpolation polynomials of order n. These are the basis functions we use to represent our numerical solution.
- **CSF** - Cerebrospinal fluid. A water-like liquid which surrounds the human brain and spinal cord.
- **DS** - Dural Sinus. Channels through which venous blood leave the brain. Located at the top of the head.
- **ECS** - Extracellular space. The space between cells in the brain parenchyma.
- **FEM** - Finite Element Method. A numerical method for finding weak solution of PDEs.
- **ICP** - Intracranial pressure. Pressure of the cerebrospinal fluid in the spine and in the subarachnoid space.
- **ISF** - Interstitial fluid. This is a water-like liquid which fills the extracellular space.
- **MPET** - Multiple network PoroElastic Theory. A set of equations descriving flow in and deformation of a porous and elastic continuum containing multiple communicating pore networks. In this thesis, we will consider the brain through this framework.
- **NPH** - Normal Pressure Hydrocephalus. A variant of dementia characterised by the almost normal intracranial pressure and increased volume of cerebrospinal fluid in the lateral ventricles of the brain. Comes in two variants: secondary NPH, or sNPH, where the cause is known, and idiopathic NPH, iNPH, where the cause is unknown. Our thesis is mainly concerned about the latter.
- **PDE** - Partial Differential Equation. An equation relating a function f to its derivatives.
- **PVS** - Perivascular space. Thin CSF-filled channels surrounding the cerebral vascular system.

- **RP**n - Resolution Parameter of n. A parameter used by the meshing software SVMTK, which sets an upper limit on the mesh's cell size.
- **SAS** - Subarachnoid space. A CSF-filled space between the pia mater and arachnoid mater. This is the area we believe perivascular CSF flows from and back into.

1.3 Notation

In this thesis, we will denote a vector, $\mathbf{v}$ with bold font. Unit vectors $\hat{\mathbf{n}}$ are denoted with a bold font and a hat. In our notation for integrals, we use $d\mathbf{x}$ to indicate a volume integral. If we use a dS, then the integral is a surface integral, and if the integral ends with a dx or dt, then it is an integral with respect to a single variable.

CHAPTER 2

Biomedical Background

The topic of this thesis is the disease of *idiopathic normal pressure hydrocephalus*, or iNPH for short. Our work takes a mathematical approach, with focus on numerical simulations and biomechanical modelling. Such analyses are, however, less interesting without a proper understanding of the medical context. Before discussing the mathematics and biomechanics of our model, we will therefore give some physical and medical context.

The aim of this chapter is to explain in detail what iNPH is, in addition to the current medical knowledge on the topic. To do so, we will start in Section 2.1 by reviewing basic properties of the human brain. In particular, we will give an overview of its dimensions and how the different fluids in the brain interact. Additionally, we will discuss the medical significance of the latter. In Section 2.2, we will use this background to discuss the condition of iNPH and how it relates to the fluid flows of the human brain. Here we will discuss what characterises the disease as well as its relation to the fluid interactions in the brain.

2.1 The anatomy of the brain

The human brain is the largest part of the human nervous system, and acts as the controlling organ of the human body. The average brain is around 15 cm long and 10 cm wide and tall. The outermost layer of the brain is called the grey matter, which in the average human is 2.5 mm thick (Winkler et al. (2010)). Behind the grey matter lies the white matter, a collection of neurons transmitting signals from the grey matter to the rest of the nervous system. Within the white matter lies the ventricles, two lateral ventricles in either hemisphere, a connecting third ventricle and a fourth ventricle travelling down towards the spine. The ventricles are filled with a water-like liquid called cerebrospinal fluid CSF. Classical theory states that the CSF is produced in the choroid plexus within the ventricles (Deisenhammer et al. (2015)), although this notion has later been challenged. The review article of Brinker et al. (2014) discards choroid plexus as the centre for CSF production, and instead proposes that CSF is produced through filtration through the blood-brain barrier (BBB) in the cerebral capillaries. In a healthy adult, the human brain contains 90 to 150 ml of CSF, where 30 ml reside in the subarachnoid space (SAS) of the brain. (Deisenhammer et al. (2015)) The SAS is a thin layer lying between the pia mater and arachnoid mater, two thin membranes protecting the brain. An

illustration of how CSF is believed to circulate is shown in Figure 2.1.

The brain gets its nutrients from the blood through cerebral arteries and enters the brain at a rate of about 700 ml/min in healthy adults (Qvarlander et al. (2017)). The blood does, however, not interact directly with the brain tissue, the parenchyma. Fluid exchange between blood vessels and the parenchyma is regulated by the BBB. The barrier is a semi-permeable membrane made up from endothelial cells surrounding the the capillary walls in the brain. In healthy individuals the BBB acts as an effective regulator of what enters and leaves the brain through the blood stream. See Barichello (2019) for a comprehensive overview of the blood-brain barrier. Around both surface and penetrating blood vessel there exist a thin CSF filled space called the perivascular spaces. These spaces are believed to play an integral role in maintaining a healthy brain environment.

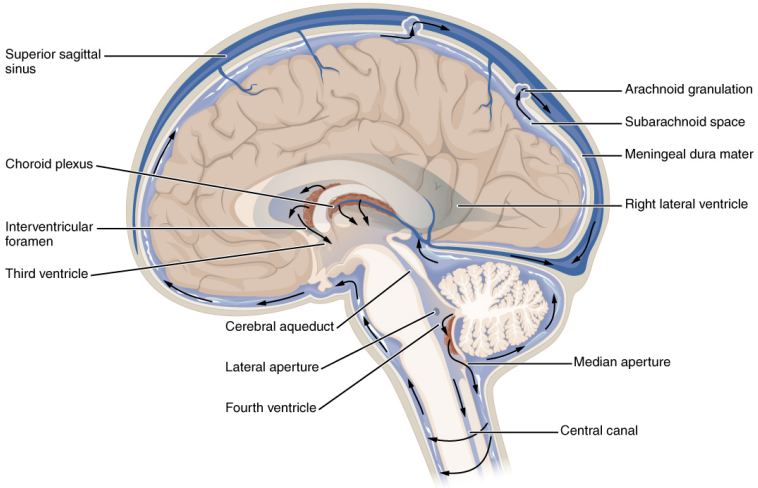

Figure 2.1: The figure shows the CSF circulatory network in the human brain. The cisterna magna is the brain section right above the marking of the median aperture. Image from DeSaix et al. (2020, Chapter 13), and used under a Creative Commons 4.0 license https://creativecommons.org/licenses/by/4.0/.

The role of the CSF and the fluid filling the extracellular space, the interstitial fluid (ISF), became a very popular research field following the article by Iliff, M. Wang, Liao et al. (2012). The authors proposed a network of convective flow in perivascular CSF and extracellular ISF filling the role of the lymphatic system for the brain, and they named it the glymphatic system. The glymphatic hypothesis, as originally proposed, states that waste in the ECS is cleared from the brain by bulk ISF flow transporting the solutes to the cerebrospinal fluid (CSF). The evidence for the proposed system stems mostly from in-vivo experiments in rats. Iliff, M. Wang, Liao et al. (2012) showed rapid entrance of tracer molecules into the brain after injection into the cisterna magna, see Figure 2.1. Furthermore, Xie et al. (2013) demonstrated that tracer clearance rate increased in sleeping or anaesthetised mice compared to awake ones. The authors hypothesised that the increased clearance rate could be attributed to an increase in the extracellular space during sleep, allowing higher ISF flow rates in the ECS.

Yet, the theory is not without controversy. In their review article Abbott et al. (2018) conclude that bulk ISF flow going through aquaporin 4 channels, as suggested by Iliff, M. Wang, Liao et al. (2012), is unlikely. They instead propose a different system for cerebral waste clearance. First, waste products in the ECS is transported diffusively in the ISF. The waste then enters the perivascular spaces (PVS), from which it is transported out of the brain by convective CSF flow. The PVS are small channels of cerebrospinal fluid running alongside cerebral blood vessels. An illustration of a cerebral artery with PVS is illustrated in Figure 2.2. This suggestion is corroborated by the findings of Mestre et al. (2018) and Raghunandan et al. (2021). The article by Mestre et al. (2018) demonstrated convective transport of tracer in the perivascular spaces in mice. Their findings were then supported by Raghunandan et al. (2021) who found that the convective tracer transport in the PVS was not caused by the increased fluid volume from tracer injection. Daversin-Catty et al. (2020) estimate the net flow rate in the cerebral perivascular spaces to be 20 - 30 μm/s. Furthermore, an important biomarker for Alzheimer's disease is the accumulation of certain amyloid-β proteins in the perivascular spaces, see Merlini, Wanner and Nitsch (2016). As a result, the concentration of those proteins is significantly lower in the CSF (Mehta et al. (2000). It seems clear that CSF, and CSF movement in the PVS is an important factor in maintaining the health of the human brain.

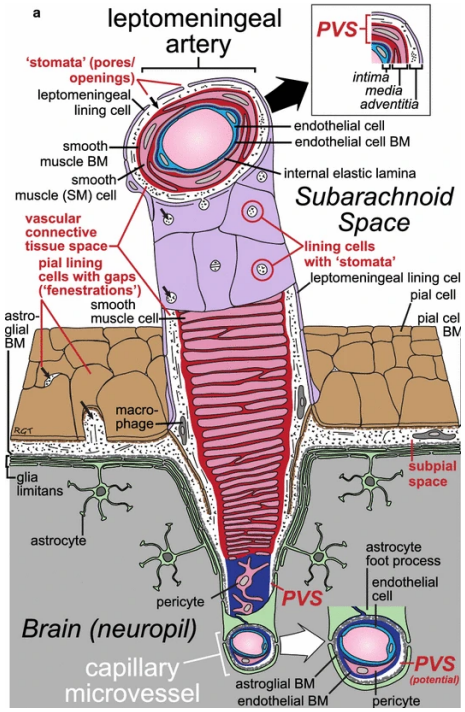

Figure 2.2: The figure illustrates the geometry of a penetrating artery in the human brain. The blue endothelial cells are the cells making up the arterial wall, and the blood brain barrier. The perivascular space is the space in between the endothelium and the grey lining cells. CSF is believed to enter the arterial PVS through small holes, stomata, in these lining cells. We assume the cerebrospinal fluid enters and leaves the brain through the astrocyte end feet in green. The figure is subfigure 1a in Abbott et al. (2018), and used under a Creative Commons 4.0 license https://creativecommons.org/licenses/by/4.0/.

2.2 Normal pressure hydrocephalus

The topic of this thesis is model normal pressure hydrocephalus (NPH), with the specific aim of modelling how healthy and afflicted brains react to an infusion test. The disease of NPH is a neurological disorder characterised by abnormally large ventricles, commonly referred to as ventriculomegaly, but almost normal ICP level (Malm and Eklund (2006)). It is estimated that 22 out of 100 000 people in Norway suffer from the disease (Brean and P. Eide (2008)). The first reported case of the disease was in 1965 by neurologists Salomón Hakim and Raymond D. Adams (Hakim and Adams (1965)). The illness itself is often characterised into two distinct subcategories, namely *idiopathic* NPH (iNPH) and *secondary* NPH. (sNPH). The latter of the two is a complication of illnesses such as stroke, brain tumor or head trauma (Daou et al. (2016)), while iNPH is a chronic illness of unknown origin which develops over a longer period of time. All three cases in Hakim and Adams (1965) responded well to a ventricular shunt and drainage of CSF. Not all patients with NPH, however, benefit from shunt-surgery (Esmonde and Cooke (2002)), and the task of deciding which

patients to operate is a difficult one.

The disease of NPH is one of the few known forms of reversible dementia. (Tripathi and Vibha (2009)). While many studies found the efficacy of surgery to be unlikely (Vanneste et al. (1992), Esmonde and Cooke (2002)), the evidence seem to suggest that with proper preoperative screening (Ryding, Kahlon and Reinstrup (2018), Toma et al. (2013)) the success rate is clear. Significant advancement in diagnostic criteria was made when Relkin et al. (2005) published the first set of systematic diagnostic criteria. The diagnostic criteria classify patients into three groups, namely probable, possible and unlikely iNPH. To receive a rating of probable, a patient need to satisfy a multitude of criteria relating to disease history, symptoms and MRI findings. A patient classified as possible still need to show clear signs of hydrocephalus, but might not exhibit all the common symptoms associated with iNPH.

The diagnostic criteria gives a good overview over how the brain is changed in iNPH-patients. They do, however, not explain how these changes happen. An early attempt at explaining the disease was that of Hakim, Venegas and Burton (1976). They propose that the cognitive decline and loss of motor functions seen in NPH patients is due to the increased surface area of the ventricles. For while the ICP remain at almost the same level as that of healthy adults, the increase in surface area results in a greater force $\mathbf{F}_p$ being exerted on the brain. The total force exerted from ventricular CSF pressure, p_{vent}, is:

$$\mathbf{F}_p = -\oint_{S_{vent}} p_{vent}\hat{\mathbf{n}}dS, \tag{2.1}$$

where S_{vent} is the ventricular surface. This force is proposed to result in a compression of the white matter in the cerebrum, which might be the cause of the loss of cognitive ability. As for the formation of ventriculomegaly, the authors propose that it is caused by either a reduced CSF drainage from, or an increased CSF pressure in the lateral ventricles. The total CSF volume is increased in iNPH patients, Malm and Eklund (2006) states the average iNPH patient has a intracranial CSF volume of 280 ml, while healthy individuals have 195 ml on average. However, the explanation of Hakim, Venegas and Burton (1976) suffers from the fact that Gideon et al. (1994) found that CSF was produced at a similar rate in iNPH patients as in healthy individuals. Furthermore, Lindstrøm et al. (2018), P. K. Eide, L. M. Valnes et al. (2021) and Gideon et al. (1994) found that aqueductal CSF flow was higher in iNPH patients than in healthy individuals. This suggests that a blocked CSF clearance from the ventricles is not a necessary component in developing the disease.

A more recent contribution to understanding the pathogenesis of the disease is the review by Z. Wang et al. (2020). Their review did not find a single underlying cause, but instead proposed that iNPH is the end result of several interacting processes. A multitude of factors, like CSF disturbance, glymphatic dysfunction and the disruption of the BBB are all found to play an important role in the formation of the disease. Scollato et al. (2008) found that iNPH patients with high net CSF flow in the sylvan aqueduct are in general more responsive to shunt surgery. Furthermore, they also found a falling CSF flow rate in the aqueduct over time, and that this might be a sign of irreversible ischemic injury to brain tissue. This could help explain why some patients does not benefit from shunt surgery. In addition to increased aqueductal flow, Z. Wang et al. (2020) believes the CSF clearance obstruction to play a major

role in the pathophysiology and pathogenesis of the disease. They highlight that Kim et al. (2015) found an R_{out} of twelve or more to be a good indicator of shun surgery success. Furthermore, Bateman and Siddique (2014) found that an increase in venous pressure led to a severe reduction in CSF clearance through the dural sinus. While these changes give a good overview over what effects might lead to the formation of hydrocephalus, the exact causes for these changes are not known.

So far, the only widespread treatment of iNPH is to install a shunt from either the ventricles or the spine and into the stomach. (Z. Wang et al. (2020)). The aim of the surgery is to construct an alternate pathway for CSF clearance from the CNS. However, not all patients benefit from shunt surgery, and early detection is often critical to ensure a favourable outcome. (Scollato et al. (2008), Andrén et al. (2021)). The most common way to determine if a patient would benefit from a shunt surgery is infusion testing, as described in Ryding, Kahlon and Reinstrup (2018) and Malm and Eklund (2006). An infusion test is a diagnostic procedure where artificial CSF is injected into the CSF network, most commonly by lumbar puncture. The added liquid will increase the intercranial CSF pressure, until a new equilibrium is reached. There are two different procedures, namely one where CSF is injected continuously and until the pressure has stabilised at the new equilibrium, or one in which the CSF is injected continuously but at an increasing rate. In the latter procedure, the aim is to reach several equilibria, one for each infusion rate. We will in our model focus on the former of the two procedures. Using the stabilised pressures, it is possible to compute the outflow resistance R_{out}. Analysis of this resistance in conjunction with plateau pressure is the common parameters considered when deciding if the patient would benefit from the shunt surgery (see Ryding, Kahlon and Reinstrup (2018) and Kim et al. (2015)). Hence, the infusion test is a crucial tool in ensuring proper treatment of patients with iNPH. Modelling how an infusion test changes the fluid flows of the brain might shed light on the mechanisms of the disease, and we will do so using fluid mechanics and the finite element method (FEM).

CHAPTER 3

Notation and Mathematical Foundations

Many problems in fluid mechanics are expressed through partial differential equations (PDEs), such as the Navier-Stokes equations, the heat equation, Biot's equation or the Stokes equations. As a result, solving such equations is important when working with fluid mechanics. In simple situations this can be done analytically or with classical numerical methods like finite differencing. In many practical problems, however, the geometry or equations involved are too complicated for these methods to suffice. Because of this, more sophisticated ways of solving PDEs are often required.

The finite element method is one popular way for solving PDEs numerically on complicated geometries, and the one we will use in this thesis. The method does, in general, retain good convergence rates and implementational simplicity even as the domains become more irregular. This section will be a short summary of the finite element method, where we also introduce relevant notation and terminology. For finite element theory we will use Langtangen and Mardal 2019 and Mardal and Logg 2021, while for the mathematical theory we will be relying on Evans 2010.

A partial differential equation is an equation expressing a relation between an unknown function $\mathbf{u}\colon \Omega \to \mathbb{R}^n$, its derivatives and a known function $\mathbf{f}\colon \Omega \to \mathbb{R}^n$. The domain, Ω, is some subset of $\mathbb{R}^m$ which is usually bounded. In addition to the equation itself, knowledge about the initial state of the system and how the unknown function $\mathbf{u}$ behaves on the boundary is often necessary. Letting $\mathcal{L}$ denote a differential operator, we can define a partial differential equation to be a set of equations on the following form.

$$\begin{cases} \mathcal{L}[\mathbf{u}](\mathbf{x},t) = \mathbf{f}(\mathbf{x},t), & \mathbf{x} \in \Omega, t > 0, \\ \mathbf{u}(\mathbf{x},t) \ = \mathbf{g}_d(\mathbf{x},t), & \mathbf{x} \in \partial\Omega_D, t > 0, \\ -\nabla\mathbf{u}\cdot\hat{\mathbf{n}} = \mathbf{g}_n(\mathbf{x},t), & \mathbf{x} \in \partial\Omega_N, t > 0, \\ -\nabla\mathbf{u}\cdot\hat{\mathbf{n}} = \mathbf{g}_r(\mathbf{x},t,\mathbf{u}), & \mathbf{x} \in \partial\Omega_R, t > 0, \\ \mathbf{u}(\mathbf{x},0) = \mathbf{h}(\mathbf{x}), & \mathbf{x} \in \Omega, t = 0. \end{cases} \tag{3.1}$$

Here $\partial\Omega$ is the domain boundary and t denotes time. The sets $\partial\Omega_N$, $\partial\Omega_R$ and $\partial\Omega_D$ are three subsets of the boundary with $\partial\Omega = \partial\Omega_N \cup \partial\Omega_R \cup \partial\Omega_D$. The second, third and fourth equations in (3.1).

We will initially address the finite element method for stationary problems.Restricting our attention to some vector space, V, the solution to the

PDE would be the function $\mathbf{u} \in V$ which, when we apply $\mathcal{L}$ on $\mathbf{u}$, returns the function $\mathbf{f}$. While many of the important results in modern PDE theory, such as the Lax-Milgram theorem, holds as long as V is a Banach-space, we will move forward assuming V is a separable Hilbert space. More specifically, we will assume V to be the Sobolev space, $H^k(\Omega)$, for a sufficiently high k. This space is defined as the set of all functions $\mathbf{u}$ satisfying:

$$\|\mathbf{u}\|^2_{H^k(\Omega)} = \sum_{|\alpha|=0}^{k} \int_\Omega \left| \frac{\partial^\alpha}{\partial \mathbf{x}^\alpha} \mathbf{u} \right|^2 d\mathbf{x} < \infty. \tag{3.2}$$

Here $\alpha \in \mathbb{N}^m$ is a multi-index and $|\alpha|$ is the sum of its components. This restriction to $H^k(\Omega)$ is necessary for the finite element method to be applicable.

Rather than looking directly for solutions to PDEs, the finite element method seeks to solve such equations almost everywhere, i.e. to find a solution, satisfying the PDE on all of the domain except for a set of measure zero. Such solutions are called weak solutions, and we will now explain how the finite element method can be used to find them.

The process starts by constructing a bilinear map, $B\colon H^k \times H^k \to \mathbb{R}$, defined as

$$B(\mathbf{u}, \mathbf{v}) = \int_\Omega \mathcal{L}(\mathbf{u}) \cdot \mathbf{v} \, d\mathbf{x}. \tag{3.3}$$

The function $\mathbf{v}$ is commonly called a test function, and $\mathcal{L}$ is the differential operator defining the PDE. The variational form of the partial differential equation is now given by

$$\text{Find } \mathbf{u} \in H^k(\Omega) \text{ such that } B(\mathbf{u}, \mathbf{v}) = \langle \mathbf{f}, \mathbf{v} \rangle_{L^2(\Omega)}, \quad \text{for all } \mathbf{v} \in H^k(\Omega). \tag{3.4}$$

Here, $\langle \mathbf{f}, \mathbf{v} \rangle_{L^2(\Omega)}$ is the L^2 inner product between $\mathbf{f}$ and $\mathbf{v}$ over Ω, and is defined by

$$\langle \mathbf{f}, \mathbf{v} \rangle_{L^2(\Omega)} = \int_\Omega \mathbf{f} \cdot \mathbf{v} \, d\mathbf{x}, \tag{3.5}$$

where L^2 is the set of square-integrable functions.

An observant reader might notice that the boundary and initial conditions are absent from our variational formulation and would need to be incorporated into the variational form for the problem to be well posed. Dirichlet boundary conditions are typically enforced directly by numerical solvers, and it is common to require the test functions $\mathbf{v}$ to be zero on the Dirichlet boundary. The Neumann and Robin conditions on the other hand can not be enforced this way. For second order PDEs, a common way to implement these types of boundary conditions is by applying integration by parts on the second order terms in Equation (3.3), reformulating the variational form to the following. Find $\mathbf{u} \in H^k(\Omega)$ such that:

$$B(\mathbf{u}, \mathbf{v}) = \langle \mathbf{f}, \mathbf{v} \rangle_{L^2(\Omega)} + \langle \mathbf{g}_n, \mathbf{v} \rangle_{L^2(\partial\Omega_N)} + \langle \mathbf{g}_r, \mathbf{v} \rangle_{L^2(\partial\Omega_R)}, \tag{3.6}$$

for all $\mathbf{v} \in H^k(\Omega)$. In this thesis, we will assume the Robin function $\mathbf{g}_r$ to be linear with $\mathbf{u}$. This allows us to include the parts of $\mathbf{g}_r$ varying with $\mathbf{u}$ in

the bilinear form. The remaining terms can be combined with the Neumann boundary condition. Hence, we let denote the combined Robin- and Neumann boundary function and $\partial\Omega_{NR} = \partial\Omega_N \cup \Omega_R$ the combined Neumann and Robin boundary.

In this thesis, we will solve PDEs numerically using the Galerkin method. This approach is based on projecting the exact solution, u, onto a finite-dimensional subspace $H_h^k(\Omega) \subset H^k(\Omega)$, as explained in Langtangen and Mardal 2019, chapters 3-6. Letting $\mathbf{u}_h$ denote the numerical solution, the discrete variational problem becomes

$$\text{Find } \mathbf{u}_h \in H_h^k(\Omega) \text{ such that } B(\mathbf{u}_h, \mathbf{v}) = \langle \mathbf{f}, \mathbf{v} \rangle_{L^2(\Omega)} + \langle \mathbf{g}, \mathbf{v} \rangle_{L^2(\partial\Omega_{NR})}, \quad (3.7)$$

for all $\mathbf{v} \in H_h^k(\Omega)$. The discrete solution $\mathbf{u}_h$ is the best possible approximation of $\mathbf{u}$ in $H_h^k(\Omega)$. This follows from the projection theorem, and since $H^k(\Omega)$ is a separable Hilbert space, there exists a countable subset $\{\psi_i(\mathbf{x})\}_{i\in\mathbb{N}} \subset H^k(\Omega)$ which form a basis for $H^k(\Omega)$. As $H_h^k(\Omega)$ is a finite-dimensional subspace of $H^k(\Omega)$, we know our projected solution $\mathbf{u}_h$ can be written as a finite linear combination of basis functions from $\{\psi_i(\mathbf{x})\}_{i\in\mathbb{N}}$. This allows us, by the linearity of $B(\mathbf{u}, \mathbf{v})$, to write Equation (3.7) as

$$\sum_{i=1}^{N} c_i B(\psi_i, \mathbf{v}) = \langle \mathbf{f}, \mathbf{v} \rangle_{L^2(\Omega)} + \langle \mathbf{g}, \mathbf{v} \rangle_{L^2(\partial\Omega_{NR})}, \quad \text{for all } \mathbf{v} \in H_h^k(\Omega). \quad (3.8)$$

Here $N = \dim(H_h^k(\Omega))$ and c_i are the unknown coefficients of the linear combination of basis vectors constituting our approximate solution $\mathbf{u}_h$.

After this reformulation, the numerical problem is reduced to finding a good way of determining the coefficients c_i. To do this, we need to ensure that Equation (3.9) holds for all $\mathbf{v} \in H_h^k(\Omega)$. This can be guarantee by making sure the equation holds for each basis function ψ_j in the basis of the finite dimensional subspace, $H_h^k(\Omega)$. Hence, the final set of equations are

$$\sum_{i=1}^{N} c_i B(\psi_i, \psi_j) = \langle \mathbf{f}, \psi_j \rangle_{L^2(\Omega)} + \langle \mathbf{g}, \psi_j \rangle_{L^2(\partial\Omega_{NR})}, \quad \text{for } j = 1, 2, 3, \ldots, N. \quad (3.9)$$

The above N equations can be solved to uniquely compute the c_is, and can be reformulated as a linear system $A\mathbf{c} = \mathbf{b}$. Here $\mathbf{c}$ is the vector of coefficients in the linear combination $\mathbf{u}_h = \sum_i c_i \psi_i(\mathbf{x})$. Linear systems can be solved using standard linear algebra methods.

So far, we have only discussed stationary problems. The extensions to time dependent problems is however straightforward. The aim is to transform the time-dependent problem into a stationary problem. Afterwards, the theory above can be used to solve the resulting equation for each time step. In Equation (3.1), we have expressed the PDE through one unified operator $\mathcal{L}[\mathbf{u}]$, containing both spatial and temporal derivatives. If we assume, for the sake of simplicity, that the time derivatives are all of first order, we could rewrite the equation to be

$$\frac{\partial \mathbf{u}}{\partial t} = \mathcal{L}_s[u], \quad (3.10)$$

where $\mathcal{L}_s[\mathbf{u}]$ is a differential operator containing only spatial derivatives. In this thesis, we will only solve PDEs with first order time derivatives, and hence

Equation (3.10) can be used. The domain, boundary conditions and initial conditions remain unchanged from Equation (3.1).

We will solve equations on the time domain $(0, T]$. To do so numerically we first introduce a partition of this time interval. While any finite collection of points $\{t^i\}_{i=1}^{N_t} \subset (0, T]$ can be used, we will assume a uniform discretisation with step size Δt. An implicit first order discretisation gives us an equation on the following form

$$\mathbf{u}^n = \mathbf{u}^{n-1} + \Delta t \mathcal{L}_s[\mathbf{u}^n], \tag{3.11}$$

where $\mathbf{u}^n = \mathbf{u}(\mathbf{x}, t^n)$ and $t^n = n\Delta t$. It is important to note that any convergent time discretisation work, but we use a first order implicit discretisation due to its stability and simplicity.

CHAPTER 4

Mathematical Model of the Brain

Now that the mathematical foundation is in place, we will establish the mechanis and physics forming the foundation for our model. First, the governing equations are presented and derived. We then formulate the weak form of these. Afterwards, we will present and explain which values we used for each parameter and give a justification for these choices. Thereafter, we discuss how we can use patient specific data to tune our model, before we, at the end, present how our quantities of interests are computed from the model output.

4.1 Governing equations

In Tully and Ventikos 2011, the authors proposed that the brain can be modelled as a porous and elastic medium containing several communicating fluid filled networks. They suggested using a set of equations first derived for geomechanical applications called the Multiple Poroelastic Network Theory equations, or the MPET-equations for short. The model was developed by Aifantis (1979) and Aifantis and Hill (1980) who established the equations to model diffusive transport of solutes in porous media containing two communicating fluid networks. The communicating fluid networks are often referred to as compartments in the literature, and we will refer to them as such from now on. The framework of Aifantis and Hill (1980) was extended to account for any number of communicating networks by Bai, Elsworth and Roegiers (1993). We will, in this thesis use these ideas as a foundation for our model.

The MPET model, as stated by Tully and Ventikos (2011), consists of one equation for the deformation of the brain parenchyma, and one additional equation for the pressure in each compartment of the model. Assume the brain is permeated by a collection of fluid filled compartments indexed by a set, $\mathcal{I}$. Furthermore, let $\mathbf{u}$ denote the deformation of the brain parenchyma, G the shear modulus, and p_i the pressure field in compartment $i \in \mathcal{I}$. Lastly, we refer to the domain and time as $\Omega \subset \mathbb{R}^3$ and t respectively. Then the equation governing the brain deformations is given by:

$$-G\frac{\partial^2 \mathbf{u}}{\partial t^2} + \nabla \cdot \sigma - \sum_{i \in \mathcal{I}} \alpha_i \nabla p_i = 0, \quad \mathbf{x} \in \Omega, t > 0. \tag{4.1}$$

Here, no body forces is assumed, and $\sigma = \left(\nabla \mathbf{u} + \nabla \mathbf{u}^T\right) + \frac{1}{2}\lambda \nabla \cdot \mathbf{u}\mathbf{I}$ is the linear stress tensor. Similarly, the equation modelling the pressure interactions

between the pressure in compartment $i \in \mathcal{I}$ and the other compartments is given by the following expression:

$$C_i \frac{\partial p_i}{\partial t} + \alpha_i \frac{\partial}{\partial t}(\nabla \cdot \mathbf{u}) - k_i \nabla^2 p_i - k_i \nabla \cdot \left(\rho_i \frac{\partial^2 \mathbf{u}}{\partial t^2} \right) + \sum_{\substack{j \neq i \\ j \in \mathcal{I}}} \omega_{ij}(p_i - p_j) = 0. \tag{4.2}$$

Here α_i is the compartment Biot-parameter, ρ_i the mass density of the fluid in compartment i, and C_i is the compartmental compliance parameter. Furthermore, ω_{ij} denotes the transfer coefficient between compartments and the parameter k_i is the hydraulic conductivity of the compartment. Do note that hydraulic conductivity is related to permeability, denoted by κ_i, by the following equation:

$$k_i = \frac{\kappa_i}{\mu_i}, \tag{4.3}$$

where μ_i is the dynamic viscosity of the fluid in the compartment. Tully and Ventikos (2011) used four compartments, one for cerebral arteries, one for cerebral capillaries, one for cerebral veins and one compartment combining the ECS and cerebral PVS. We, on the other hand will be using seven compartments. These are arteries, capillaries, veins, arterial PVS, capillary PVS, venous PVS and the ECS. How we assume these compartments to be connected can be seen in Figure 4.1 A central assumption in the MPET framework is that compartments are homogenised. Mathematically, this means that each compartmental pressure p_i is a function on the entirety of the domain Ω.

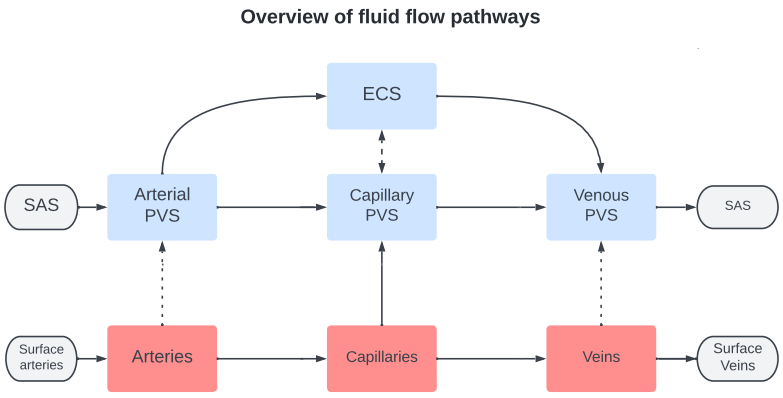

Figure 4.1: Connection overview for the seven compartment MPET model. Whole arrows indicate connections we are sure exist, and know the direction of. Dashed arrows are geometrically possible, but whether they are connected and to what extent is unknown. Red compartments are filled with blood, blue with cerebrospinal or interstitial fluid. PVS is short for perivascular space, ECS is short for extracellular space and SAS is short for subarachnoid space.

We will in our thesis assume that the deformation of the brain tissue remains small, meaning $\|\mathbf{u}\| = \sqrt{\mathbf{u} \cdot \mathbf{u}} \leq \epsilon$ for a suitably small epsilon almost everywhere in Ω. Under this assumption, we can safely neglect several terms

in Equation (4.2), and ignore Equation (4.1) all together. Evidence exists of deformations of the brain parenchyma both under short term processes such as the cardiac cycle (E. Lee, J. Wang and Mezrich (1989), A. A. Linninger et al. (2009)) and long time processes as the sleep/wake cycle (Xie et al. (2013)). We will, however, model an infusion test, a process which typically lasts on a time scale of thirty to sixty minutes (Kahlon, Sundbärg and Rehncrona (2005)). Hence, the time scale is too long for it to be computationally feasible to model vascular pulsation, and too short for any circadian effects to present realistically itself. With the assumption of negligible deformation, Equation (4.2) reduces to:

$$C_{p_i}\frac{\partial p_i}{\partial t} - k_i\nabla^2 p_i + \sum_{\substack{j\neq i \\ j\in\mathcal{I}}}\omega_{ij}(p_i - p_j) = 0, \qquad \mathbf{x}\in\Omega, t>0. \tag{4.4}$$

Boundary conditions

Now that we have established our governing equations, we will turn our attention to the boundary conditions. While we will discuss our meshing procedure later, we do note that our mesh has three surface markings. These are the pial surface Γ_{pial}, the ventricular surface Γ_{vent}, and the surface of the brain stem Γ_{stem}. The surface of the brain stem has been modelled as a solid boundary in all compartments. While CSF bulk flow happens in the sylvan aqueduct, see for instance P. K. Eide, L. M. Valnes et al. (2021), Lindstrøm et al. (2018), this aqueduct is not a part of our mesh and hence can not be modelled. We will also here introduce the Darcy velocity $\mathbf{q}$, which is commonly defined (see for instance Vinje et al. (2020)) by:

$$\mathbf{q}_i = -k_i\nabla p_i. \tag{4.5}$$

Darcy's law reveals that the fluid flow in a compartment is proportional to the pressure gradient in the compartment. Hence, a Neumann boundary condition on the form $k_i\nabla p_i = g$ is a way to enforce the inflow into a compartment. We begin by discussing the arterial compartment and its boundary conditions, and this relation between inflow and Neumann conditions allows us to specify the rate of arterial blood flow with a high degree of accuracy. The ventricles are assumed to not exchange fluid with the arterial compartment. Letting B_{in} denote the average arterial inflow rate per square meter nets us the following boundary conditions for the arterial compartment.

$$k_a\nabla p_a\cdot\hat{\mathbf{n}} = B_{in}, \qquad \mathbf{x}\in\Gamma_{pial},\ t\geq 0, \tag{4.6}$$

$$k_a\nabla p_a\cdot\hat{\mathbf{n}} = 0, \qquad \mathbf{x}\in\Gamma_{vent},\ t\geq 0. \tag{4.7}$$

How and where the CSF is produced is a divisive topic in the academic community. Some, like Abbott et al. (2018) believe the choroid plexuses to be the source of CSF production. Others, such as Brinker et al. (2014) think the CSF is formed by filtration in the cerebral capillaries. We will follow the example of Tully and Ventikos (2011) and assume CSF is produced by the choroid plexus at a rate of $Q_{prod} = 0.33$ ml/min. This CSF is produced by draining fluid from the capillaries, and then deposit the CSF in the lateral ventricles. We will also assume that no cerebral blood leaves the brain through

the capillaries, and we will as such set a homogeneous Neumann condition on the pial surface. The boundary conditions for the capillary compartments are:

$$k_c \nabla p_c \cdot \hat{\mathbf{n}} = 0, \qquad \mathbf{x} \in \Gamma_{pial},\ t \geq 0, \tag{4.8}$$

$$k_c \nabla p_c \cdot \hat{\mathbf{n}} = -Q_{prod}, \qquad \mathbf{x} \in \Gamma_{vent},\ t \geq 0. \tag{4.9}$$

As with the arterial compartment, we assume that all venous blood leaves the parenchyma through the pial surface. As to not enforce how the fluid flows through the compartments, we will not hard code the venous outflow. Instead, we will model it by a Robin type boundary condition relating outflow to the difference between vascular pressure and the pressure in subarachnoid CSF, p_{CSF}, and the dural sinus pressure, p_{DS}. This outflow is based on the proposed exit ways of CSF by Iliff, M. Wang, Liao et al. (2012), who suggested that perivascular CSF leaves the brain and either reenters the subarachnoid CSF or leaves the cranium. Assuming the cerebral veins and venous perivascular space follow the same path leads us to apply the same boundary conditions on the venous compartment as the perivenous. Hence, venous blood either leaves the brain through the dural sinus (DS) or into veins on the pial surface. The dural sinus pressure, p_{DS}, was estimated by Vinje et al. (2020) to be 8.4 mmHg. The CSF pressure, p_{CSF}, is discussed later in this section. The boundary conditions for the venous compartment are:

$$k_v \nabla p_v \cdot \hat{\mathbf{n}} = \beta_1 \left(\frac{p_{DS} + p_{CSF}}{2} - p_v \right), \qquad \mathbf{x} \in \Gamma_{pial},\ t \geq 0, \tag{4.10}$$

$$k_v \nabla p_v \cdot \hat{\mathbf{n}} = 0, \qquad \mathbf{x} \in \Gamma_{vent},\ t \geq 0. \tag{4.11}$$

Here $\beta_1 = 10^{-3}$ is a numerical parameter which captures how easy or hard it is for fluid to exit through the pathway. Parameters like β_1 will be used in three boundary conditions. These parameters were set after testing with different values.

The periarterial compartment will, like the arterial compartment, regard the ventricular wall as an impermeable membrane. Hence, a homogenous Neumann condition will be applied on the ventricles. We will assume CSF enters the arterial PVS from the SAS, and that this flow rate proportional to the pressure difference between the CSF pressures in the SAS and arterial PVS. Letting $\beta_2 = 10^{-3}$ be a flow resistance coefficient, the periarterial boundary conditions are:

$$k_{pa} \nabla p_{pa} \cdot \hat{\mathbf{n}} = \beta_2 \left(p_{CSF} - p_{pa} \right), \qquad \mathbf{x} \in \Gamma_{pial},\ t \geq 0, \tag{4.12}$$

$$k_{pa} \nabla p_{pa} \cdot \hat{\mathbf{n}} = 0, \qquad \mathbf{x} \in \Gamma_{vent},\ t \geq 0. \tag{4.13}$$

We will assume that there is no fluid entering or leaving the pericapillary compartment through either pia or the ventricles. Homogenous Neumann conditions therefore apply on both boundaries, and our conditions are:

$$k_{pc} \nabla p_{pc} \cdot \hat{\mathbf{n}} = 0, \qquad \mathbf{x} \in \Gamma_{pial},\ t \geq 0, \tag{4.14}$$

$$k_{pc} \nabla p_{pc} \cdot \hat{\mathbf{n}} = 0, \qquad \mathbf{x} \in \Gamma_{vent},\ t \geq 0. \tag{4.15}$$

We enfore the same type of boundary conditions on perivenous compartment will as we do on the venous compartment. These conditions are homogenous Neumann on the ventricles and a Robin-boundary condition on the pial boundary.

With $\beta_3 = 10^{-7}$, we have the following boundary conditions for the venous PVS:

$$k_{pv}\nabla p_{pv} \cdot \hat{\mathbf{n}} = \beta_3 \left(\frac{p_{DS} + p_{CSF}}{2} - p_{pv} \right), \qquad \mathbf{x} \in \Gamma_{pial},\ t \geq 0, \tag{4.16}$$

$$k_{pv}\nabla p_{pv} \cdot \hat{\mathbf{n}} = 0, \qquad \mathbf{x} \in \Gamma_{vent},\ t \geq 0. \tag{4.17}$$

Finally, for the extracellular compartment, we assume that no ISF leaves the brain directly from the compartment. Hence, we enforce homogeneous Neumann conditions on the entire boundary, giving us the following equations:

$$k_e\nabla p_e \cdot \hat{\mathbf{n}} = 0, \qquad \mathbf{x} \in \Gamma_{pial},\ t \geq 0, \tag{4.18}$$

$$k_e\nabla p_e \cdot \hat{\mathbf{n}} = 0, \qquad \mathbf{x} \in \Gamma_{vent},\ t \geq 0. \tag{4.19}$$

The cerebrospinal fluid pressure

In our boundary conditions for the perivenous, periarterial and venous pressure, we relied on the quantity of subarachnoid cerebrospinal fluid pressure. The pressure in the subarachnoid CSF, which we will often refer to as intracranial pressure (ICP), is the pressure that is measured during an infusion test. We will model this using the equation derived by Vinje et al. (2020). Assuming CSF is produced at a rate of Q_{prod} and infused at a rate of Q_{inf}, Vinje et al. (2020) models the ICP by the following equation:

$$C_{CSF}\frac{\partial p_{CSF}}{\partial t} = Q_{prod} + Q_{inf} + \frac{p_{DS} - p_{CSF}}{R_{DS}} + \frac{p_{crib} - p_{CSF}}{R_{crib}}. \tag{4.20}$$

Here, R_{DS} and R_{crib} are the outflow resistance parameters of the dural sinus and cribiform plate respectively, and $p_{DS} = 8.4$ mmHg and $p_{crib} = 0$ mmHg are the pressures at these points. Finally, we have assumed an infusion rate $Q_{inf} = 1.5$ ml/min, and that CSF is produced at a rate $Q_{prod} = 0.33$ ml/min (Deisenhammer et al. (2015)). A pressure of 0 mmHg corresponds to atmospheric pressure. Do note that Vinje et al. (2020) had an additional term in Equation (4.20) modelling the pressure interaction between PVS and SAS. One of their main results was that the fluid clearance through the PVS was significantly lower than through the dural sinus or cribiform plate. Hence, we decided to ignore this interaction to reduce the computational complexity. The parameter C_{CSF} is the compliance for the SAS, and is given by Vinje et al. (2020) to be:

$$C_{CSF}(p_{CSF}) = \begin{cases} (E[p_{CSF} - p_r])^{-1} & p, \geq p_{tres}, \\ (E[p_{tres} - p_r])^{-1}, & p_{CSF} < p_{tres}. \end{cases} \tag{4.21}$$

The new parameters in this equations are the elastance E, the treshold pressure p_{tres} and the reference pressure p_r. Vinje et al. (2020) estimates the elastance to be 0.2 ml^{-1}, the treshold pressure to be about 11 mmHg and the reference pressure to be 9 mmHg. We will use these values when testing the importance of geometry on our model, but we will adjust them in Section 4.4 to capture the patient specific responses to an infusion test.

4.2 The weak formulation

We wish to employ the finite element method to solve the set of equations highlighted in the previous section. Doing so requires the derivation of the variational formulation of the equations. Let $\{q_i\}_{i=1}^{7}$ be a collection of test functions belonging to the Sobolev space $H^1(\Omega \times [0,T))$. For each compartmental pressure p_i and index $i \in \mathcal{I}$, we can multiply Equation (4.4) with the corresponding test function q_i. Integrating each equation over the domain Ω and summing all the equations together yields:

$$\sum_{i\in\mathcal{I}} \int_\Omega C_{p_i} \frac{\partial p_i}{\partial t} q_i - k_i \nabla^2 p_i q_i + \sum_{\substack{j\neq i \\ j\in\mathcal{I}}} \omega_{ij}(p_i - p_j) q_i \; d\mathbf{x} = 0. \tag{4.22}$$

Using integration by parts, this equation can be rewritten to:

$$\sum_{i\in\mathcal{I}} \int_\Omega C_{p_i} \frac{\partial p_i}{\partial t} q_i + k_i \nabla p_i \cdot \nabla q_i + \sum_{\substack{j\neq i \\ j\in\mathcal{I}}} \omega_{ij}(p_i - p_j) q_i \; d\mathbf{x} = \sum_{i\in\mathcal{I}} \int_{\partial\Omega} k_i \nabla p_i q_i \cdot \hat{\mathbf{n}} dS.$$

The right hand side of the above equation can be used to enforce our boundary conditions. By inserting our chosen boundary conditions, we get that the following expression has to equal zero:

$$\begin{aligned}
&\textstyle\sum_{i\in\mathcal{I}} \int_\Omega \quad C_{p_i} \dfrac{\partial p_i}{\partial t} q_i + k_i \nabla p_i \cdot \nabla q_i + \sum_{\substack{j\neq i \\ j\in\mathcal{I}}} \omega_{ij}(p_i - p_j) q_i \; d\mathbf{x}, \\
&- \textstyle\int_{\Gamma_{pial}} \qquad Q_{in} q_a + \beta_1 \left(\dfrac{p_{DS} + p_{CSF}}{2} - p_v \right) q_v dS, \\
&- \textstyle\int_{\Gamma_{pial}} \qquad \beta_2 (p_{CSF} - p_{pa}) + \beta_3 \left(\dfrac{p_{DS} + p_{CSF}}{2} - p_{pv} \right) dS, \\
&+ \textstyle\int_{\Gamma_{vent}} \qquad Q_{prod} q_c dS.
\end{aligned} \tag{4.23}$$

In Equation (4.23), we have derived a full spatial discretisation of our governing equations. The final step is to discretise the equation in time. We chose a fully implicit first order scheme. Letting p_i^n denote the pressure in compartment i at time $t = t_n$, we get left hand side of:

$$\begin{aligned}
&\textstyle\sum_{i\in\mathcal{I}} \int_\Omega \quad C_{p_i} \dfrac{p_i^n - p_i^{n-1}}{\Delta t} q_i + k_i \nabla p_i^n \cdot \nabla q_i + \sum_{\substack{j\neq i \\ j\in\mathcal{I}}} \omega_{ij}(p_i^n - p_j^n) q_i \; d\mathbf{x}, \\
&- \textstyle\int_{\Gamma_{pial}} \qquad Q_{in} q_a + \beta_1 \left(\dfrac{p_{DS}^n + p_{CSF}^n}{2} - p_v^n \right) q_v dS, \\
&- \textstyle\int_{\Gamma_{pial}} \qquad \beta_2 (p_{CSF}^n - p_{pa}^n) + \beta_4 \left(\dfrac{p_{DS}^n + p_{CSF}^n}{2} - p_{pv}^n \right) dS, \\
&- \textstyle\int_{\Gamma_{vent}} \qquad \beta_3 (p_{CSF}^n - p_{pa}^n) - Q_{prod} q_c dS.
\end{aligned} \tag{4.24}$$

The right hand side of the equation is zero. with the equation fully discretised, we will dedicate the next sections to explain how we determined the values of each parameter we used in our model.

4.3 Input data and uncertainties

In Equation (4.24) we solve for seven unknown pressure fields. In addition to these there are a total of 52 parameters we need to specify for our problem to be well defined. While some of the parameters are well documented in the literature, others are more speculative. We have listed every parameter which needs to be specified for an implementation of our model in Table 4.1. This section will be dedicated to present the values of each parameter and provide a justification for why that value was chosen.

Parameter type	**Symbol**	**Number of parameters**
Hydraulic conductivity	k_i	7
Compliance	C_{p_i}	7
Transfer coefficient	ω_{ij}	21
CSF inflow	Q	2
Arterial inflow	B	1
Boundary permeability	β_i	3
Outflow resistance	R	2
External pressures	p	2
Porosity	ϕ	7

Table 4.1: The table gives an overview over the different kinds of parameters used directly in our model. In addition, the amount of different parameters in each parameter class is shown. The total amount of parameters is 52.

Determining the hydraulic conductivities

We will start by discussing our values for the compartmental hydraulic conductivity. Assuming the pressure gradient to be constant, i.e. $\nabla p = \Delta p/L$ for a characteristic length scale L, we can find the volume flux Q through a cross section A of a pore to be:

$$Q = \int_A \mathbf{q} \cdot \hat{\mathbf{n}} dS = \frac{k \Delta p A}{L}. \tag{4.25}$$

Here, $\mathbf{q}$ is the Darcy velocity as defined in Equation (4.5). We define the outflow resistance R in the same manner as Vinje et al. (2020), namely by:

$$R = \frac{\Delta p}{Q}. \tag{4.26}$$

By some rearrangement of Equation (4.25), we find a relation between hydraulic conductivity and resistivity, namely:

$$R_i = \frac{L}{k_i A}, \tag{4.27}$$

We have here added subscripts to the conductivity and resistivity to denote that the different compartments might have different resistances and conductivities. As we have homogenised our domain the characteristic length scale and cross

sectional area are the same for all compartments. Rearranging Equation (4.27), we get

$$R_i k_i = \frac{L}{A} = C. \tag{4.28}$$

Equation (4.28) allow us to find a common constant C for all the seven compartments. With this constant we are then able to compute the conductivity, k_i, as a function of the compartmental resistance. Vinje et al. (2020) computed the resistance of the extracellular space to be $R_{ECS} = 0.57$ mmHg/(ml/min), and Holter et al. (2017) found the upper bound for the extracellular permeability, κ_{ECS}, to be 20 nm^2. Using these values for R_{ECS} and κ_{ECS}, and a viscosity $\mu = 0.66$ g/(mm·s) we find the constant C to be $1.38{\cdot}10^{-4}$ m$^-$1.

We will use the constant C in Equation (4.28) to determine the conductivity of most compartments, with the exception of the ECS and the capillaries. The permeability of the ECS was, as stated previously, found by Holter et al. (2017) to be 20 nm^2. In El-Bouri and S. J. Payne (2015), the authors found a lower bound for the permeability of the capillaries to be $1.44{\cdot}10^{-15}$ m^2. The resistivity for the arterial and venous compartments are based on a computation done by Vinje et al. (2020). They used the model of Faghih and Sharp (2018) to estimate the flow resistivity, and found that $R_a = 9.40 \cdot 10^{-4}$ mmHg/(ml/min) and $R_v = 8.15 \cdot 10^{-5}$ mmHg/(ml/min). Vinje et al. (2020) also computed the resistivity of the arterial and venous PVS to be 1.02 mmHg/(ml/min) and $7.90 \cdot 10^3$ mmHg/(ml/min) respectively. Finally, based on the thickness of the capillaries found by El-Bouri and S. J. Payne (2015) and the proposed width of the capillary PVS by Faghih and Sharp (2018), Vinje et al. (2020) computed the resistance of the pericapillary network to be 32.24 mmHg/(ml/min).

In Table 4.2 we have listed our values for each k_i along with the source from which the number was computed. We have operated on the assumption that $\mu_{CSF} = \mu_{ISF} = 3\mu_{Blood}$, where the last equality is a common simplification first done by Tully and Ventikos (2011).

Compartment	**Value** [m^2/(Pa·s)]	**Source**
Arterial	$5.53 \cdot 10^{-14}$	Vinje et al. (2020), Faghih and Sharp (2018)
Capillary	$7.29 \cdot 10^{-13}$	El-Bouri and S. J. Payne (2015)
Venous	$6.37 \cdot 10^{-10}$	Vinje et al. (2020), Faghih and Sharp (2018)
aPVS	$1.70 \cdot 10^{-14}$	Vinje et al. (2020)
cPVS	$5.37 \cdot 10^{-16}$	El-Bouri and S. J. Payne (2015)
vPVS	$2.19 \cdot 10^{-13}$	Vinje et al. (2020)
ECS	$3.04 \cdot 10^{-14}$	Holter et al. (2017)

Table 4.2: The table gives a comprehensive list over the values we used for hydraulic conductivity in our model. The source table show the origin of the numbers used to determine the conductivity.

Deciding transfer coefficients

A vital component of our model is capturing the fluid transfer between compartments. With seven compartments, we have a 7×7 connection matrix containing 49 elements. Compartments do not communicate with themselves, and the transfer coefficient from compartment i to compartment j is the same

as the one from j to i. Hence, we need to determine 21 transfer coefficients. We have listed each nonzero transfer coefficient in Table 4.3.

We have assumed there is no direct connection between the ECS and the vasculature, meaning ω_{ae}, ω_{ce} and ω_{ve} is set to zero. Furthermore, arterial blood has to enter the veins through the capillaries, and the CSF in the arterial PVS has to enter the venous PVS through the capillary PVS. Hence, $\omega_{av} = \omega_{pa,pv} = 0$. Finally, a vascular compartment is assumed to not communicate with the PVS of the other vascular compartments. Therefore, $\omega_{a,pc}$, $\omega_{a,pv}$, $\omega_{c,pa}$, $\omega_{c,pv}$, $\omega_{v,pa}$ and $\omega_{v,pc}$ are all set to zero.

In their article, Vinje et al. (2020) operates with a one dimensional pressure model for the brain during an infusion test. They compute the fluid transfer F_{ij}^{1D} between a compartment i and compartment j by the following formula:

$$F_{ij}^{1D} = \frac{1}{R_{ij}}(p_i - p_j). \tag{4.29}$$

Here, R_{ij} is the fluid transfer rate between compartments. To compute the fluid transfer F_{ij} between the compartments in our three dimensional model, we can integrate the transfer term over the domain. Hence:

$$\begin{aligned} F_{ij} &= \int_\Omega \omega_{ij}(p_i - p_j)d\mathbf{x}, && (4.30)\\ &= \frac{1}{V_\Omega}\int_\Omega\int_\Omega \omega_{ij}(p_i - p_j)d\mathbf{x}\ d\mathbf{x}, && (4.31) \end{aligned}$$

where the second equality holds as F_{ij} is constant in space. By the linearity of the integral, we have:

$$\begin{aligned} F_{ij} &= \int_\Omega \frac{\omega_{ij}}{V_\Omega}\int_\Omega p_i - p_j d\mathbf{x}\ d\mathbf{x}, && (4.32)\\ &= \int_\Omega \omega_{ij}\overline{(p_i - p_j)}d\mathbf{x}, && (4.33)\\ &= \omega_{ij}\overline{(p_i - p_j)}V_\Omega. && (4.34) \end{aligned}$$

Where the overline denotes the average pressure difference between compartments. We assume the average pressure difference between compartments in our model is equivalent to the pressure difference in Equation (4.29). Then, by equating Equation (4.34) and Equation (4.29), we can relate the transfer coefficient ω_{ij} to the one dimensional resistance by the following equation:

$$\omega_{ij}V_\Omega = \frac{1}{R_{ij}}. \tag{4.35}$$

Here, the inter-compartmental pressure differences cancel out by assumption. When determining the transfer between the vascular compartment, we can use the experimental data on the blood flow B into the brain given to us by Anders Eklund and his group at Umeå University. This term can be incorporating by substituting Equation (4.26) for the resistance R_{ij}, giving us:

$$\omega_{ij}\Delta p_{ij}V_\Omega = B. \tag{4.36}$$

Cerebral autoregulation is the phenomenon where the brain ensures that cerebral blood flow remains constant even as the arterial blood pressure changes. According to Paulson, Strandgaard and Edvinsson (1990), cerebral autoregulation works in the range of 60-150 mmHg. Zagzoule and Marc-Vergnes (1986), estimated the capillary pressure to be around 25 mmHg. In addition, Kinoshita et al. (2006) found the venous pressure to be 8-10 mmHg in their measurements of 26 individuals and a difference between ICP and arterial blood pressure of 70 mmHg. Hence, for our compuation of transfer term, we are assuming ICP to be around ten and that the pressure drop from arterial to capillary compartment is 60 mmHg. Furthermore, we also presume the pressure drop from capillaries to veins to be 10 mmHg, and arterial inflow, B, to be 700 ml/min. The latter assumption was made to resemble the arterial inflow rates given to us by Anders Eklund (Qvarlander et al. (2017)). With these numbers, we find the vascular transfer terms listed in Table 4.3.

To determine the transfer coefficients between the PVS and the extracellular space, we will assume that CSF can enter and exit the brain through the astrocytic end feet. These are illustrated in green in Figure 2.2. Vinje et al. (2020) computed the flow resistance through the end feet surrounding the penetrating arteries and veins, and found them to be 0.57 mmHg/(ml/min) and 0.64 mmHg/(ml/min) respectively. Furthermore, they also computed the flow resistance through the capillary wall to be 125 mmHg/(ml/min). Capillary filtration is believed to contribute to, or be the most important source for, CSF production. (Brinker et al. (2014)). Hence, we will assume communication between the capillary and pericapillary compartment and the transfer coefficient is computed similar to that between PVS and ECS. The values for these three transfer coefficients are given in Table 4.3.

Some transfer terms are, however, difficult to determine. To our knowledge, little information exist on the flow resistance between the capillary PVS and the ECS. The exact transfer rate and pressure gradient governing perivascular flow is also not known. Hence, our choices of transfer coefficients for these connections are speculative. We have assumed that the transfer coefficient between the PVS are of the same order of magnitude as the one between the vascular compartments. This is motivated by both in-vivo measurements like those of Mestre et al. (2018) and the glymphatic theory Abbott et al. (2018). In numbers, we have $\omega_{pa,pc} = \omega_{pc,pv} = 10^{-6}$ Pa^{-1}s^{-1}. We have assumed there be little communication between arteries and veins, and their PVS. Hence, the transfer coefficients here are $\omega_{a,pa} = \omega_{v,pv} = 10^{-17}$ Pa^{-1}s^{-1}. Finally, we assumed the transfer coefficient between capillary PVS and ECS to be slightly larger than the one between arteries and arterial PVS, at $\omega_{pc,e} = 10^{-15}$ Pa^{-1}s^{-1}.

Deciding on compliance

We have assumed that the deformations of the brain are negligible during an infusion test, and hence the parenchyma should for our purposes be viewed as near incompressible. While certainly not true, for example CBVf increases during exercise (Huo, Greene and Drew (2015)) and evidence suggest the ECS volume increases during sleep (Xie et al. (2013)), it reduces the computational complexity of our problem. Since we have assumed the brain to be incompressible, we decided on using a low compliance C_i of 10^{-8} Pa^{-1}

Link	**Value** $[\mathrm{Pa}^{-1}\mathrm{s}^{-1}]$	**Source**
$\omega_{a,c}$	$1.25 \cdot 10^{-6}$	Zagzoule and Marc-Vergnes (1986)
$\omega_{c,v}$	$6.01 \cdot 10^{-6}$	Kinoshita et al. (2006)
$\omega_{a,pa}$	10^{-17}	Estimated
$\omega_{c,pc}$	$8.48 \cdot 10^{-10}$	Vinje et al. (2020)
$\omega_{v,pv}$	10^{-17}	Estimated
$\omega_{pa,e}$	$1.86 \cdot 10^{-7}$	Vinje et al. (2020)
$\omega_{pc,e}$	10^{-15}	Estimated
$\omega_{pv,e}$	$1.65 \cdot 10^{-7}$	Vinje et al. (2020)
$\omega_{pa,pc}$	10^{-6}	Estimated
$\omega_{pc,pv}$	10^{-6}	Estimated

Table 4.3: The table gives a comprehensive list over the values we used for the inter-compartmental transfer parameters in our model. All non-listed transfers were set to zero, and $\omega_{ij} = \omega_{ji}$

for all compartments and all patient groups. This is an idealisation, but was chosen due to time constraints.

The porosity of the brain.

The Darcy velocity $\mathbf{q}$ is related to the compartmental velocity $\mathbf{v}$ by the compartmental porosity ϕ_i (see for instance Ray, Iliff and Heys (2019)). The porosity is a volume fraction describing the percentage of the total domain volume which is occupied by the compartment, and we define it as

$$\phi_i = \frac{V_i}{V_\Omega}. \tag{4.37}$$

Where V_i is the volume of the compartment and V_Ω is the total brain volume. If we know the Darcy velocity $\mathbf{q}_i$ and porosity ϕ_i of a given compartment i, we can find the real fluid velocity in the compartment by the following equation:

$$\mathbf{v}_i = \frac{1}{\phi_i}\mathbf{q}_i. \tag{4.38}$$

We will dedicate this section to discussing our chosen values for the compartmental porosity, which are shown in Table 4.4.

Compartment	**Value**	**Source**
ϕ_a	$1.09 \cdot 10^{-2}$	Ito et al. (2001), S.-P. Lee et al. (2001).
ϕ_c	$2.31 \cdot 10^{-3}$	Ito et al. (2001).
ϕ_v	$1.98 \cdot 10^{-2}$	Ito et al. (2001).
ϕ_{pa}	$1.52 \cdot 10^{-2}$	Mestre et al. (2018)
ϕ_{pc}	$2.31 \cdot 10^{-3}$	Pizzo et al. (2018).
ϕ_{pv}	$2.77 \cdot 10^{-2}$	Mestre et al. (2018).
ϕ_e	$1.40 \cdot 10^{-1}$	Xie et al. (2013).

Table 4.4: The table gives a comprehensive list over the values we used for the compartmental porosities.

We will start by discussing the vascular compartments. Perles-Barbacaru and Lahrech (2007) estimated the cerebral blood volume fraction (CBVf) to be 3.3 % of the total brain volume. This is corroborated by Ito et al. (2001) and S.-P. Lee et al. (2001), who in addition observed that the arterial blood constitutes a third of the total cerebral blood volume (CBV). The remaining two thirds of the CBV constitute the combined capillary and venous blood, and it is the belief of Ito et al. (2001) that most of this blood is venous. Hence, we assumed the venous blood to occupy a large portion of this, with capillary blood occupying 7 % of the CBV and the rest being venous blood.

To determine the perivascular porosities, we have estimated the relative size between PVS and vasculature. For the arterial and venous PVS, we have assumed them to be 1.4 times the size of the arteries and veins. This is based on the observations by Mestre et al. (2018), who used in-vivo measurements to determine the width of the surface PVS in mice. For the capillary PVS, we used the observations of Pizzo et al. (2018), who presents a picture of a capillary and its PVS (figure 9D in the article). By measuring the diameter of the combined PVS and capillary, as well as just the capillary, at several points we were able to determine the cross sectional area of the capillary and the PVS. This image suggest that the PVS surrounding the capillaries within the brain have almost the same cross sectional area as the capillaries themselves. As a result, we opted for setting the capillary PVS porosity equal to that of the capillaries. This is on the higher end compared to other simulation studies, such as Kedarasetti, Drew and Costanzo (2021) and Tithof et al. (2022).

Finally, when estimating the porosity of the extracellular compartment, we chose to rely on the observations of Xie et al. (2013), who demonstrated that the extracellular volume fraction of the murine brain was 14 % in awake animals.

4.4 Implementing patient specific data

We have thus far explained the parameters required to implement our model. These parameters have, however, not accounted for individual difference. We possess experimental data of 47 infusion test and their corresponding patient specific geometries. Hence, we are able to tune the CSF pressure at the boundary to match the individual variances measured by Qvarlander et al. (2017). We have built upon the model of Vinje et al. (2020) for intercranial CSF pressure, who assumed a constant infusion rate of 1.5 ml/min.

The infusion rate in infusion tests are however not standardised, and for instance Kahlon, Sundbärg and Rehncrona (2005) infused a CSF-like liquid at a rate of 0.8 ml/min. Hence, the numerical values of plateau pressure is not necessarily comparable between studies. A common quantity of comparison is the outflow resistivity, denoted R_{out}, see for instance Malm and Eklund (2006) and Kahlon, Sundbärg and Rehncrona (2005). We will define the outflow resistance as Kahlon, Sundbärg and Rehncrona (2005), by

$$R_{out} = \frac{p_{plat} - p_{base}}{Q_{inf}}. \tag{4.39}$$

Here, p_{plat} and p_{base} are the plateau and baseline pressures respectively. These can be seen illustrated in Figure 4.2. The model of Vinje et al. (2020), as presented in Section 4.1 has modelled the same ICP curve as is seen in typical

infusion tests. They have, however, still assumed a linear increase in outflow resistance with respect to outflow pressure. Hence, we used linear regression to relate their resistances R_{DS} and R_{crib} to R_{out}.

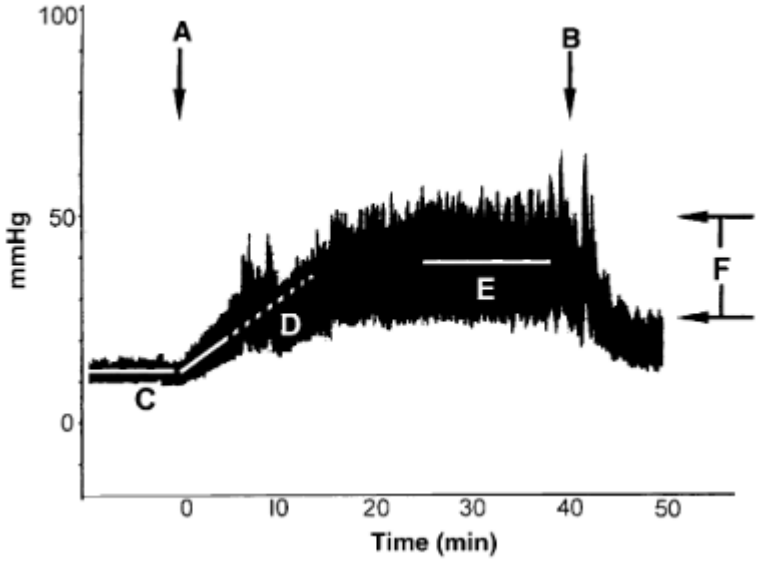

Figure 4.2: The figure shows the recorded intercranial pressure during an infusion. The image is acquired from Kahlon, Sundbärg and Rehncrona (2005). The authors describe the figure as follows: A shows start of infusion, B shows end of infusion, C is pressure plateau pre-infusion and D shows the increase in pressure during infusion. The line marked as E is the average pressure plateau achieved when the new equilibrium is reached, and F shows the exponential drop in ICP once infusion ended.

To be able to perform a linear regression on R_{DS} and R_{crib} as a function of R_{out} we made the assumption that R_{out} relates to R_{DS} and R_{crib} by means of a common scalar α. With this scalar we are able to define two modified resistances $R^*_{AG}\colon \mathbb{R} \to \mathbb{R}$ and $R^*_{crib}\colon \mathbb{R} \to \mathbb{R}$ by

$$R^*_{AG}(\alpha) = R_{AG}\alpha, \tag{4.40}$$
$$R^*_{crib}(\alpha) = R_{crib}\alpha. \tag{4.41}$$

By simulating the CSF pressure for many different values of α, we can compute the resulting R_{out} by Equation (4.39) for each α. We found that a linear fit of

$$R_{out}(\alpha) = 11.27\alpha - 1.24, \tag{4.42}$$

was the best fit to the computed R_{out}. In Figure 4.3, the linear fit is shown alongside the computed values used to make the fit. The fit predicts negative values for very low values of α, and Andersson, Malm and Eklund (2008) raises doubts as to whether the pressure increase is linear after ICP surpasses 26 mmHg. We have, however, chosen to use this fit regardless, as the exact dependence of R_{out} on plateau pressure is, to our knowledge, not known.

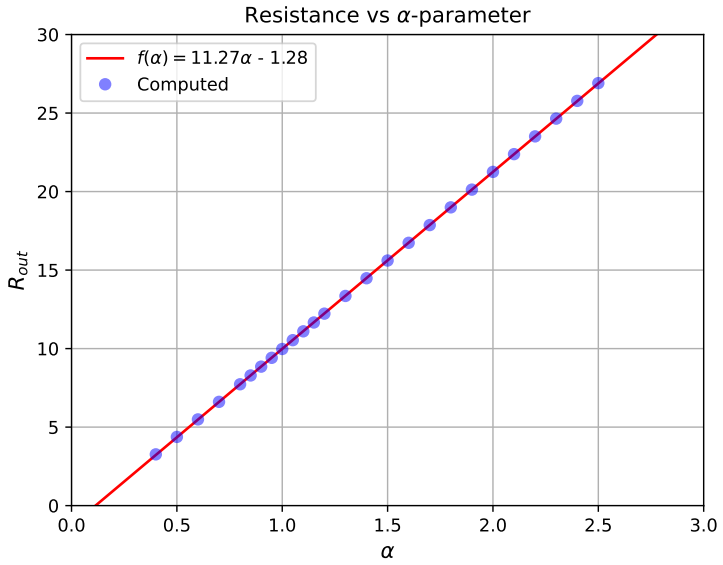

Figure 4.3: In blue, the computed value of R_{out} is shown for a selected number of values of α. The red line show the linear fit that relate the two quantities.

We have, in addition to the patient specific values for R_{out} also measurements of the reference pressure p_{ref} used in Equation (4.21). Some patients had reference pressure exceeded the threshold pressure, p_{tres}, or the CSF pressure, p_{CSF}. On advice by Anders Eklund, the reference pressure was set to be 1 and 2 mmHg lower than the threshold and CSF pressure respectively. A last patient specific tuning was set by applying the measured arterial inflow of each patient.

4.5 Output quantities

Our model yields us seven pressure fields p_i. These pressure fields are, however, defined on the entire parenchyma at each time point t_i. Hence, they are difficult to compare directly. Furthermore, the pressure fields can also be used to find several other quantities of interest. We have in our thesis decided on three separate functionals of interest, namely the volume averaged pressure $\bar{p}_i$, the mean pore speed $\bar{v}_i(t)$ and the inter-compartmental fluid transfer F_{ij}. Each of these quantities are computed over a volume, and we decided on showing the total transfer, and average pressure and speed over the entire parenchyma as well as the grey- and white matter. Our mesh has markers for smaller subdomains. There is, however, little knowledge of how the brain responds to an infusion test, and results from these regions were hard to compare with experimental data. Hence, we opted not to include these in our thesis.

The pressure average $\bar{p}_i^k$ of compartment i in patient k can be computed by an average integral, namely:

$$\bar{p}_i^k(t) = \frac{1}{V_\Omega} \int_\Omega p_i^k(\mathbf{x}, t)\ d\mathbf{x}. \tag{4.43}$$

Here V_Ω is the volume of the integration domain. The average pressure allows us to quantify a systematic pressure difference between compartments. Furthermore, it will also allow us to get a number to the pressure difference between patients. A function $\bar{p}_i^k \colon [0,T) \to \mathbb{R}$ can, unlike a function $p_i^k \colon \Omega \times [0,T) \to \mathbb{R}$, be visualised by a curve, making comparison easier.

Averaging can, however, smooth out local pressure variations. Hence, two compartments can have similar average pressures but radically different pressure field. From Darcy's law in Equation (4.5), we know the compartmental fluid velocity is proportional to the pressure gradient. The fluid velocity is in other words an expression of the pressure variations in the field. Furthermore, the glymphatic hypothesis relies on convective transport of solutes, and the topic of perivascular CSF and extracellular ISF flow has been a popular topic as a result (Holter et al. (2017), Tithof et al. (2022), Abbott et al. (2018), Iliff, M. Wang, Liao et al. (2012) and Ray, Iliff and Heys (2019)). The pore velocity defined in Equation (4.38) is the velocity at which the fluid flows in nature. We will refer to pore velocity whenever we discuss velocity unless otherwise stated. As with pressure, we are going to compare the volume averaged pore speeds, and not the velocity fields themselves. The mean speed $\bar{v}_i^k$ within a given volume Ω in compartment i and patient k is given by:

$$\bar{v}_i^k(t) = \frac{1}{V_\Omega} \int_\Omega \frac{k_i}{\phi_i} \sqrt{\nabla p_i^k \cdot \nabla p_i^k} d\mathbf{x}. \tag{4.44}$$

Our final quantity of interest is the inter-compartmental fluid transfer rate. The transfer term $\omega_{ij}(p_i - p_j)$ has units s^{-1}, and by integrating the term over a volume Ω, we find the volume flux F_{ij}^k from compartment i to compartment j in patient k to be:

$$F_{ij}^k = \int_\Omega \omega_{ij}(p_i^k - p_j^k)\ d\mathbf{x}. \tag{4.45}$$

Unlike that of pressure and speed, the fluid transfer F_{ij} is not averaged but shows the total fluid transport. As each compartment communicates with its connections on the entire domain, and most compartments have several connections, the fluid velocities themselves can not be used to determine where the fluid flows to. Hence, to verify if mass is conserved and to investigate the flow patterns of cerebral fluids, computation of the fluid transfer term is vital.

We will employ our model on a total of 47 seven patients in two groups. Hence, showing the curves for each patient would make the figures in Chapter 7 too crowded to be legible. Instead, we will show the curves for each group in separate sub-figures, and for each group only show the group average and the lowest and highest observed value at each time point t_i. Furthermore, the amount of data processed made it impossible to store the system state at all time points. Hence, only every tenth time step was saved and since post-processed. To make the text easier to read, we will refer to the volume averaged pressure and volume average speed as the pressure and speed of a patient. Whenever we state the average speed, average pressure or average transfer rate, we refer to the average within a group, i.e. for a compartment i and a group index set $\mathcal{I}_G$, the average pressure $\bar{p}_i$ is defined as:

$$\bar{p}_i = \frac{1}{N} \sum_{k \in \mathcal{I}_G} \bar{p}_i^k. \tag{4.46}$$

The same formula applies for the group speed average and group transfer average.

4.6 Software and implementation.

The model was implemented using the finite element software FEniCS, (Logg, Mardal and Wells (2012) and Alnæs et al. (2015)). All code is available at github in the following directory: https://github.com/larswd/Code_NPH_thesis. Raw data from simulations can be made available upon request via email: larswd@gmail.no.

CHAPTER 5

Meshing

This chapter is dedicated to the meshing process. We discuss our dataset of patients, how errors in segmentation was corrected and the software used in the meshing pipeline. Lastly, we also discuss the generation of a partial mesh used to measure sensitivity to spatial and temporal resolution.

The meshing pipeline

We have in our possession 47 MRI images of the human brain performed by the group of Anders Eklund. Of these, 33 of them are healthy individuals constituting the control group, while the remaining 14 are patients diagnosed with iNPH. FEniCS is not able to compute on MRI images directly, and hence we need to transform the images to mesh files. In this section, we will rely on Mardal, Rognes et al. (2022), a book written about mesh generation from MRI images.

Our model places boundary conditions on the pial and ventricular surfaces. It is therefore of vital importance that the computational mesh accurately capture these surfaes. The MRI images were segmented using FreeSurfer (Biomedical Imaging (2021)) by Karen-Helene Støverud at SINTEF Digital. We were able to inspect the segmentations using FreeView, a software developed by FreeSurfer to graphically inspect MRI files and subsequent segmentations. This inspection revealed that the pial markings in were satisfactory and were left as they were.

In most patients, however, the ventricles were incorrectly segmented. This was especially true for patients had a tilted head or enlarged ventricles, the segmentation algorithm struggles with correctly identifying the region. This phenomenon is seen in Figure 5.1 where the red and purple coloured area shows the segmented left and right lateral ventricles respectively. At the back of the brain, a significant black spot is seen in the brain image. T1-imaging, the imaging technique used to generate this image and all MRI images used to generate our meshes shows CSF in black. Hence, a large part of the lateral ventricles are not segmented by the FreeSurfer algorithm, and required manual correction. The errors in Figure 5.1 were corrected by hand using the *Voxel Edit* tool in FreeView. The only pixels to be coloured was those that either was unsegmented, or those where the background was fully black. If a grey or dark grey pixel was marked as tissue, then the pixel would not be edited. An illustration of the colouring process is seen in Figure 5.2, where the dark areas in the top left was coloured while the choroid plexus in cyan was left untouched. The MRI images have a spatial resolution of 1 mm^3, and hence the

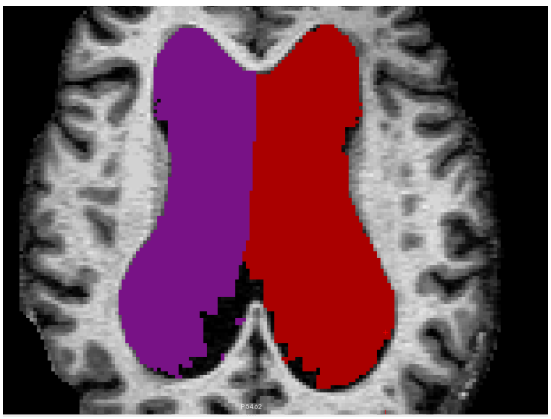

Figure 5.1: The figure shows a faulty segmentation of the lateral ventricles of a patient. The purple region highlights the freesurfer-segmented right lateral ventricle, while the red region highlights the segmented left one. The large dark spots visible inside the parenchyma is likely to be ventricles as well, as water filled cavities show up as dark spots in T1-weighted MRI imaging.

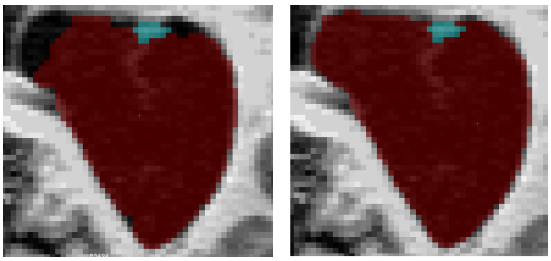

Figure 5.2: The figure to the left shows the image of an uncorrected axial slice of a patient. Here, red shows the area segmented as left lateral ventricle, while cyan highlights the area segmented as choroid plexus. There is a significant black spot connected to the coloured part of the ventricle. The right image shows the corrected axial slice, and most of the dark spots are now marked red. On the top left there is an uncoloured dark area, which was left untouched as there is a clear wall of tissue separating the area from the ventricle.

spatial resolution of the MRI images is not always fine enough to capture the ventricles in detail. In particular, the lateral ventricles have a tail, as can be seen in Figure 2.1. This tail was, for certain patients difficult to impossible to capture in detail. In Figure 5.3, we see the segmented right lateral ventricle (purple), the segmented right choroid plexus (cyan) and a possible candidate or the tail of the right lateral ventricle in a red circle. The possible candidate was not coloured due to it being only a couple of pixels wide and only slightly darker than the white matter tissue surrounding it.

The next and final step in the meshing pipeline was to construct a FEniCS compatible mesh from our corrected MRI images. This was accomplished using the software SVMTK, a python3 package developed by L.-M. Valnes and Schreiner (2021). To create the meshes, we followed the procedure outlined in

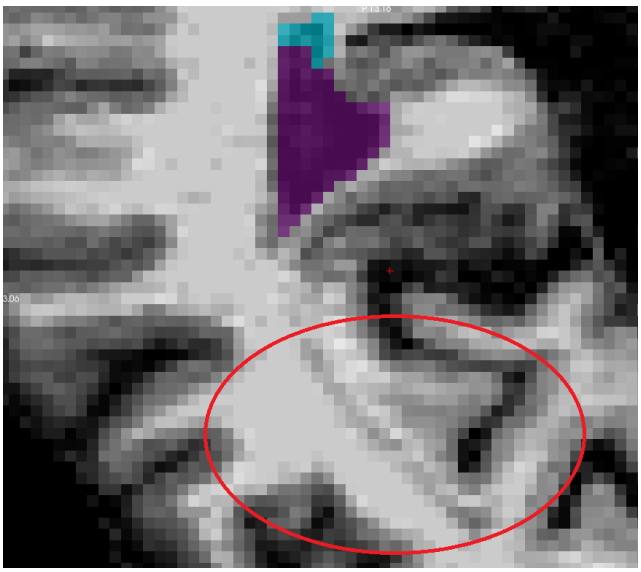

Figure 5.3: A possible candidate for the tail of the right lateral ventricle is shown within the red circle. The final segmented part of the ventricle is shown in purple and cyan highlights the right choroid plexus.

Mardal, Rognes et al. (2022), where we first constructed surface files on the stl-format for the pial and white matter surfaces for both the cerebrum and cerebellum, as well as the ventricle surfaces and the brainstem. With these surfaces, we were able to generate the outline of our domain by telling SVMTK which sections to label as grey matter, white matter or brain stem. Finally, this mesh was converted to a h5-file format which we could open and read in FEniCS.

Partial meshing for convergence estimation

In the Finite Element Method, a well known result is that the numerical error E is bounded by

$$E \leq Ch^{p+1}, \tag{5.1}$$

where C is a constant, h is the mesh resolution in terms of element length and p is the order of the basis Lagrange polynomials. This is, for instance, shown in Mardal and Logg (2021). This relationship between the error and mesh resolution suggest a possible lower bound on mesh resolution if we wish to avoid a significant extra insecurity in our results. The error in Equation (5.1) goes to zero as $h \to 0$, but computational cost increases with a finer mesh resolution. Hence, it is important to find a combination of h and p such that E is smaller than the uncertainty from the estimation of parameters and boundary conditions, but without making simulations prohibitively expensive.

To do so, we created a test mesh where only a small part of the total brian volume was used in the mesh generation. SVMTK allows for extraction of the surface of any region in the lookup table of freesurfer. Hence we used FreeView to select two connected regions in the brain, one grey matter and one white

matter region. These had the Freesurfer tags of "2029 ctx-rh-superiorparietal" and " 4029 wm-rh-superiorparietal", and can be seen in Figure 5.4. Using the

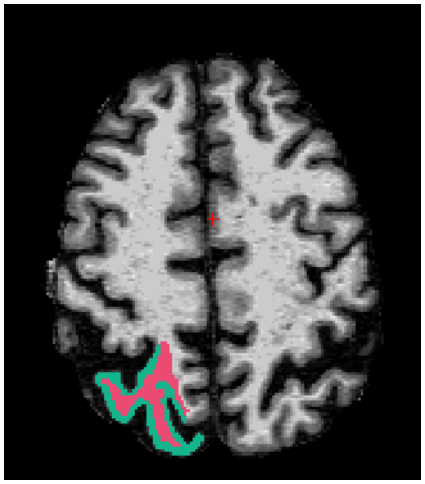

Figure 5.4: The figure shows the brain of patient C25, with the superior parietal cortex and white matter highlighted in green and pink respectively. The small selection allows us to compute on a much finer mesh on a home computer than what would be possible if the whole brain was used. The program used to visualise the brain was FreeView.

same meshing pipeline as discussed in the previous subsection, we were able to generate meshes with resolution parameters (RPn) of 8, 16, 32, 64 and 96. The resolution parameter is an argument sent to some SVMTK commands, and is a number setting a a lower bound on the ratio of mesh circumference to cell size. Hence, a high RPn gives a finer mesh while a low RPn correleates to a rougher mesh. In Figure 5.5, a partial mesh with RP64 is shown. Furthermore, the difference between meshes with between the resolutions are shown in figures 5.6 and 5.7, which show the node and cell density of a mesh with RP64 and RP16 respectively.

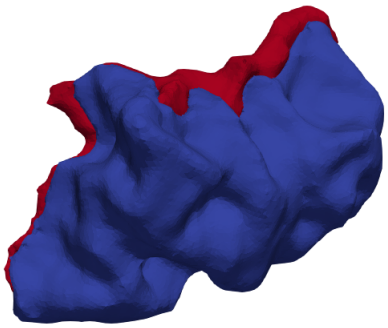

Figure 5.5: The figure shows the mesh generated from the selected parts of the brain of patient C25. The mesh, generated using SVMTK, shows cortex in blue and white matter in red. This mesh was generated with RP64.

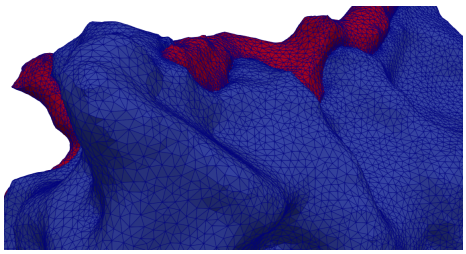

Figure 5.6: The figure shows the mesh generated from the selected parts of the brain of patient C25 with a grid showcasing nodes and element edges. The mesh, generated using SVMTK, shows cortex in blue and white matter in red. This mesh was generated with RP64.

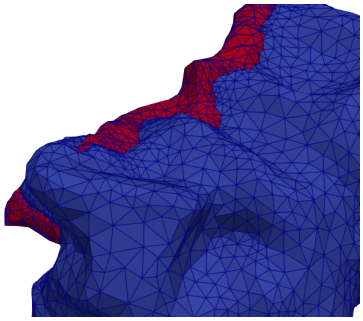

Figure 5.7: The figure shows the mesh generated from the selected parts of the brain of patient C25 with a grid showcasing nodes and element edges The mesh, generated using SVMTK, shows cortex in blue and white matter in red. This mesh was generated with RP16.

CHAPTER 6

Model verification

In this chapter we present how we have verified our model and what results that gave us. We start by presenting how we chose mesh resolution and how we made sure that the spatial discretisation error was negligible. Thereafter, we discuss how we measured the requirement for time resolution for our model. Finally, we then discuss the model's sensitivity to parameter changes.

6.1 Resolution sensitivity tests

We implemented our model on the partial meshes described in Chapter 5. We tested CG1 polynomials on the resolutions RP8, RP16, RP32, RP64 and RP96. Second order polynomials were tested with resolutions RP8, RP16 and RP32. This yielded the extracellular pressure during infusion shown in Figure 6.1. A similar trend is observed in all compartments, and illustrated by venous pressure inFigure 6.2 and venous PVS pressure in Figure 6.3. The average pressures follow the same trend in all compartments, namely that the average compartmental pressure increase with resolution and basis polynomial order. A general trend emerges where all pressures computed with CG2 and CG1 pressures with RP64 or greater are close together. The CG1 pressures with RP32, RP16 or RP8 on the other hand are notably lower than the rest. As the CG2 polynomials showed convergence at lower resolutions, we decided to use CG2 and RP32 in our simulations.

In our measurements on time resolution sensitivity, we decided to use CG1 polynomials and RP32 on the entire brain mesh. Then, for a selection of different time step values we computed the pressure in all compartments. The pressure in the venous compartment is seen in Figure 6.4 and the ECS pressure is shown in Figure 6.5. The curves suggest that a time step of at most 20 seconds is required for accurate results.

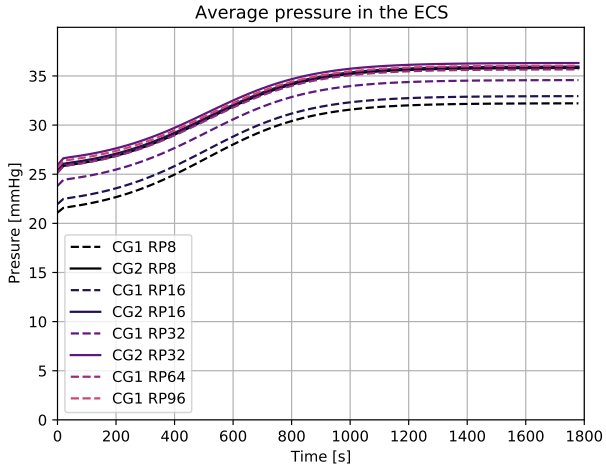

Figure 6.1: Average ECS pressure over the partial C25 mesh with inflow velocity at $Q_{in} = 712.15$ ml/min and several different resolutions. Dashed lines indicate first order Lagrange polynomials, whole lines are second order basis polynomials.

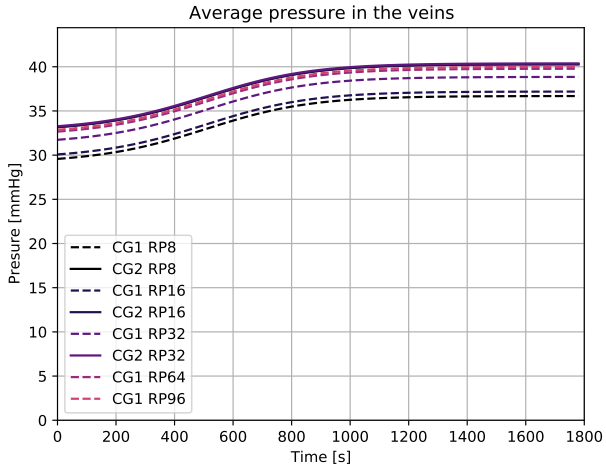

Figure 6.2: Average venous pressure over the partial C25 mesh with inflow velocity at $Q_{in} = 712.15$ ml/min and several different resolutions. Dashed lines indicate first order Lagrange polynomials, whole lines are second order basis polynomials.

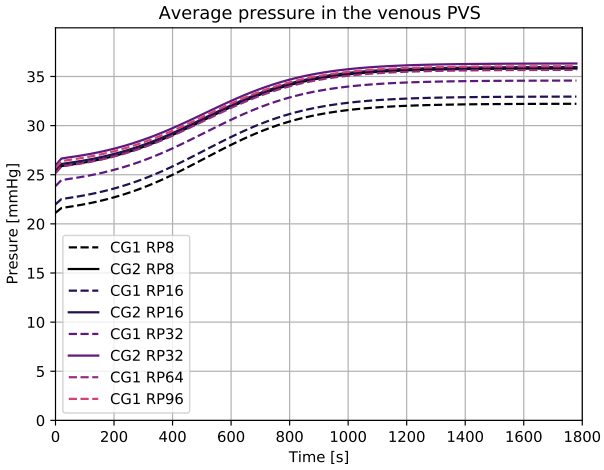

Figure 6.3: Average venous PVS pressure over the partial C25 mesh with inflow velocity at $Q_{in} = 712.15$ ml/min and several different resolutions. Dashed lines indicate first order Lagrange polynomials, whole lines are second order basis polynomials.

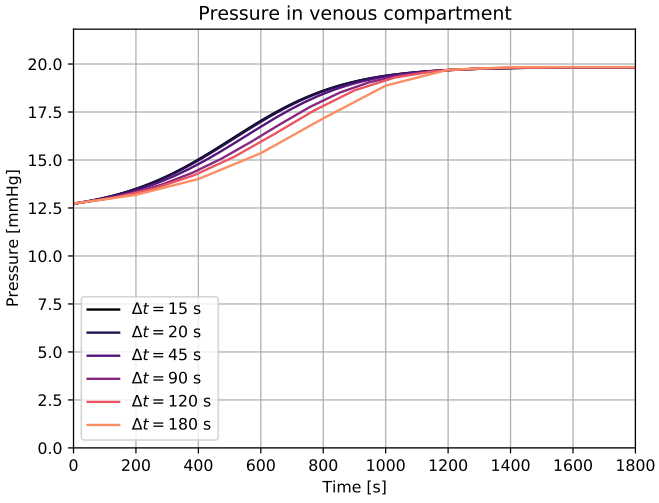

Figure 6.4: The figure show average venous pressure over the entire C25 mesh with inflow velocity at $Q_{in} = 712.15$ ml/min and CG1 basis polynomials with RP32, for a selection of time steps Δt.

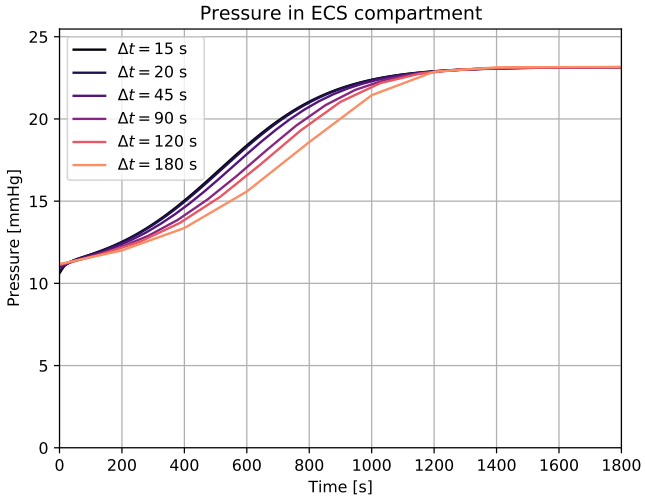

Figure 6.5: The figure show average ISF pressure over the entire C25 mesh with inflow velocity at $Q_{in} = 712.15$ ml/min and CG1 basis polynomials with RP32, for a selection of time steps Δt.

6.2 Sensitivity to changes in arterial inflow

The data we possess from Qvarlander et al. (2017) show large interpersonal variance. Hence, we decided on assessing the importance of this quantity before running simulations on all patients. To do so, we chose to run the simulations on the mesh of the entire brain parenchyma of patient C25 with RP16. We chose to do one simulation at the average inflow velocity of the control group, namely $B_{in} = 712.5$ ml/min. Furthermore, four more simulations was done with B_{in} plus/minus one and two standard deviations. The standard deviation for arterial inflow in the control group is 172,4 ml/min. The change in average pressure in the extracellular and perivascular were for all intents and purposes constant with respect to arterial inflow rate. In Figure 6.6 we see little variation in ECS pressure as arterial inflow is changed. The vascular compartments respond more strongly to these changes, as can be seen in Figure 6.7.

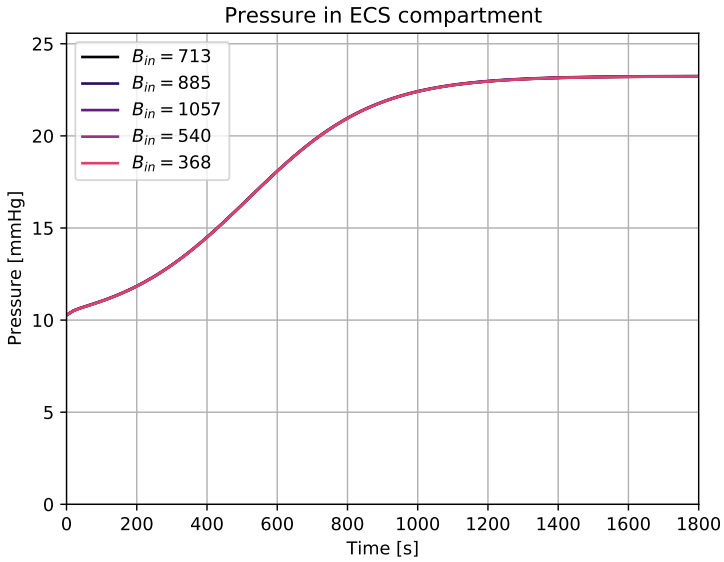

Figure 6.6: Average ECS fluid pressure over the entire brain parenchyma in C25 for different arterial inflow rates. Average inflow rate was 712.5 ml/min, and the curves show the pressure at the average and plus/minus both one and two standard deviations.

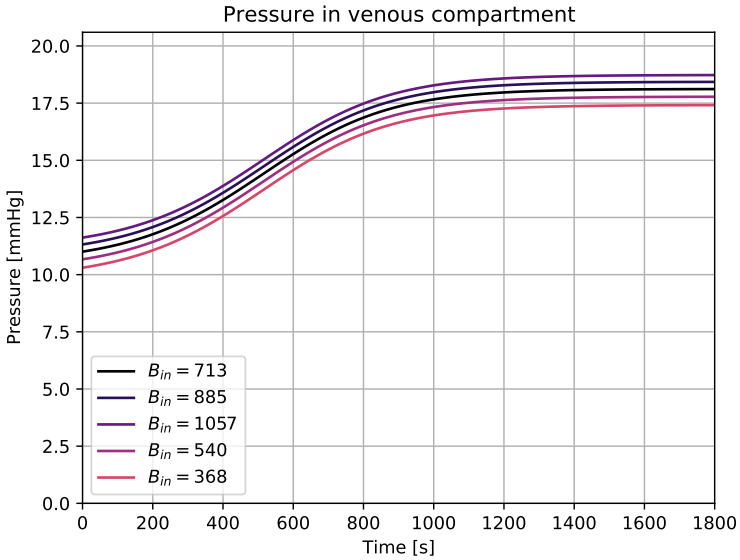

Figure 6.7: Average venous fluid pressure over the entire brain parenchyma in C25 for different arterial inflow rates. Average inflow rate was 712.5 ml/min, and the curves show the pressure at the average and plus/minus both one and two standard deviations.

CHAPTER 7

Results

In this chapter, we present our main findings. The chapter is divided into two sections. In the first section , we will present how both the control and the iNPH groups responded to the infusion test subject to the same boundary conditions. We will present the findings for a selection of the compartments, one candidate from the vascular system, one from the perivascular system and the results from the extracellular space. For each of the selected compartments, we will present the average pressure within the compartment, the average velocity and the inter-compartmental transfer. These results will be given for the entire brain parenchyma, the grey matter and the white matter. The second section is dedicated to how the groups responded to patient specific boundary conditions. As with section one, data for average pressure, average speed and total transfer rate is presented. As stated in Section 4.5, we will, for the sake of brevity sometimes refer to the volume averaged pressure and volume averaged speeds as just pressure and speed.

7.1 Results under one model

The first set of simulations were done using the same applied CSF pressure on all patients, where we used the values for outflow resistance and reference pressure from Vinje et al. (2020) in Equation (4.20). Arterial inflow rate was set at 712.5 ml/min for the control group and 653.4 ml/min for the iNPH group, which are the average inflow rates for the group. These simulations initiates the infusion at $t = 0$ s, and the simulations end at $t = 1800$ s.

Pressure development during infusion

The pressure increased in all compartments after infusion began. In the extracellular space, the pressure rose from an average of 10.2 mmHg and 10.3 mmHg to 22.3 and 22.2 mmHg at the end of infusion in the control and iNPH groups respectively. A similar trend is also observed in the perivascular spaces, and as an example the pressure in arterial PVS is shown in Figure 7.1b. In the arterial PVS, the pressure rose from 10.3 mmHg and 10.2 mmHg to 22.3 mmHg and 22.2 mmHg in the control and iNPH groups in that order. The pressure in the grey and white matter was, on average, at the same level in the grey and white matter in the ECS. The ISF pressure in these regions is shown Figure 7.2a and Figure 7.2b, where the pressure plateaues at 22.2 mmHg in both regions for the control group. The difference is larger in the iNPH

group, where the grey matter pressure was 22.2 mmHg, while the white matter pressure was 22.0 mmHg. The arterial PVS pressure in the grey and white matter follow the same trend as the ECS pressures. The pressure plateaues at 22.3 mmHg in both regions for the control group, while in the iNPH group the grey matter pressure was 22.4 mmHg and the white matter pressure 22.1 mmHg. Pressure differences between groups were of a similar magnitude in all perivascular compartments, and hence only the arterial PVS pressure is shown here.

The arterial compartment, however, has larger differences between the grey and white matter pressures at all points during the simulation. The arterial pressure is shown in Figure 7.4a, while the arterial grey matter pressure is shown in Figure 7.4b. The volume averaged pressure in the arterial compartment was, at the end of infusion, on average 83.4 mmHg and 80.7 mmHg in the control and iNPH groups. In the grey matter, these numbers were 101 mmHg and 93.6 mmHg. In the white matter, the arterial pressure was 65.6 mmHg and 64 mmHg at the end of infusion.

In Figure 7.5 we see the pressure field in the extracellular spaces of patients C25 and NPH1 at $t = 1400$ s after infusion start. A total pressure difference of 2 mmHg between the highest and lowest observed values is found in both patients. The highest pressures are alongside the cortex, but so are the lowest values. Hence the biggest pressure gradients are in the grey matter, while the pressure field is more uniform in the white matter. The perivenous pressure field is illustrated in Figure 7.6 at the same point in time for the same two patients. Unlike the ECS, the pressure is the lowest at the boundary. The pressures range from 22.64 mmHg at the highest to 20.2 mmHg at the lowest, and both extremes are found in NPH1. The venous PVS pressure field is similar to the one in the venous field, shown in Figure 7.7, in that the pressure is lower on the pial boundary. Unlike the venous PVS, however, the venous pressure gradients are significantly steeper. The pressure at the ventricular boundary are at 21.30 mmHg in C25 and 20.59 mmHg in NPH1. At the cortical boundary, the pressures are 16.41 mmHg and 16.37 mmHg in the control and NPH group respectively.

While not all pressure curves are shown, the average value within each group for the volume averaged pressure in all regions is shown in Table 7.1.

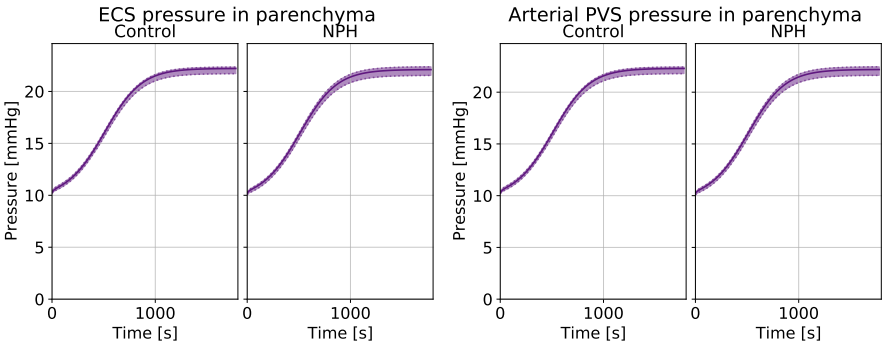

(a) (b)

Figure 7.1: The ECS and arterial PVS had similar pressure curves before and after infusion. In figure (a) we see the computed average extracellular pressure in the whole of the brain's extracellular space. The pressure increases from 10.3 mmHg and 10.2 mmHg to 22.2 mmHg and 22.1 mmHg in the control and iNPH group respectively. Figure (b) on the other hand show the volume averaged pressure in the arterial PVS. The pressure plateaus at 0.1 mmHg higher than the ECS pressure in each group, namely 22.3 mmHg in the controls and 22.2 in the iNPH group. The whole line show the group average, while the dashed lines show the highest and lowest computed value at the given time point.

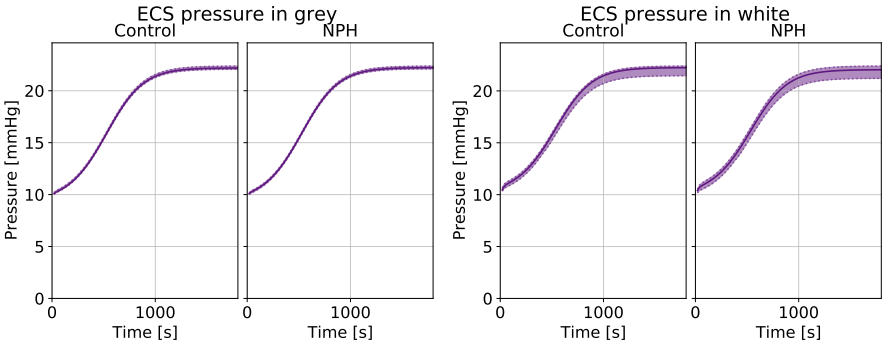

(a) (b)

Figure 7.2: The volume averaged ECS pressures were similar in the grey and white matter. In figure (a) we see the computed average extracellular pressure in the grey matter. Figure (b) on the other hand show the pressure in the white matter. In both regions, the pressure increases by 12 mmHg over the 1800 second long infusion time. The whole line show the group average, while the dashed lines show the highest and lowest computed value at the given time point. A time step of $\Delta t = 20$ s was used, and every tenth time step was stored during simulations.

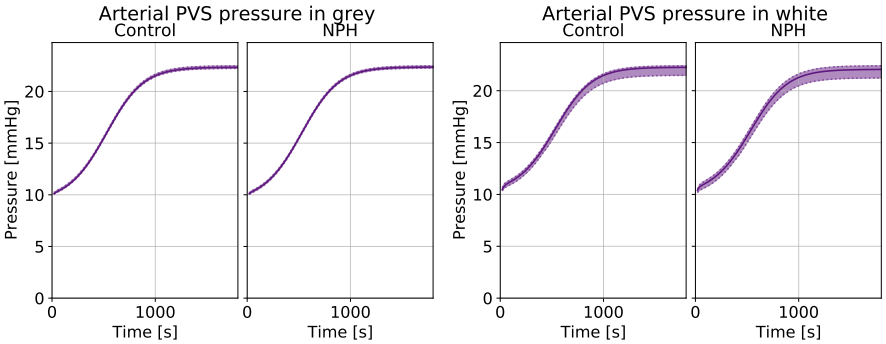

(a) (b)

Figure 7.3: The volume averaged ECS pressures were similar in the grey and white matter. In figure (a) we see the computed average extracellular pressure in the grey matter. Figure (b) on the other hand show the pressure in the white matter. In both regions, the pressure increases by 12 mmHg over the 1800 second long infusion time. The whole line show the group average, while the dashed lines show the highest and lowest computed value at the given time point. A time step of $\Delta t = 20$ s was used, and every tenth time step was stored during simulations.

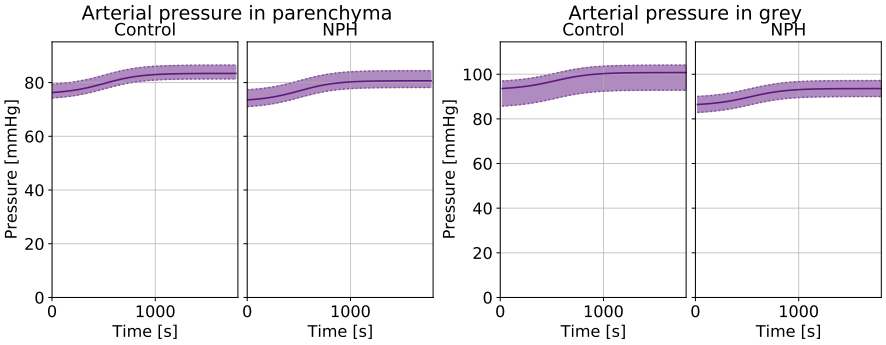

(a) (b)

Figure 7.4: The volume averaged arterial pressures were similar in the grey and white matter. In figure (a) we see the computed average extracellular pressure in the grey matter. Figure (b) on the other hand show the pressure in the white matter. In both regions, the pressure increases by 7.2 mmHg over the 1800 second long infusion time. The whole line show the group average, while the dashed lines show the highest and lowest computed value at the given time point. A time step of $\Delta t = 20$ s was used, and every tenth time step was stored during simulations.

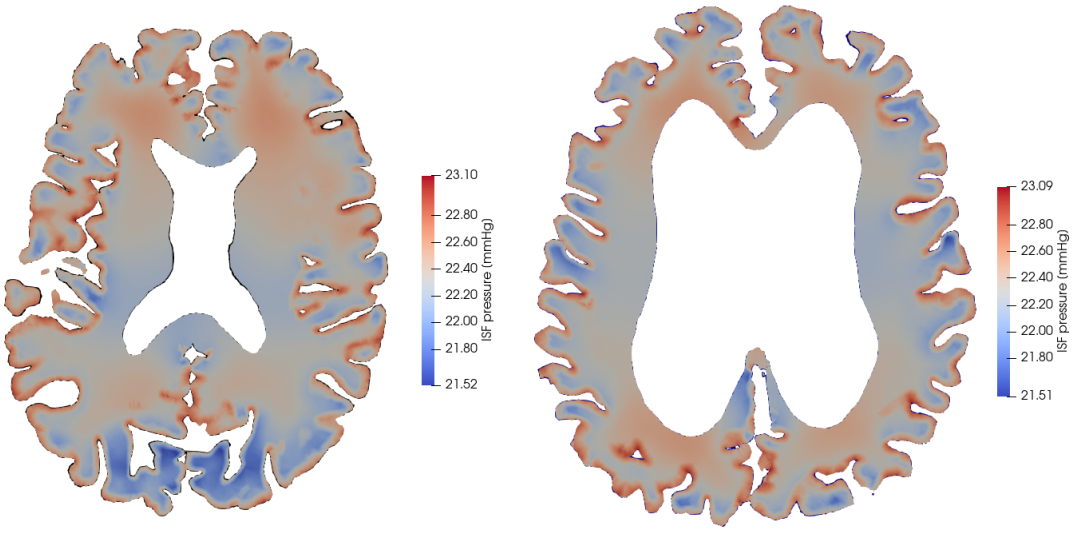

Figure 7.5: The pressure field in the extracellular space of patients C25 (left) and NPH1 (right) in a 2D slice of the brain parenchyma. The slice show the pressure at $t = 1400$ s. In both patients, the pressure ranges from 23.1 mmHg at the cortex and falls to 21.5 mmHg at its lowest value.

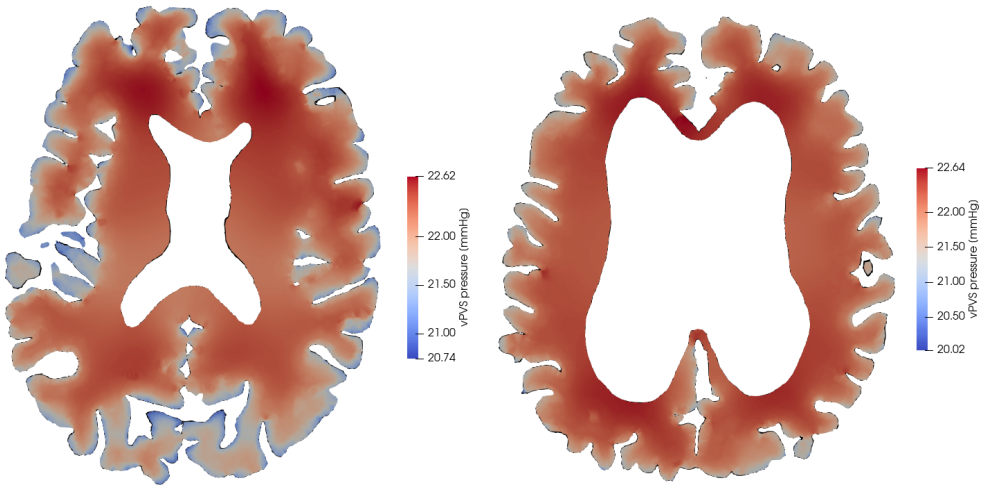

Figure 7.6: The pressure field in the venous PVS of patients C25 (left) and NPH1 (right) in a 2D slice of the brain parenchyma. The slice show the pressure at $t = 1400$ s. In both patients, the pressure ranges from 22.6 mmHg at the cortex in both groups and falls to 20.7 and 20.2 mmHg at its lowest value in the control and iNPH group respectively.

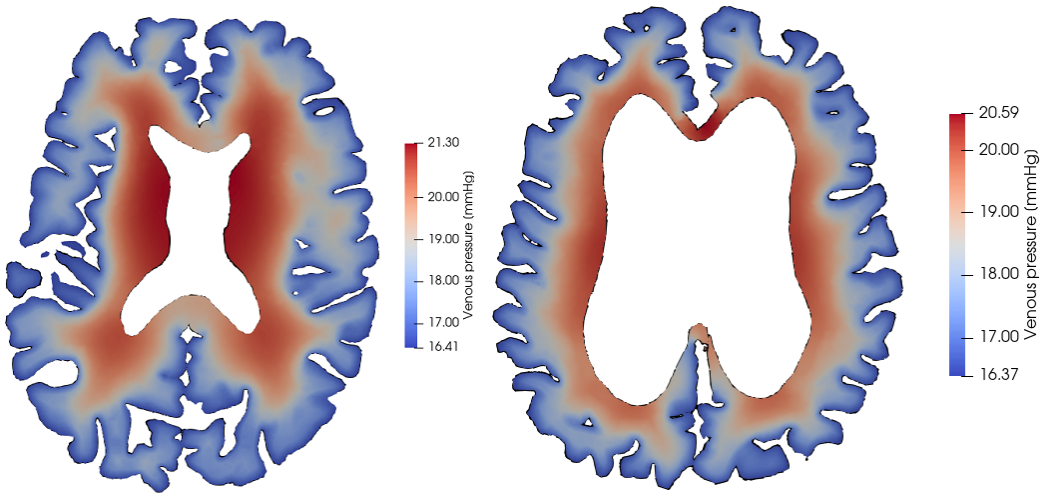

Figure 7.7: The pressure field in the venous compartment of patients C25 (left) and NPH1 (right) in a 2D slice of the brain parenchyma. The slice show the pressure at $t = 1400$ s. In both patients, the pressure ranges from 16.4 mmHg at the cortex in both groups. The pressure is highest in the white matter, where it reaches 21.3 mmHg and 20.6 mmHg in the control and iNPH group respectively.

Average compartmental pressure at the end of infusion [mmHg]

Compartment	Parenchyma		Grey Matter		White Matter	
Arterial	83.4	80.1	93.6	86.4	65.5	64.0
Capillary	29.5	28.8	31.8	30.5	27.1	26.6
Venous	18.2	18.0	17.4	17.4	19.0	18.8
Arterial PVS	22.3	22.2	22.3	22.4	22.3	22.1
Capillary PVS	22.2	22.1	22.2	22.2	22.2	22.0
Venous PVS	22.1	22.0	22.0	22.0	22.2	22.0
ECS	22.2	22.1	22.2	22.2	22.2	22.0

Colour code	
Control group	iNPH group

Table 7.1: Average pressure in each compartment at the end of infusion for both the control group (blue) and the iNPH group (beige). Units are in mmHg.

Fluid velocities within compartments

During infusion, the pressure in all compartment rises and with it the pressure gradient increases as well. We will, as outlined in Section 4.5, refer to the compartmental volume averaged pore speed as the compartmental speed in this section. In Figure 7.8a we see the curves for the speed in the extracellular compartment, the initial speed was 2.0 nm/s for both groups. At $t = 1800$ s these speeds had risen to an average of 6.8 nm/s and 6.3 nm/s for the iNPH group and the control group respectively. Fluid moves faster in the PVS than in the ECS, illustrated by the arterial PVS in Figure 7.8b. At the start of infusion, the average speed in the arterial PVS was 12.5 nm/s in both groups. The speed in the arterial PVS plateaued at 139 nm/s in the control group and 143 nm/s in the iNPH group.

The ISF speed is higher in the grey matter than in the parenchyma as a whole, as can be seen in Figure 7.9a. The fluid speed is higher in the control group than the iNPH group, with the average group member having a speed of 10.8 nm/s in the grey matter for controls and 10.3 nm/s for iNPH patients. In the white matter, the fluid speeds are significantly lower, which is shown in Figure 7.9b. The interpersonal variance in white matter is a lot greater than in the grey matter and in the parenchyma as a whole, with values ranging from one to four nm/s in both groups. In the grey matter and the parenchyma as a whole, however, the largest computed fluid speed in each group were only 20-30 % larger than the smallest. Yet as can be seen in Figure 7.8a, the overall lower fluid speed in the white matter makes the large variance in the white matter negligible on the ECS fluid speed as a whole. moves significantly slower in the white matter than in the grey matter, this big interpersonal variance is not reflected when considering the parenchyma as a whole.

As with the extracellular space, the average fluid speed is greater in the grey than in the white matter in the PVS, see Figure 7.10a and Figure 7.10b. The interpersonal variance in the white matter is smaller in the arterial PVS than in the ECS, but we still see a 200% increase from smallest to greatest. In the arterial PVS grey matter we observe a top speed of 272 nm/s. The fluid velocity in the venous PVS follows the same trend as the ECS, but with the magnitude of the arterial PVS. Hence, the figure is not shown, but the plateau speed in the venous PVS was 163 nm/s in the control group and 176 nm/s in the NPH group. Lastly, the speed in the capillary PVS was 7.6 nm/s and 8.0 nm/s in the control and iNPH groups respectively at t= 1800 s.

The speed in the vascular compartments remained stable throughout the simulation, as can be seen in Figure 7.11a. At both the start and end of the simulation, arterial blood speeds were 3.32 mm/s and 3.02 mm/s. Fluid speeds were higher in the arterial grey matter, where the blood moved at a speed of 4.35 mm/s in the average control patient, and 3.76 mm/s in the average iNPH patient. While not all speed curves are shown, the average speed in each compartment in every region of interest at the end of infusion is shown in Table 7.2. Furthermore, using Equation (4.44) with the speed values listed in Table 7.2, we computed the average pressure gradients which are listed in Table 7.3.

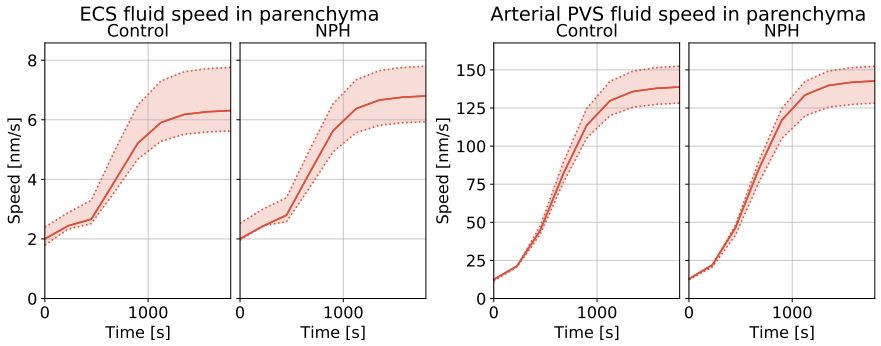

(a) (b)

Figure 7.8: Fluid in the ECS moved significantly slower than in the arterial PVS. In figure (a) we see the computed average extracellular fluid speed in the whole of the brain's extracellular space. Figure (b) on the other hand show the volume averaged pore speed in the arterial PVS. The whole line show the group average, while the dashed lines show the highest and lowest computed value at the given time point. A time step of $\Delta t = 20$ s was used, and every tenth time step was stored during simulations.

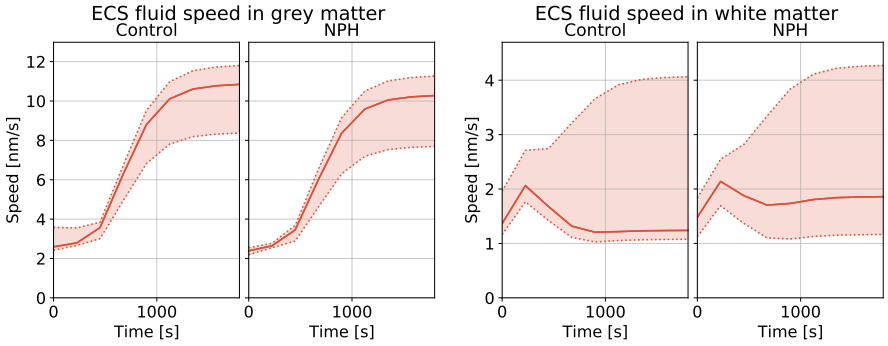

(a) (b)

Figure 7.9: Fluid in the ECS moved quicker in the grey than in the white matter. In figure (a) we see the computed average extracellular fluid speed in the grey matter, while figure (b) on the other hand show the speed in the white matter. The simulation ended at $t = 1800$ s. The whole line show the group average, while the dashed lines show the highest and lowest computed value at the given time point. A time step of $\Delta t = 20$ s was used, and every tenth time step was stored during simulations.

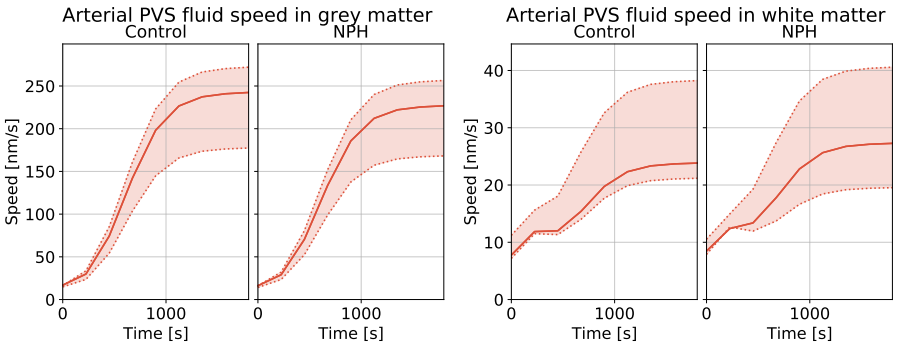

(a) (b)

Figure 7.10: Fluid in the ECS moved quicker in the grey than in the white matter. In figure (a) we see the computed average arterial PVS fluid speed in the grey matter, while figure (b) on the other hand show the speed in the white matter. The simulation ended at $t = 1800$ s. The whole line show the group average, while the dashed lines show the highest and lowest computed value at the given time point. A time step of $\Delta t = 20$ s was used, and every tenth time step was stored during simulations.

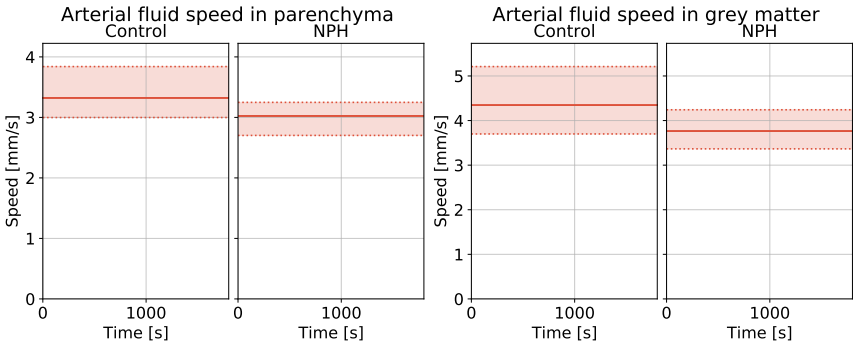

(a) (b)

Figure 7.11: Fluid in the penetrating arteries remained stable throughout the simulation. In figure (a) we see the computed average arterial fluid speed in the whole of the brain parenchyma. Figure (b) show the volume averaged pore speed in the arterial grey matter. The whole line show the group average, while the dashed lines show the highest and lowest computed value at the given time point. Average blood speed is 1 mm/s higher in the grey matter than in the parenchyma as a whole. A time step of $\Delta t = 20$ s was used, and every tenth time step was stored during simulations.

Average compartmental fluid speed at the end of infusion

Compartment	Unit	Parenchyma		Grey Matter		White Matter	
Arterial	mm/s	3.32	3.02	4.35	3.76	2.23	2.06
Capillary	μm/s	15.8	14.4	20.2	17.6	11.3	10.2
Venous	mm/s	1.27	1.16	1.70	1.45	0.80	0.76
Arterial PVS	nm/s	139	143	242	227	23.8	27.3
Capillary PVS	nm/s	7.6	8.0	13.1	12.3	1.5	1.9
Venous PVS	nm/s	163	176	263	243	51.2	71.7
ECS	nm/s	6.3	6.8	10.8	10.3	1.2	1.9

Colour code	
Control group	iNPH group

Table 7.2: Average speed in each compartment at the end of infusion for both the control group (blue) and the iNPH group (beige). Fluid flow happen on several different orders of magnitude, and hence the units are shown in a separate column.

Average compartmental pressure gradient at the end of infusion [mmHg/mm]

Compartment	Parenchyma		Grey Matter		White Matter	
Arterial	4.90	4.46	6.43	5.55	3.29	3.04
Capillary	0.54	0.49	0.69	0.60	0.38	0.35
Venous	0.28	0.26	0.38	0.32	0.18	0.17
Arterial PVS	0.94	0.96	1.63	1.53	0.16	0.18
Capillary PVS	0.35	0.37	0.60	0.57	0.07	0.09
Venous PVS	0.15	0.16	0.24	0.22	0.05	0.06
ECS	0.22	0.23	0.37	0.36	0.04	0.07

Colour code	
Control group	iNPH group

Table 7.3: Average pressure gradient in each compartment at the end of infusion for both the control group (blue) and the iNPH group (beige). Gradients were computed using Equation (4.44) and the computed average speeds in Table 7.2.

Fluid transport between compartments

Figure 7.12a show the transfer between the extracellular space and and its connected compartments. Positive values indicate new inflow from the labelled compartment, while negative values show net outflow to the labelled compartment. The net flow rate from arterial PVS to ECS, and from ECS to venous PVS is at 0,15 ml/min at the end of infusion for both groups. The fluid transfer rates between ECS and PVS does not account for the majority of CSF flow in the PVS, as can be seen in Figure 7.12b. Most CSF enters the venous PVS from the capillary PVS and not through the ECS, and the fluid inflow from the capillary PVS to the venous PVS was 0.75 ml/min in both groups.

We observe a significantly higher fluid transfer rate in the ECS grey matter, compared to the white matter, shown in Figure 7.13a and Figure 7.13b. In both groups, the fluid transfer rate from the arterial PVS and to the venous PVS was at 0.15 ml/min at the end of infusion. More fluid enters than leaves the extracellular white matter. Fluid enters the ECS from the arterial PVS at a rate of 0.13 ml/min in the grey matter from the control group and 0.14 ml/min from the iNPH group, and at a rate of 0.01 ml/min in the white matter. Fluid leaves the ECS to the venous PVS at a rate of 0.14 ml/min in the grey matter and 0.01 ml/min in the white matter in both the control and iNPH group.

Similarly to the ECS grey and white matter transfer rate difference, most fluid transfer in the perivascular compartments happen in the grey matter. More than ten times the amount of fluid enters the venous PVS grey matter, seen in Figure 7.14a, than in the white matter, seen in Figure 7.14b. In both regions, most fluid enters the venous PVS from the capillary PVS. In the grey matter, this transfer happened at a rate of 0.69 ml/min for the control group and 0.71 for the iNPH group. The corresponding number for the white matter was 0.05 ml/min for both groups.

In Figure 7.15a, we see the total volume flow rate into the capillary compartment during the infusion. The fluid transfer rate remains stable in the vascular compartments. Throughout the simulation, the fluid transfer between arteries and capillaries, and the transfer between capillaries and veins, remaining at 640 ml/min in the control group and 565 ml/min in the iNPH group. As with the other compartments, most of the fluid transfer in the vascular compartments happen in the grey matter. In Figure 7.15b, we see that the grey matter transfer rate is 404 ml/min for the iNPH group and 434 ml/min in the control group, constituting over three quarters of the total transfer rate. Most fluid transfer graphs were not shown, but each fluid transfer $F_{i,j}$ from compartment i to compartment j at the end of infusion for every region of interest is shown in Table 7.4.

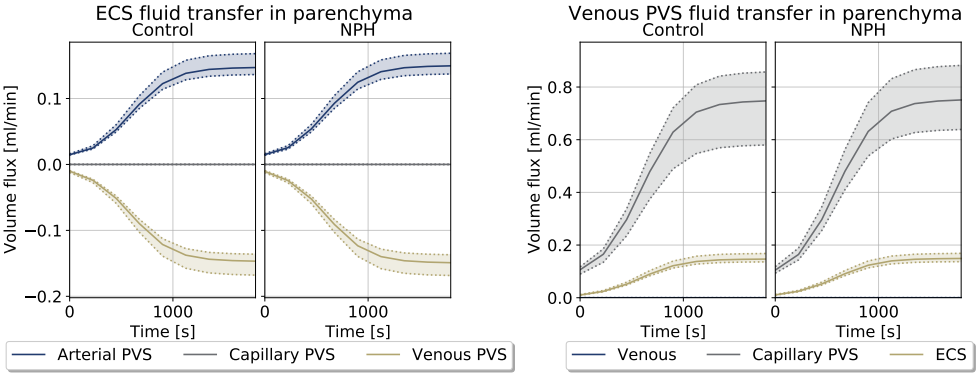

(a) (b)

Figure 7.12: The net fluid exchange between the ECS (figure a) and its connected compartments, and the fluid exchange between the venous PVS and its connections (figure b). In both figures, the whole line show the patient average within the group, and the dotted lines show the smallest and largest observed volume flux at the given time point.

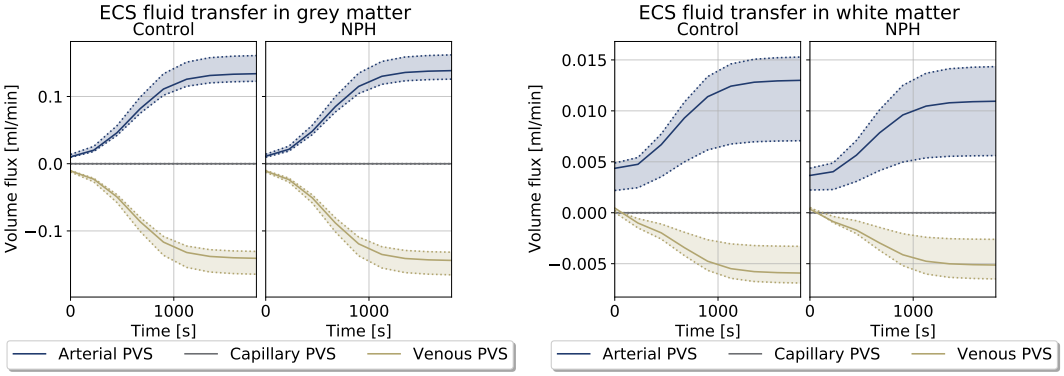

(a) (b)

Figure 7.13: The net fluid exchange between the ECS grey matter (figure a) and the ECS white matter (figure b) and their connected compartments. The legend show the colour of each compartment. In both figures, the whole line show the patient average within the group, and the dotted lines show the smallest and largest observed volume flux at the given time point.

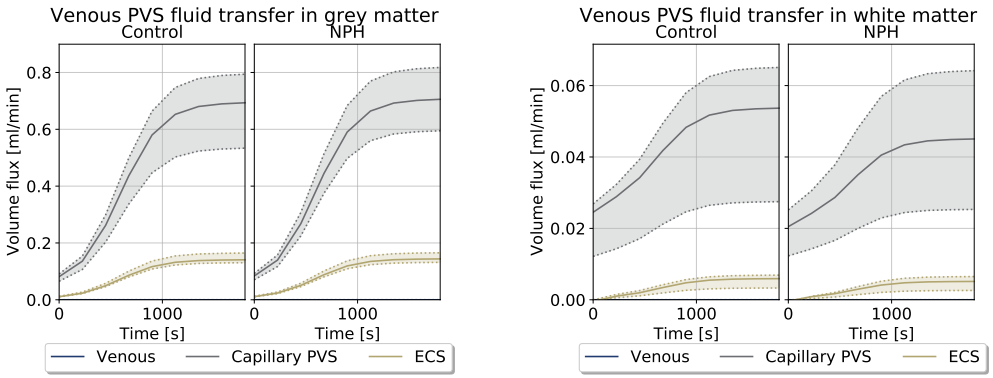

(a) (b)

Figure 7.14: The net fluid exchange between the venous PVS grey matter (figure a) and the venous PVS white matter (figure b) and their connected compartments. The legend show the colour of each compartment. In both figures, the whole line show the patient average within the group, and the dotted lines show the smallest and largest observed volume flux at the given time point.

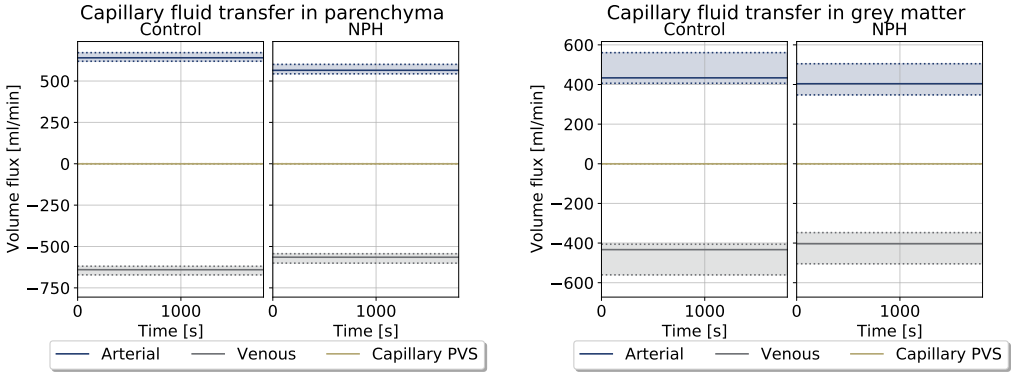

(a) (b)

Figure 7.15: The net fluid exchange between the capillary compartment in the entire brain parenchyma (figure a) and the capillary grey matter (figure b) and their connected compartments. The legend show the colour of each compartment. In both figures, the whole line show the patient average within the group, and the dotted lines show the smallest and largest observed volume flux at the given time point.

Total fluid transfer at the end of infusion [ml/min]

Compartment	Parenchyma		Grey Matter		White Matter	
$F_{a,c}$	640	565	434	404	205	159
$F_{c,v}$	640	565	433	404	205	160
$F_{c,pc}$	0.06	0.05	0.04	0.04	0.01	0.01
$F_{pa,pc}$	0.69	0.70	0.65	0.67	0.04	0.03
$F_{pa,e}$	0.15	0.15	0.13	0.14	0.01	0.01
$F_{pc,pv}$	0.75	0.75	0.69	0.71	0.05	0.05
$F_{e,pv}$	0.15	0.15	0.14	0.14	0.01	0.01

Colour code	
Control group	iNPH group

Table 7.4: Total fluid transfer $F_{i,j}$ from compartment i to compartment j for both the control group (blue) and the iNPH group (beige). Units are in ml/min.

7.2 Patient specific boundary conditions

In this section, we will present how our model estimates the response from the control group and the iNPH group to an infusion test. Using patient specific measurements of arterial inflow, outflow resistance and threshold pressure, we computed the pressure in each compartment over a time interval of half an hour. We also computed the system state at rest by simulating the system for five minutes before starting the infusion. The results will be presented in the same order as in the previous section, starting with the average pressures, then we present the average speeds before showing the total inter-compartmental fluid transfers in the end.

Average pressure

In Figure 7.16a we see the average pressure in the extracellular compartment over the entire parenchyma. The pressure starts at an initial plateau of 10.3 mmHg and 10.2 mmHg for the control and iNPH groups respectively. The interpersonal variance in both groups remain low before infusion starts, and both groups have similar ECS pressure levels. After infusion starts, the pressure rapidly increases in both groups. At the end of simulation, the group mean pressure in the control department reached a level of 22.9 mmHg, while the average patient in the iNPH group had a pressure of 32.0 mmHg in the ECS. The average pressure plateaus at different rates between different patients. In the iNPH curve, we see the pressure is still rising towards the end of infusion. This means not all iNPH patients had plateaued 30 minutes after infusion start. The CSF pressure in the perivascular compartments follow a very similar curve to the pressure in the ECS compartment, illustrated by the arterial PVS pressure in Figure 7.18a. At the end of infusion, the average patient in both groups has a arterial PVS pressure 0.1 mmHg higher than their corresponding ECS pressure. The pressure difference between the ECS and venous PVS is 0.1 mmHg and 0.15 mmHg in the control and iNPH groups respectively, with ECS pressure being the highest. The pressure spans in the iNPH group is large. At the end of infusion, the arterial PVS pressure ranges from 17.0 mmHg to 60.6 mmHg in the iNPH group, and from 13.7 mmHg to 39.3 mmHg in the control group.

Similarly to the average pressures in Section 7.1, the volume averaged pressure remains at comparable levels throughout the different regions. In Figure 7.17a and Figure 7.17b we see the ECS pressures for both the control and iNPH patients in the grey and white matter. The control group had an average pressure of 22.9 mmHg in the grey matter, and an average pressure of 23.0 mmHg in the white matter at the end of infusion. The iNPH group had a plateau pressure of 32.2 mmHg in the grey matter and 31.7 mmHg in the white matter. The perivascular pressure, like the extracellular pressure, has almost the same volume average in the grey and white matter. This can be seen in Figure 7.18a and Figure 7.18b, where we see the volume averaged pressure in the arterial PVS grey and white matter respectively. The initial pressure level in the arterial PVS white matter was 10.5 mmHg in the control and 10.4 mmHg for the iNPH group in both compartments. At the end of the simulation, both compartments ended at an average pressure of 23.0 mmHg in the control group and 31.7 mmHg in the NPH group. In the grey matter, the initial pressure was

Average compartmental pressure before the start of infusion [mmHg]

Compartment	Parenchyma		Grey Matter		White Matter	
Arterial	76.2	73.5	93.2	86.2	58.6	57.0
Capillary	22.3	21.7	24.6	23.4	20.0	19.5
Venous	11.1	10.9	10.3	10.3	11.9	11.7
Arterial PVS	10.3	10.3	10.1	10.1	10.5	10.4
Capillary PVS	10.3	10.3	10.1	10.1	10.5	10.4
Venous PVS	10.3	10.2	10.1	10.1	10.5	10.4
ECS	10.3	10.2	10.1	10.1	10.5	10.4

Colour code	
Control group	iNPH group

Table 7.5: Average pressure in each compartment before the start of infusion for both the control group (blue) and the iNPH group (beige). Patient specific boundary conditions were used. Units are in mmHg.

somewhat lower, at 10.1 mmHg in both groups, before rising to 23.1 mmHg and 32.5 mmHg in the control and iNPH groups respectively.

The arterial pressure is, however,higher in the grey matter than in the parenchyma as a whole. In the parenchyma, the average control patient has an arterial pressure of 76.2 mmHg before the onset of infusion, and the average iNPH patient has one of 73.5 mmHg. As can be seen in Figure 7.19a, the pressure rises after infusion starts, and reaches an average of 83.8 mmHg in the control group and 86.6 mmHg in the iNPH group. In Figure 7.19b, we can see the curves for arterial pressure in the grey matter. The arterial pressure rose from 93.2 mmHg to 101 mmHg in the control group, and from 86.2 mmHg to 99.3 mmHg in the iNPH group, in the grey matter. In the white matter, the arterial pressure starts at 58.6 mmHg and 57.0 mmHg in the control and iNPH group. After infusion this pressure ends at 66.1 mmHg and 70.1 mmHg for the control- and NPH patients respectively.

The pressure field in the ECS is characterised by a high pressure region at the pial boundary, with pressures reaching 25.3 mmHg in the control group and 34.7 mmHg in the iNPH group toward the end of the infusion test. This can be seen in Figure 7.20. Close to the pial boundary, the pressure drops by 1-2 mmHg, giving a significant pressure gradient in this region. There are some pressure gradients in the white matter, but the overall pressure differences are lower in both patients. A similar trend is seen in the venous and perivenous compartments as well. As can be seen in Figure 7.21 and Figure 7.22 the gradients are greatest at the pial surface. Unlike the ECS, pressure is lowest in the cortex, and is at its highest near the ventricular wall. The venous PVS pressure reaches 24.7 mmHg in the control group and 33.6 mmHg in the iNPH group. These numbers were 23.9 mmHg for controls and 26.7 mmHg for iNPH patients in the venous compartment.

We have not shown the pressure curves for each compartment, but we have listed the average pressure values in each compartment before infusion in Table 7.5, and at the end of simulation in Table 7.6

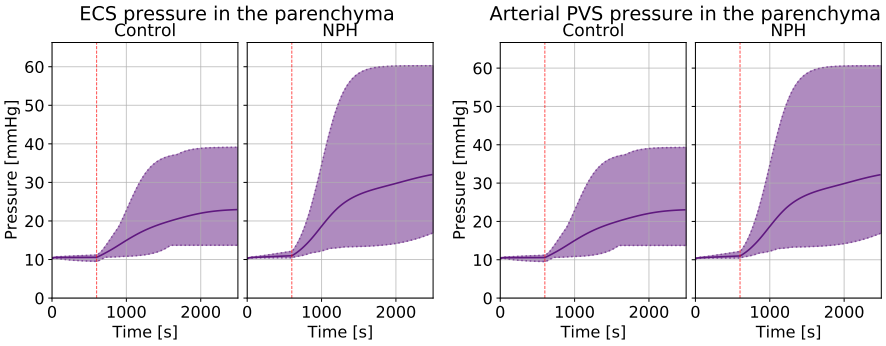

(a) (b)

Figure 7.16: The ECS and arterial PVS had similar pressure curves before and after infusion. In figure (a) we see the computed average extracellular pressure in the whole of the brain's extracellular space. . Figure (b) on the other hand show the volume averaged pressure in the arterial PVS. The whole line show the group average, while the dashed lines show the highest and lowest computed value at the given time point. The start of infusion is marked by the red dashed vertical line.

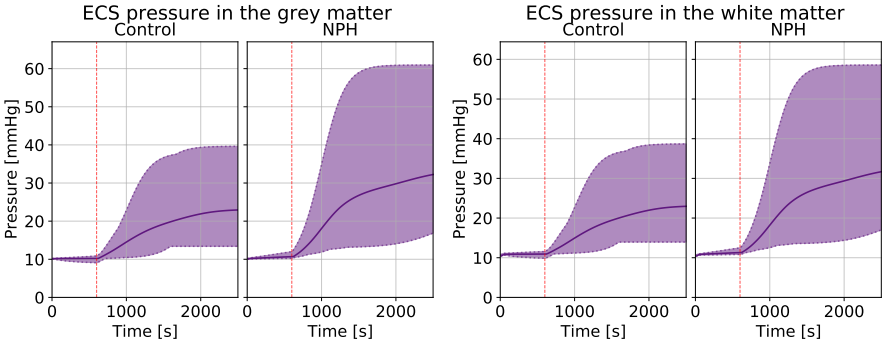

(a) (b)

Figure 7.17: Comparison between average ECS pressure in the grey and white matter under patient specific boundary conditions. In figure (a) we see the computed average extracellular pressure in the extracellular grey matter, while in figure (b) the average pressure in the ECS white matter is shown. The whole line show the group average, while the dashed lines show the highest and lowest computed value at the given time point. The start of infusion is marked by the red dashed vertical line.

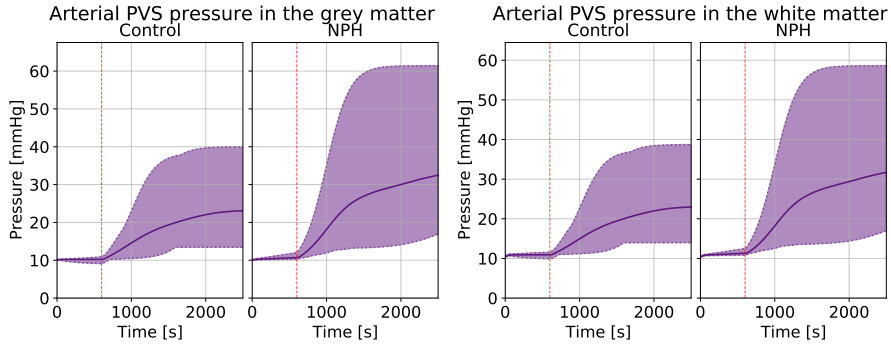

(a) (b)

Figure 7.18: Comparison between average arterial PVS pressure in the grey and white matter under patient specific boundary conditions. In figure (a) we see the computed average arterial PVS pressure in the extracellular grey matter, while in figure (b) the average pressure in the white matter is shown. The whole line show the group average, while the dashed lines show the highest and lowest computed value at the given time point. The start of infusion is marked by the red dashed vertical line.

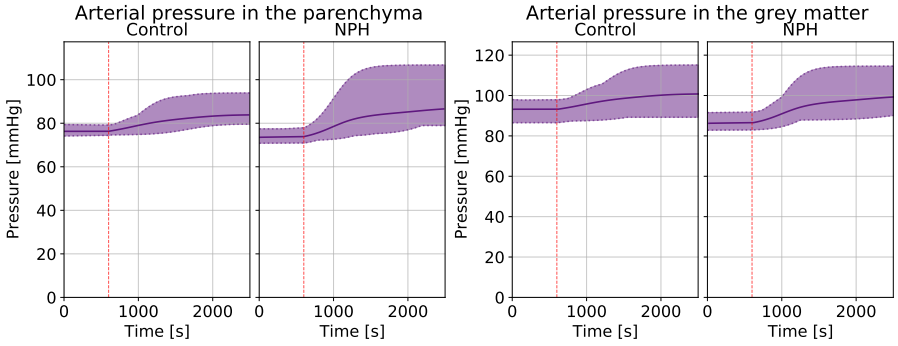

(a) (b)

Figure 7.19: Comparison between average arterial PVS pressure in the grey and white matter under patient specific boundary conditions. In figure (a) we see the computed average arterial PVS pressure in the extracellular grey matter, while in figure (b) the average pressure in the white matter is shown. The whole line show the group average, while the dashed lines show the highest and lowest computed value at the given time point. The start of infusion is marked by the red dashed vertical line.

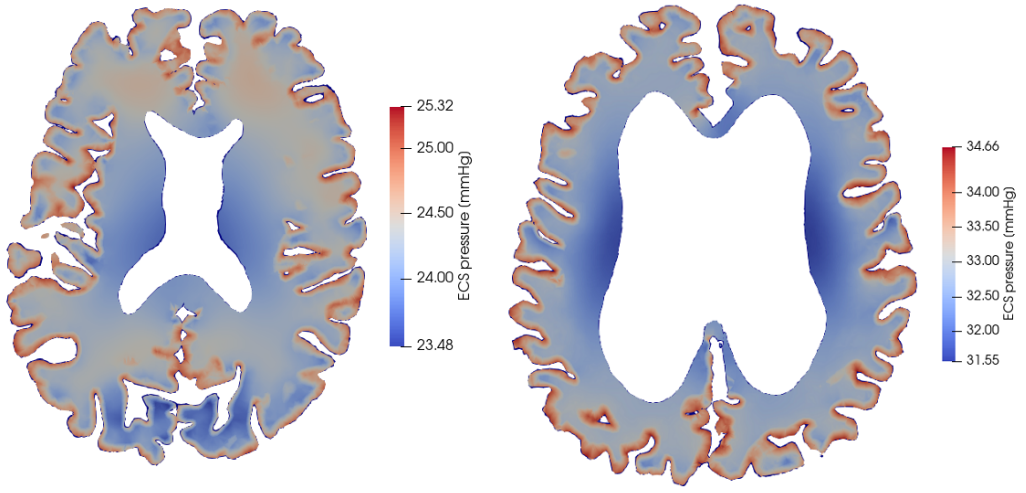

Figure 7.20: The figure show the pressure field in the extracellular space of patients C25 and NPH1 in a 2D slice of the brain parenchyma. Patient specific boundary conditions were used. The slice show the pressure at $t = 2000$ s, which is 1400 seconds after infusion start. In both patients, the pressure is highest at the cortex and lowest by the ventricle walls.

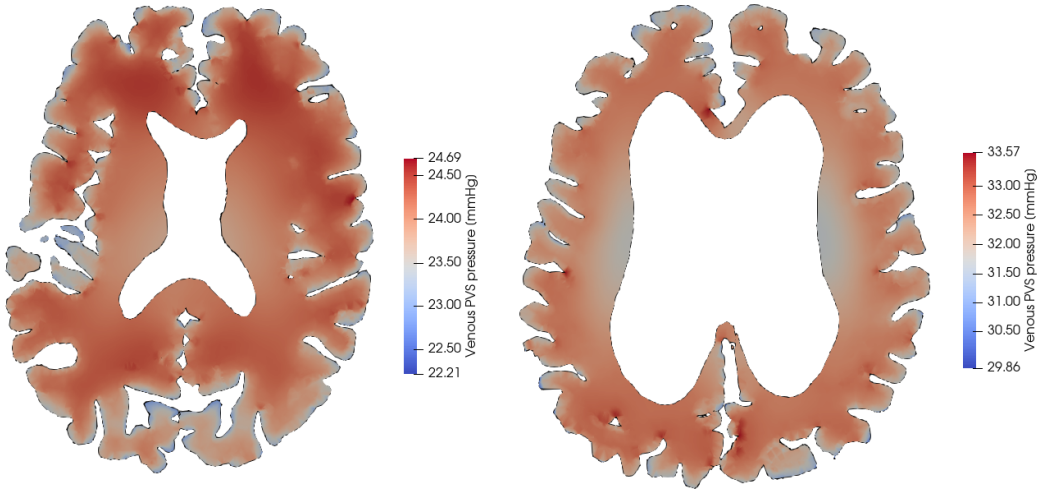

Figure 7.21: The figure show the pressure field in the venous PVS of patients C25 (left) and NPH1 (right) in a 2D slice of the brain parenchyma. Patient specific boundary conditions were used. The slice show the pressure at $t = 2000$ s, which is 1400 second after infusion start. In both patients, the pressure is highest in the white matter and lowest at the cortex.

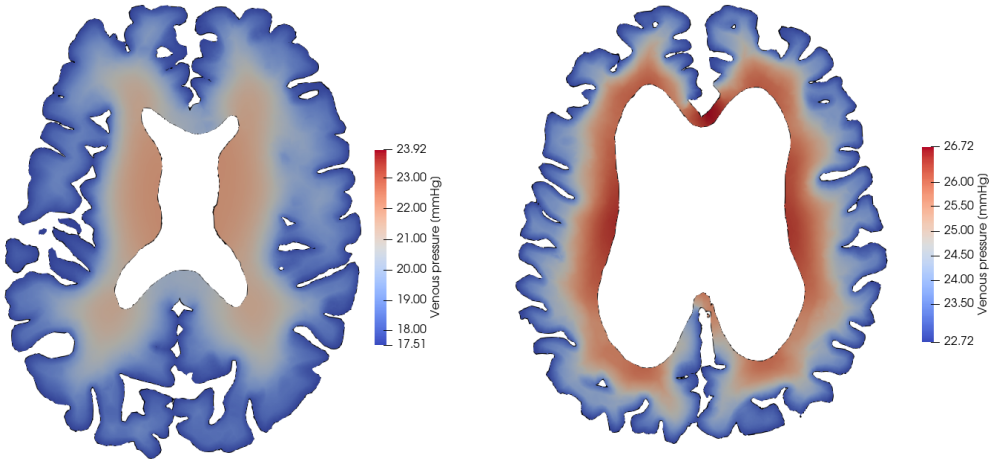

Figure 7.22: The figure show the pressure field in the venous compartment of patients C25 and NPH1 in a 2D slice of the brain parenchyma. The slice show the pressure at $t = 2000$ s, which is 1400 seconds after infusion start. In both patients, the pressure ranges is significantly higher in the white matter than at the cortex, signifying rapid outflow.

Average compartmental pressure at the end of infusion [mmHg]

Compartment	Parenchyma		Grey Matter		White Matter	
Arterial	83.8	86.6	101	99.2	66.1	70.1
Capillary	29.9	24.7	32.1	36.38	27.5	32.5
Venous	18.6	23.9	17.9	23.3	19.4	24.7
Arterial PVS	23.0	23.1	32.5	32.4	23.0	31.7
Capillary PVS	22.9	32.0	22.9	32.2	23.0	31.7
Venous PVS	22.8	31.8	22.8	32.0	23.0	31.7
ECS	22.9	32.0	22.9	32.2	23.0	31.7

Colour code	
Control group	iNPH group

Table 7.6: Average pressure in each compartment at the end of infusion for both the control group (blue) and the iNPH group (beige). Patient specific boundary conditions were used. Units are in mmHg.

Average velocities

There are significant speed differences between the control and iNPH groups in all compartments. In Figure 7.23a we see the average ISF velocity over the entire ECS. There is little movement in the brain ECS as a whole before infusion starts, with average speeds of 2.0 nm/s in the control group and 1.9 nm/s in the iNPH group. After infusion starts, the average speed remains stable for a time period of 5 minutes, before it rises steadily. The new speeds had not plateaued at simulation end, but the average control patient had a mean ISF speed of 6.84 nm/s and the average iNPH patient had a mean speed of 12.1 nm/s in the parenchyma. As in Section 7.1, velocities are higher in the perivascular compartments. We chose to again illustrate this with arterial PVS velocities. In Figure 7.23b we see the average arterial PVS velocity in the brain parenchyma. The iNPH group and the control group has comparable CSF flow speeds before start of infusion, with an average speed of 11.3 nm/s for both groups. After the onset of infusion, however, the NPH group experiences significantly higher fluid flow speeds. At $t = 2500$ s, the control group had an average arterial PVS speed of 134 nm/s, while the iNPH group had an average speed of 233 nm/s. In both the ECS and the PVS, inter-personal variance is large. The lowest computed arterial PVS speed was 37.1 nm/s, with the highest being 578 nm/s.

The average speed is higher in the ECS grey matter than the white matter. In Figure 7.24a we see the mean speed of the average control- and iNPH patient. The speeds are at the same level in the grey matter as in the parenchyma as a whole before infusion starts, at 2.59 nm/s and 2.37 nm/s in the control and iNPH group respectively. The response to the infusion is, however, strong. In the control group the average patient had a mean grey matter speed of 11.7 nm/s, and for the iNPH group it is 18.8 nm/s. In both regions and for both groups, the interpersonal variance is large. At the end of the infusion, average speeds in the grey matter varied from 3.35 nm/s to 30.9 nm/s in the control group, and 4.49 nm/s to 41.4 nm/s in the iNPH group. Fluid flow is slower in the white matter, as can be seen in Figure 7.24b. In the control group, the average patient would have an ISF flow speed of 2.3 nm/s as the infusion starts. After the infusion started, flow stagnated in the control group and ended up on 1.24 nm/s. Not all controls observed stagnating white matter ISF flow, with one patient plateauing at 3.71 nm/s. The NPH group showed higher white matter velocities, with the average patient having a white matter ISF speed of 1.86 nm/s at the end of infusion. The variance was also greater, with speeds ranging from 1.35 nm/s to 7.22 nm/s in the iNPH group compared to a span of 1.10 nm/s to 3.71 nm/s in the control group.

As with the ECS, the speeds are greater in the grey matter in the perivascular compartments. Figure 7.26a we see the speed curves for the arterial PVS in the grey matter. The average control patient has speeds of 234 nm/s in the grey matter at the end of infusion, and the average iNPH patient has speeds at 366 nm/s. Right before the start of infusion, these numbers were 15.4 nm/s for control and 14.6 nm/s for the iNPH group. In the white matter, the arterial PVS fluid speed increases from 7.0 nm/s and 7.1 nm/s to values are 23.9 nm/s and 42.4 nm/s in the control and iNPH groups respectively. This can be seen in Figure 7.26b. Similarly to the ECS, the average speeds has not plateaued for many patients, with the average speeds increasing toward the end of simulation.

The arterial compartment has, as in Section 7.1, constant blood speed

Average compartmental fluid speed before the start of infusion

Compartment	Unit	Parenchyma		Grey Matter		White Matter	
Arterial	mm/s	2.99	2.74	3.90	3.41	2.00	1.86
Capillary	μm/s	15.7	14.3	19.9	17.5	11.1	10.2
Venous	mm/s	1.32	1.22	1.77	1.52	0.83	0.80
Arterial PVS	nm/s	11.4	11.3	15.4	14.6	7.0	7.1
Capillary PVS	nm/s	1.6	1.6	2.2	2.0	1.0	1.0
Venous PVS	nm/s	96.3	94.0	135	124	53.7	54.0
ECS	nm/s	2.0	1.9	2.6	2.4	1.4	1.4

Colour code	
Control group	iNPH group

Table 7.7: Average speed in each compartment before the start of infusion for both the control group (blue) and the iNPH group (beige). Fluid flow happen on several different orders of magnitude, and hence the units are shown in a separate column. Patient specific boundary conditions were used.

throughout the infusion. The same is seen in all vascular compartments. The average control patient has an arterial blood speed of 2.99 mm/s in the parenchyma as a whole, and 3.90 mm/s in the grey matter. The average iNPH patient had lower arterial blood speeds, at 2.74 mm/s in the parenchyma as a whole and 3.41 mm/s in the grey matter.

Not all speed curves have been shown, but the average speed before infusion is shown in Table 7.7, and the mean speed after infusion is shown in Table 7.8. Furthermore, using Equation (4.44), we computed the corresponding average pressure gradients, which are shown in Table 7.9 and Table 7.10.

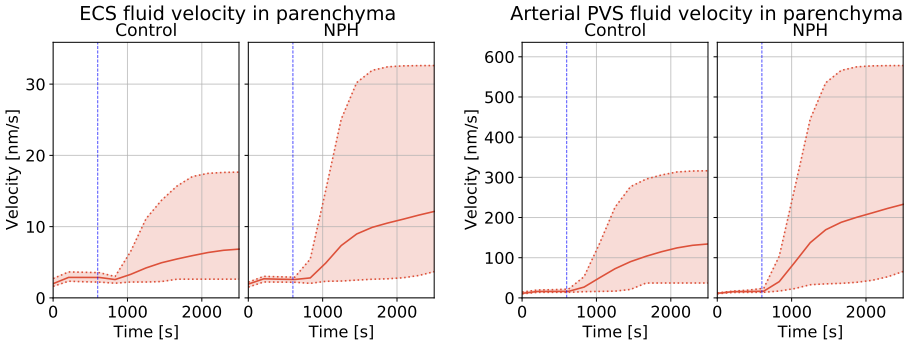

(a) (b)

Figure 7.23: Fluid in the ECS moved significantly slower than in the arterial PVS. In figure (a) we see the computed average extracellular fluid speed in the whole of the brain's extracellular space. Figure (b) on the other hand show the volume averaged pore speed in the arterial PVS. The whole line show the group average, while the dashed lines show the highest and lowest computed value at the given time point. The vertical dashed blue line show the start of infusion at $t = 600$ s.

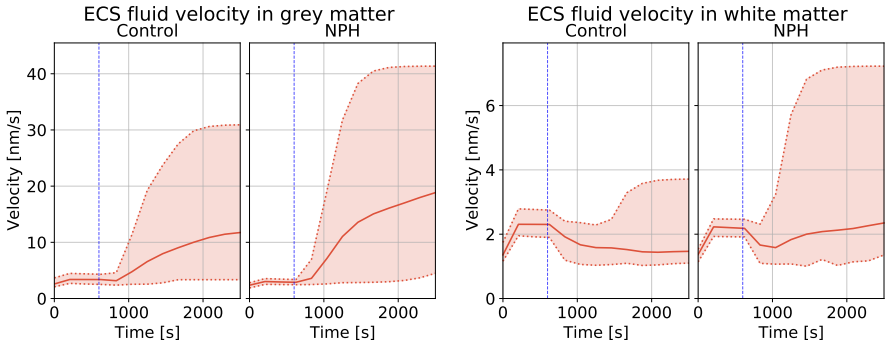

(a) (b)

Figure 7.24: Fluid in the ECS moved quicker in the grey than in the white matter. In figure (a) we see the computed average extracellular fluid speed in the grey matter, while figure (b) on the other hand show the speed in the white matter. The simulation ended at $t = 2500$ s. The whole line show the group average, while the dashed lines show the highest and lowest computed value at the given time point. The vertical dashed blue line show the start of infusion at $t = 600$ s.

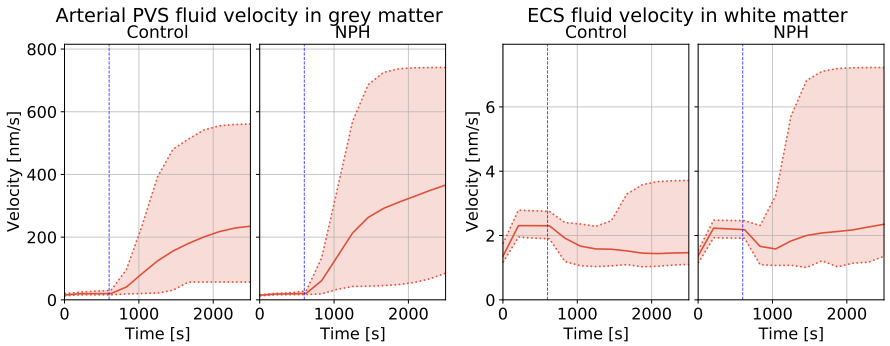

(a) (b)

Figure 7.25: Fluid in the ECS moved quicker in the grey than in the white matter. In figure (a) we see the computed average extracellular fluid speed in the grey matter, while figure (b) on the other hand show the speed in the white matter. The simulation ended at $t = 2500$ s. The whole line show the group average, while the dashed lines show the highest and lowest computed value at the given time point. The vertical dashed blue line show the start of infusion at $t = 600$ s.

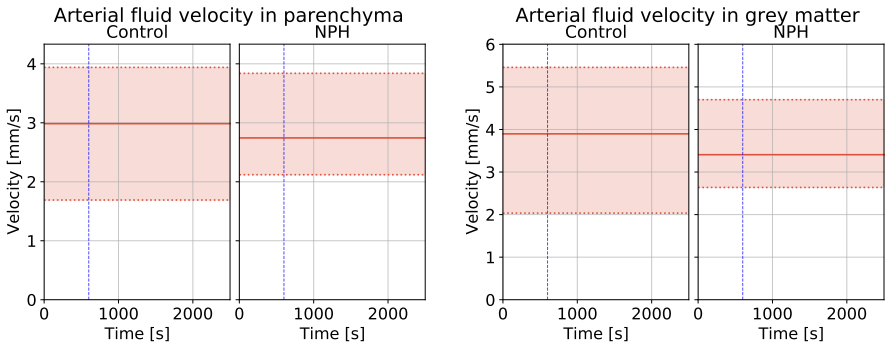

(a) (b)

Figure 7.26: Fluid in the ECS moved quicker in the grey than in the white matter. In figure (a) we see the computed average extracellular fluid speed in the grey matter, while figure (b) on the other hand show the speed in the white matter. The simulation ended at $t = 2500$ s. The whole line show the group average, while the dashed lines show the highest and lowest computed value at the given time point. The vertical dashed blue line show the start of infusion at $t = 600$ s.

Average compartmental fluid speed at the end of infusion

Compartment	Unit	Parenchyma		Grey Matter		White Matter	
Arterial	mm/s	2.99	2.74	3.90	3.41	2.00	1.86
Capillary	μm/s	15.7	14.3	19.9	17.5	11.1	10.2
Venous	mm/s	1.32	1.22	1.77	1.52	0.83	0.80
Arterial PVS	nm/s	134	233	235	366	23.9	42.4
Capillary PVS	nm/s	8.8	15.5	15.1	24.0	1.9	3.3
Venous PVS	nm/s	182	264	292	390	60.3	82.2
ECS	nm/s	6.8	12.1	11.7	18.8	1.5	2.3

Colour code	
Control group	iNPH group

Table 7.8: Average speed in each compartment at the end of infusion for both the control group (blue) and the iNPH group (beige). Fluid flow happen on several different orders of magnitude, and hence the units are shown in a separate column. Patient specific boundary conditions were used.

Average compartmental pressure gradient before infusion [mmHg/mm]

Compartment	Parenchyma		Grey Matter		White Matter	
Arterial	4.41	4.05	5.76	5.05	2.95	2.75
Capillary	0.53	0.49	0.68	0.59	0.38	0.35
Venous	0.29	0.27	0.39	0.34	0.18	0.18
Arterial PVS	0.08	0.08	0.10	0.10	0.05	0.05
Capillary PVS	0.07	0.07	0.10	0.09	0.05	0.05
Venous PVS	0.09	0.08	0.12	0.11	0.05	0.05
ECS	0.07	0.07	0.09	0.08	0.05	0.05

Colour code	
Control group	iNPH group

Table 7.9: Average pressure gradient in each compartment at before infusion for both the control group (blue) and the iNPH group (beige). Gradients were computed using Equation (4.44) and the computed average speeds in Table 7.7. Patient specific boundary conditions were applied.

Average compartmental pressure gradient at the end of infusion [mmHg/mm]

Compartment	Parenchyma		Grey Matter		White Matter	
Arterial	4.41	4.05	5.76	5.05	2.95	2.75
Capillary	0.53	0.49	0.68	0.59	0.38	0.35
Venous	0.29	0.27	0.39	0.34	0.18	0.18
Arterial PVS	0.90	1.57	1.58	2.46	0.16	0.29
Capillary PVS	0.41	0.71	0.70	1.11	0.09	0.15
Venous PVS	0.16	0.24	0.26	0.35	0.05	0.07
ECS	0.23	0.42	0.40	0.65	0.05	0.08

Colour code	
Control group	iNPH group

Table 7.10: Average pressure gradient in each compartment at the end of infusion for both the control group (blue) and the iNPH group (beige). Gradients were computed using Equation (4.44) and the computed average speeds in Table 7.8. Patient specific boundary conditions were applied.

Fluid transfer rates with patient specific CSF pressure

With patient specific boundary conditions, inter-compartmental transfer increased in both groups. Figure 7.27a shows the fluid transfer rate to and from the entire ECS and its connected compartments in ml/min. The transfer rate stays stable at a net inflow of $1.19 \cdot 10^{-2}$ ml/min from the arterial PVS and a net outflow of $1.17 \cdot 10^{-2}$ ml/min to the venous PVS for the control group. The numbers for the iNPH group was $1.40 \cdot 10^{-2}$ ml/min from arterial PVS and $1.38 \cdot 10^{-2}$ ml/min to venous PVS. Fluid exchange with capillary PVS was negligible. After infusion started, the transfers increased. The control group received $1.55 \cdot 10^{-1}$ ml/min from arterial PVS and sent $1.54 \cdot 10^{-1}$ ml/min to the venous PVS. The ECS of the iNPH group had a net inflow of $2.60 \cdot 10^{-1}$ ml/min from arterial PVS and a net outflow of $2.59 \cdot 10^{-1}$ ml/min to the venous PVS at the end of infusion. In comparison, Figure 7.27b show the rates at which fluid entered and left the venous PVS for both the control and the iNPH group during simulation. The net fluid inflow from the ECS is the same as shown in figure (a). The inflow from capillary PVS was larger at all points of the simulation, starting at $1.05 \cdot 10^{-1}$ ml/min in the control and $1.12 \cdot 10^{-1}$ ml/min in the iNPH group. At the end of simulation this had increased to $7.77 \cdot 10^{-1}$ ml/min for controls and 1.26 ml/min for iNPH patients. Only a small part of the CSF in- and outflow goes through the ECS. The inflow from capillary PVS to venous PVS is 8.92 times as large before infusion starts. At the end of simulation, flow from capillary PVS to venous PVS was 5.03 times as large as flow from ECS to venous PVS.

The fluid exchange rates from different subdomains show most fluid exchange happen in the grey matter. This is illustrated in Figure 7.28a which show the fluid transfer rate to and from the grey matter ECS and its connected compartments in ml/min, and Figure 7.28b which show the transfer rates for the white matter ECS. The transfer rate stays stable in both regions before infusion starts, with a net inflow of $8.04 \cdot 10^{-3}$ ml/min from the arterial PVS and a net outflow of $1.11 \cdot 10^{-2}$ ml/min to the venous PVS for the control group. The numbers for the iNPH group was $1.07 \cdot 10^{-2}$ ml/min from arterial PVS and $1.32 \cdot 10^{-2}$ ml/min to venous PVS. Fluid exchange with capillary PVS was negligible. As the infusion test started the transfers increased. The control group recieved $1.41 \cdot 10^{-1}$ ml/min from arterial PVS and sent $1.48 \cdot 10^{-1}$ ml/min to the venous PVS in the grey matter at the end of simulation. The ECS grey matter of the iNPH group had a net inflow of $2.43 \cdot 10^{-1}$ ml/min from arterial PVS and a net outflow of $2.51 \cdot 10^{-1}$ ml/min to the venous PVS at the end of infusion. The transfer in the ECS white matter was significantly lower throughout the entire simulation. Before the infusion started, the ECS white matter had a on average net inflow from the arterial PVS of $3.82 \cdot 10^{-3}$ ml/min in the control group and $3.31 \cdot 10^{-3}$ ml/min in the NPH group. At the same time, the net outflow from the extracellular white matter to the venous PVS white matter was $6.64 \cdot 10^{-4}$ ml/min in the control group and $6.64 \cdot 10^{-4}$ ml/min. At the end of simulation, the inflow from the arterial PVS had increased to $1.36 \cdot 10^{-2}$ ml/min in the control group and $1.63 \cdot 10^{-2}$ ml/min in the iNPH group. The net outflow to venous PVS in the white matter at this time point was $6.29 \cdot 10^{-3}$ ml/min for controls and $8.42 \cdot 10^{-3}$ ml/min for iNPH patients. The net inflow into the ECS white matter indicate a net fluid flow from the ECS white matter to the ECS grey matter before the fluid flows into the venous

PVS.

As with the ECS, the fluid transfers are also larger in the grey matter for the perivascular compartments. We have illustrated this with the venous PVS, and in Figure 7.29a and Figure 7.29b we see the fluid transfers to the venous PVS in the grey and white matter respectively. Before infusion, the inflow into the grey matter was $7.80 \cdot 10^{-2}$ ml/min from capillary PVS and $1.11 \cdot 10^{-2}$ ml/min from the ECS in the control group. In the NPH group, the inflow pre-infusion was $8.92 \cdot 10^{-2}$ ml/min from the capillary PVS and $1.32 \cdot 10^{-2}$ ml/min in the ECS. At the final time point, the inflow rates in the control was $7.21 \cdot 10^{-1}$ ml/min from the capillary PVS and $1.48 \cdot 10^{-1}$ ml/min from the ECS. In the NPH group, fluid entered the venous PVS at a rate of 1.20 ml/min from the capillary PVS and $2.51 \cdot 10^{-1}$ ml/min from the ECS. The white matter fluid flow rate is lower from both compartments. The transfer from the ECS is less than 1 μl/min before infusion, and at the end of the simulation it had risen to only 6.29 μl/min and 8.43 μl/min from the control and iNPH groups respectively. CSF enters the venous PVS from the capillary PVS at a rate of 2.65 ml/min in the controls and $2.24 \cdot 10^{-2}$ ml/min in the NPH group at the start of infusion. At the end, the rates had risen to $5.51 \cdot 10^{-2}$ ml/min and $6.05 \cdot 10^{-2}$ ml/min in the control and iNPH groups respectively. The relative difference between the inflows from the PVS and ECS is lower in the grey matter. Both before and after infusion, the inflow into the venous PVS white matter from the capillary PVS was more than 10 times as large as the one from the ECS. In the grey matter, the capillary PVS inflow was seven times larger than the ECS inflow before infusion in both groups. At the end, the rate had fallen to 5.1 in the control group and 4.8 in the iNPH group.

The transfer rates in the vascular compartments remain stable throughout the simulation. In figures Figure 7.30a and Figure 7.30b we see the transfer rate to and from the capillaries in the grey and white matter respectively. In both regions, and for both groups, the volume in- and outflow only increase by less than 1 ‰ after infusion starts. Little fluid is exchanged with the perivascular spaces, and fluid enters and leaves the capillaries in the grey matter at a rate of 433 ml/min in the controls and 403 ml/min in the iNPH group. Fluid enters the capillaries from the arteries and leaves into the veins. In the white matter, the flow rates are lower, with inflow at 206 ml/min in the control group and 160 ml/min in NPH. Outflow was the same in both groups.

The fluid transfer graphs is not shown for all compartments and all subdomains. We have listed all transfers with a nonzero transfer rate in Table 7.11 and Table 7.12. The former table show the fluid transfers before the start of infusion, the latter the transfers at the end of simulation.

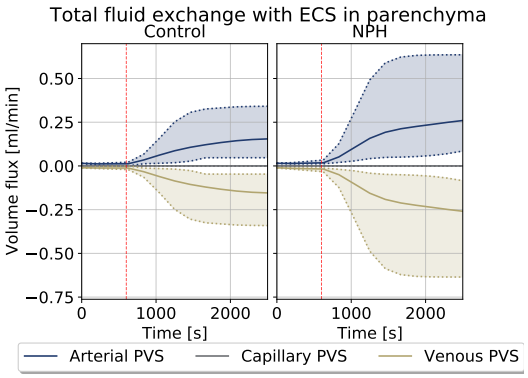

(a)

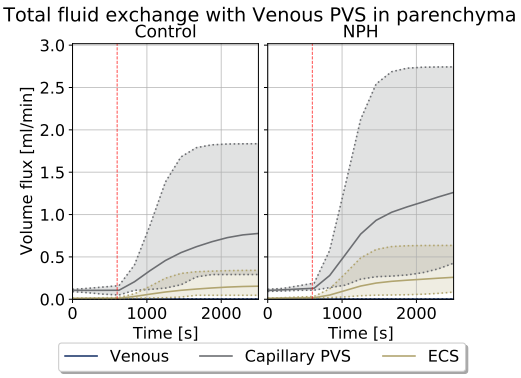

(b)

Figure 7.27: These figures show the net fluid exchange between the ECS (figure a) and its connected compartments, and the fluid exchange betwen the venous PVS and its connections (figure b). In figure (a), we observe the inflow from the arterial PVS and the outflow to the venous PVS is almost balanced out. Fluid exchange between the ECS and capillary PVS is negligible. Figure (b) show that only a small part of the CSF in- and outflow goes through the ECS. In both figures, the whole line show the patient average within the group, and the dotted lines show the smallest and largest observed volume flux at the given time point. The red dashed line marks the start of infusion.

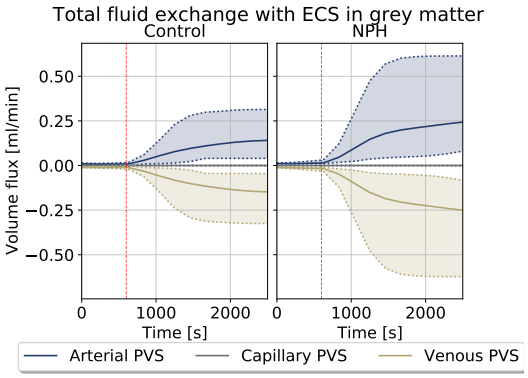

(a)

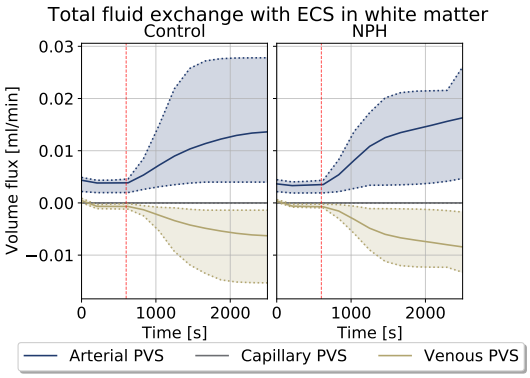

(b)

Figure 7.28: The fluid exchange between the ECS grey- (a) and white matter (b) and the connected compartments to the ECS, In both regions, the fluid transfer remains stable before the start of infusion. As infusion starts, which is marked by the red dashed line, the inter-compartmental transfer rapidly increases. In both the grey and white matter, the transfer rate increases by more than one order of magnitude. In the white matter, there is a net inflow in both control and iNPH groups. The whole line show the patient average within the group, and the dotted lines show the smallest and largest observed volume flux at the given time point. The fluid exchange with the capillary PVS is negligible.

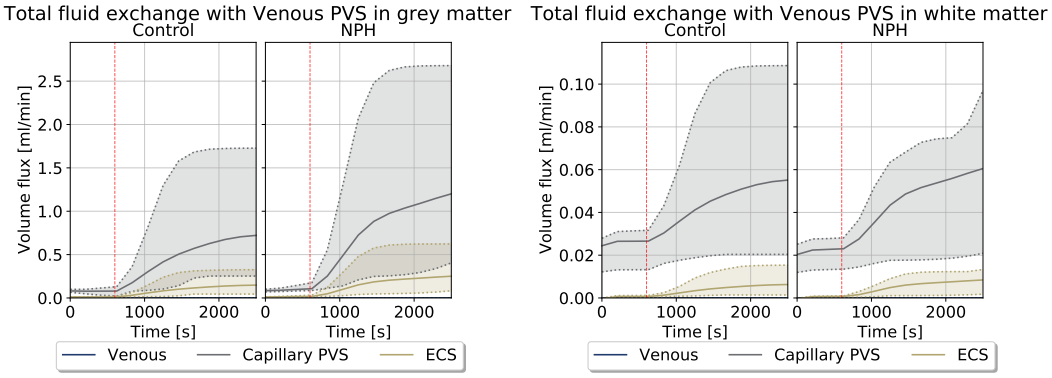

(a) (b)

Figure 7.29: The fluid exchange between the venous PVS grey- (a) and white matter (b) and the compartments connected to it. In both regions, the fluid transfer remains stable before the start of infusion. As infusion starts, which is marked by the red dashed line, the inter-compartmental transfer rapidly increases. In both the grey and white matter, the transfer rate is increased tenfold. The relative difference between inflow from capillary PVS and inflow from the ECS is larger in the white matter than in the grey matter. Fluid inflow is larger in the grey matter from both the ECS and the venous PVS. The whole line show the patient average within the group, and the dotted lines show the smallest and largest observed volume flux at the given time point. The fluid exchange with the capillary PVS is negligible.

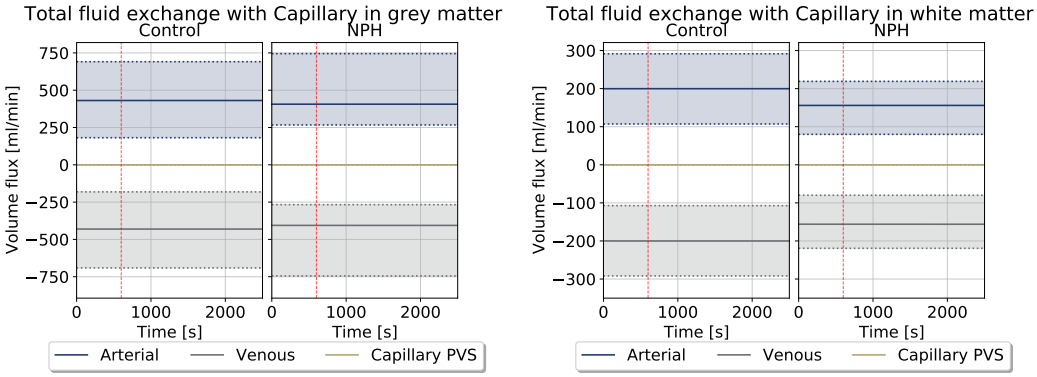

(a) (b)

Figure 7.30: The fluid exchange between the capillaries in the grey- (a) and white matter (b) and the compartments connected to it. In both regions, the fluid transfer remains stable throughout the simulation. The transfer remains negligible. Total change between infusion start and end was less than 1 ‰ of the total fluid transfer in both group and between all compartments in both figures. The whole line show the patient average within the group, and the dotted lines show the smallest and largest observed volume flux at the given time point. The fluid exchange with the capillary PVS is negligible.

Total fluid transfer before infusion [ml/min]

Compartment	Parenchyma		Grey Matter		White Matter	
$F_{a,c}$	633	564	431	406	200	156
$F_{c,v}$	633	564	431	406	200	156
$F_{c,pc}$	0.09	0.09	0.06	0.06	0.03	0.01
$F_{pa,pc}$	0.01	0.03	0.02	0.04	-0.01	0.00
$F_{pa,e}$	0.01	0.02	0.01	0.01	0.00	0.00
$F_{pc,pv}$	0.10	0.12	0.08	0.10	0.03	0.02
$F_{e,pv}$	0.01	0.02	0.01	0.02	0.00	0.00

Colour code	
Control group	iNPH group

Table 7.11: Total fluid transfer $F_{i,j}$ from compartment i to compartment j before the start of infusion. The control group is marked in blue and the iNPH group in beige. Units are in ml/min. Patient specific boundary conditions were used.

Total fluid transfer at the end of infusion [ml/min]

Compartment	Parenchyma		Grey Matter		White Matter	
$F_{a,c}$	633	564	431	406	200	156
$F_{c,v}$	633	564	431	406	200	156
$F_{c,pc}$	0.06	0.02	0.04	0.02	0.02	0.00
$F_{pa,pc}$	0.72	1.24	0.68	1.18	0.04	0.06
$F_{pa,e}$	0.15	0.26	0.14	0.24	0.01	0.02
$F_{pc,pv}$	0.77	1.26	0.72	1.20	0.06	0.06
$F_{e,pv}$	0.15	0.26	0.15	0.25	0.01	0.01

Colour code	
Control group	iNPH group

Table 7.12: Total fluid transfer $F_{i,j}$ from compartment i to compartment j at the end of infusion. The control group is marked in blue and the iNPH group in beige. Units are in ml/min. Patient specific boundary conditions were used.

CHAPTER 8

Discussion

This chapter is dedicated to discussion and interpretation of our results as well as their limitations and place in an academic context. The first section is a short summary of our results. Afterwards we will discuss their plausibility and how they compare to experimental and clinical data. Thereafter we will consider the limitations of our work and possible extensions and corrections to our work. Lastly, we will summarise our discussion and what our simulations imply.

8.1 Summary of results

After extensive testing, we concluded that the a mesh resolution of RP32 was sufficient if we used CG2 polynomials. Furthermore, a time step of 20 was deemed necessary to ensure a sufficient resolution in time.

When subjected to the same CSF pressure, little to no difference between patients was found. The total variance in average ECS pressure in the control group was much smaller than 1 mmHg throughout the simulation. The same was observed within the iNPH group. Furthermore, the pressure difference between the groups was also small. The average pressure was 0.1 mmHg higher in the iNPH group than in the control group at the end of infusion. Speeds were ten times as high in the grey as the white matter for both the ECS and all perivascular compartments. The vascular speeds were higher in the grey matter, but the increase from the white matter was smaller than in the PVS/ECS. Velocities in the ECS were computed to be in the range of 6-7 nm/s at the end of infusion for most patients. The iNPH group had on average 0.5 nm/s higher speed than that of the control group. Fluid transfer rates between compartments were almost identical within and between groups when subjected to the same boundary condition. A slight difference was observed in the ECS white matter, where the control group had slightly higher clearance rate than the NPH group. Yet, almost all fluid transfer happened in the grey matter, making this difference negligible.

When using patient specific CSF pressure at the boundary, the situation changes. The stronger response to an infusion test in the ICP for the iNPH group propagated into the brain parenchyma. The response of the arterial, capillary and venous compartments were all mostly dependent on arterial inflow. This is on average lower in the iNPH group. At the start of infusion, capillary filtration is an important part of CSF inflow to the PVS. The filtration rate is lowered after the start of infusion. Towards the end of infusion, the inflow from

and outflow to the SAS is the dominating factor in the PVS. By extension, the same holds for the ECS.

In our computation with patient specific CSF pressure, we computed the state of each patient at rest. The ISF pressure was 10.1 mmHg in both groups before infusion started. The difference in group response became clear shortly after the infusion test began. While the control group seemed to settle at an average pressure of 23 mmHg, a 0.7 mmHg increase from Section 7.1, the changes in the iNPH group was significantly greater. The average iNPH patient had a mean ECS pressure of 22.2 mmHg when subjected to the non-patient specific boundary condition. With patient specific boundary conditions, the mean pressure for the average patient had not fully plateaued after half an hour of infusion. The ECS pressure reached a level of 32.0 mmHg for the average iNPH patient, with one patient plateauing at 60 mmHg.

The fluid speeds were increased in the PVS and ECS compared to what we got when using the same CSF pressure for all patients. The control group had slightly higher average speeds in the PVS and ECS, and, as with average pressure, the speed increase was higher in the iNPH group. While the CSF flow speeds before infusion were almost identical with the control group, after infusion the speed in arterial and venous PVS was over 100 nm/s greater in the average iNPH patient. Inter-compartmental transfer followed the same pattern as pressure and speed, with similar transfer rates before infusion and a stronger response to infusion in the iNPH group.

The interpersonal variance is higher when using patient specific boundary conditions. In Section 7.1, there was little variance in pressure, speed and transfer rates in all compartments. The same can, however, not be said for Section 7.2. In the PVS, the highest computed speed was more than 8 times as large as the lowest, and the total fluid transfer between the arterial PVS and the ECS ranged from under 0.1 ml/min to over 0.6 ml/min.

8.2 Our results in context

In this section, we will discuss our results in detail and how they measure up to the work of others. We will compare with both experimental and computational studies. We begin by discussing how our results concerning the system at rest compare to the literature. The second section is dedicated to discussing our results concerning the waterscape of the brain during infusion tests.

The brain state pre-infusion

The glymphatic hypothesis relies on convective flow of CSF in the PVS (Abbott et al. (2018)). Initially, it also relied on convective flow of ISF in the ECS (Iliff, M. Wang, Liao et al. (2012)). As a result, a significant effort by the scientific community has been made to investigate flow in these compartments.

Two such studies are the simulation studies of Holter et al. (2017) and Jin, Smith and Verkman (2016), who both found ISF bulk flow unlikely. The simulations of Holter et al. (2017) concluded that, even with a steep pressure gradient of 1 mmHg/mm, ISF speeds in the ECS were observed in the range of 1-10 nm/s. With our model, we get similar results. Before infusion started, we computed an average speed of 2-3 nm/s in all patients in both grey and white

matter. Jin, Smith and Verkman (2016) found that sustained unphysically large pressure gradients between the arterial and venous PVS were necessary to facilitate bulk flow in the brain ECS. In Section 7.2, we computed the average PVS pressure before infusion. Just as Jin, Smith and Verkman (2016), we do not observe the necessary conditions for bulk flow in the ECS. It is important to note that both Jin, Smith and Verkman (2016) and Holter et al. (2017) only considered the effects on a small subdomain of the ECS. Furthermore, the domain of Jin, Smith and Verkman (2016) was an idealised 2D-construction, while our domains are generated from MRI images of patients. Hence, our simulations are on a different length scale than the work of Holter et al. (2017) and Jin, Smith and Verkman (2016).

Not all studies find convective ECS flow unlikely. Ray, Iliff and Heys (2019) reported superficial bulk flow velocities of 7 to 50 μm/min, corresponding to pore velocities of 35 to 150 μm/min, or 0.58 to 2.50 μm/s. This is significantly higher than our computed ISF speeds of 2-3 nm/s in the ECS. This difference is due to the fact that Ray, Iliff and Heys (2019) assume much higher pressure gradients and permeabilities than we did in our simulations. For instance, their permeability is between one and two orders of magnitude greater than that of Holter et al. (2017). In addition, a pressure difference of at least 0.8 mmHg between venous and arterial PVS is assumed. The mesh used by Ray, Iliff and Heys (2019) set a distance of $d = 250\mu$m of between venous and arterial PVS. Their assumed pressure difference of 0.8 mmHg then result in a pressure gradient of 3.2 mmHg/mm between the arterial and venous PVS. Dutta-Roy, Wittek and Miller (2008) found that a CSF pressure difference of 1.76 mmHg between the lateral ventricles and SAS was sufficient to induce ventriculomegaly. Furthermore, Holter et al. (2017) worked with an upper bound on the extracellular pressure gradient at 1 mmHg/mm. Our computed pressure gradient before infusion is, on average, significantly lower than that. In the ECS, the highest average pressure gradient before infusion was in the extracellular grey matter at 0.09 mmHg/mm . This is lower than the gradient enforced by Ray, Iliff and Heys (2019) or computed by Tithof et al. (2022). The pressure gradient of 0.09 mmHg/mm is, however, a volume average and not an upper bound on the pressure gradients within the parenchyma. The experimental study of P. K. Eide and Sæhle (2010) observed a maximal pressure difference between ventricular and subarachnoid CSF during the cardiac cycle of 0.18 mmHg. The pressure gradient of Ray, Iliff and Heys (2019) is significantly higher than the upper bound assumed by Holter et al. (2017), and measured by P. K. Eide and Sæhle (2010). When using the extracellular permeability computed by Holter et al. (2017), and a pressure gradient of 0.8 mmHg/mm, the authors report a speed of 4.2 nm/s. This is more in agreement with our computed extracellular pore speed of 2.0 nm/s.

Flow in the perivascular spaces has been a popular topic in the recent years. Tithof et al. (2022) estimated the pressure gradients required for convective perivascular flow in mice. They find that velocities were larger in the grey matter, but that CSF flow continued into the white matter. The authors report that the CSF flow speed within the parenchyma were in the range of 19 nm/s to 60 nm/s. Our computed speeds are lower than that of Tithof et al. (2022), with arterial PVS speeds of 16.1 nm/s and 16.9 nm/s in the grey matter for iNPH and control patients respectively. In the white matter, we found an average speed of 7.71 nm/s and 7.79 nm/s. Both the grey- and white matter

flow rates are below the computed range of Tithof et al. (2022). An explanation for why our results differ from that of Tithof et al. (2022) is, of course, that our model considers the human brain and not that of mice. That being said, there is also a more mathematical explanation. From Equation (4.38), we know that the two coefficients determining fluid velocity in a compartment is the porosity and permeability. Tithof et al. (2022) concludes that a scenario where the hydraulic resistance in the ECS is of a similar magnitude to that in the PVS, gives results which most closely resembles in-vivo measurements in mice. The authors remarks that their permeabilities are similar to that of Vinje et al. (2020). As we used the permeabilities computed by Vinje et al. (2020) in our model, we are in agreement with Tithof et al. (2022) about the permeability of the perivascular spaces. On the other hand, Tithof et al. (2022) based their estimation on the possible range of the porosity ϕ_i of the PVS on the sizes of the basement membrane and the endothelial glycocalyx. These structures gave a lower $\phi_{PVS} = 0.07\phi_{vascular}$, and upper $\phi_{PVS} = 0.36\phi_{vascular}$ bound for the porosity. In our simulations, we estimated the porosity of the PVS based on in-vivo images in mice taken by Pizzo et al. (2018). These images suggested a capillary PVS with a cross sectional area equal to the capillaries themselves. Hence, assuming the PVS to not increase in volume relative to the PVS, the porosity of arterial and venous PVS was set to $\phi_{PVS} = 1.4\phi_{vascular}$ based on the estimates by Mestre et al. (2018).

The expected pressure drop in the PVS was investigated by Tithof et al. (2022), who simulated four different scenarios for flow in the murine brain. They found that a pressure drop of 1.2 to 3.3 mmHg was required for achieving believable CSF flow in penetrating PVS. Their high pressure drop might be partially explained by their small PVS sizes. Still, like with Ray, Iliff and Heys (2019), their pressure differences are higher than we would expect, although Tithof et al. (2022) mark that their low resistance scenario only requires a pressure drop of 0.2 mmHg. The authors themselves point out that a pressure drop of 1.2 - 3.3 mmHg is of marginal feasibility. They point to Penn and A. Linninger (2009) found that the largest possible transmantle pressure difference in humans is 1 mmHg.

Another article studying perivascular flow is Kedarasetti, Drew and Costanzo (2021). The authors simulate perivascular flow at the penetration point where the artery enters the brain parenchyma. They do not give exact numbers for the perivascular, v_{PVS}, and extracellular, v_{ECS}, fluid speeds, but instead give the ratio between them. They found the ratio v_{PVS}/v_{ECS} to be 1.62 to 2.91 during arterial vasodilation. Our model found the PVS speeds to be significantly greater than the ECS speeds. In the grey matter, the arterial PVS speed was 8 times as great as the extracellular fluid speeds. This is larger than what is reported by Kedarasetti, Drew and Costanzo (2021). We believe this difference is due partially to us not having taken arterial pulsations into account. An other possibility is that the computational mesh used in Kedarasetti, Drew and Costanzo (2021) is only at the surface of the brain parenchyma, going 150 μm deep. The grey matter, however, is several millimeters thick (Winkler et al. (2010), Kabani et al. (2001)), and hence our computed grey matter velocity covers a significantly larger area.

Our model underestimates cerebral blood flow in the capillaries and veins. We have set the transfer coefficients to ensure mass conservation, and it is seen in the transfer rates in both Section 7.1 and Section 7.2 that the cerebral

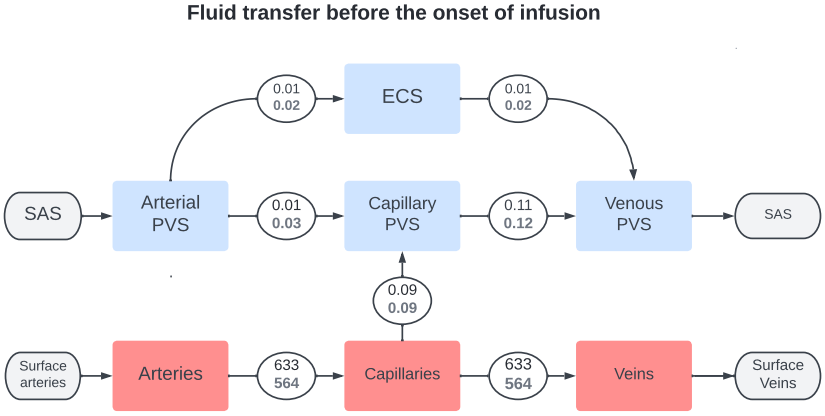

Figure 8.1: Average total fluid transfer rates in ml/min between compartments before the onset of infusion. Top numbers show the control average, the grey bottom numbers show the iNPH average values. Blue compartments are filled with CSF/ISF, red compartments with blood. Due to the significant methodological challenges with computing in- and outflow from BC (Kovzar and Lozzi-Kovzar (2017), Józsa et al. (2021)), the in- and outflow through the boundary is not shown. Here, PVS is short for perivascular space, ECS is short for extracellular space and SAS is short for subarachnoid space.

transfer between capillaries and veins is the same as the one between arteries and capillaries. The blood flow rate is somewhat lower than what we would expect, but this is due to us setting a uniform inflow field over the entire cortex. However, when we specified arterial inflow we computed the average blood flux per surface area. Afterwards, we used a Neumann condition to ensure that the total blood flow through the surface area would be the same as the one measured by Anders Eklund. The error was introduced by us using the entire brain surface area when computing the average flux, not just the cortical surface. As such, we effectively scaled down arterial inflow since we only had arterial inflow through the pial surface. We do, however believe the error introduced this way to be of little importance. Arterial inflow rate does not affect perivascular and extracellular pressure in any noteworthy degree, as reported in Chapter 6. Most of the CSF outflow from the PVS before infusion starts is fluid that leaked from the capillaries to the capillary PVS, see Figure 8.1. After infusion starts, however, this fluid exchange diminishes while the PVS fluid exchange increases drastically as seen in Figure 8.2.

Many simulation studies, like those of Sobey et al. (2010) and Sobey et al. (2012), do not assume any fluid transfer between blood and CSF/ISF. Others, like Tully and Ventikos (2011) and Guo, Li et al. (2019), assume flow from capillaries to the PVS/ECS and flow from the CSF/ECS to the veins. We do have a semi-agreement with latter model, as the biggest source of perivascular CSF before the start of infusion is capillary filtration. This CSF, however, never enters the ECS. By not separating the PVS and ECS, Tully and Ventikos (2011) and Guo, Li et al. (2019) are not able to check to what extent the ECS manages to exchange fluid with the CSF, a phenomenon our model is theoretically able

to capture.

The response to infusion.

Most of the literature on what happens deep into the brain parenchyma considers the waterscape at rest. As a result, our comparisons thus far have considered only what happens before the start of infusion. This will be the topic of this section.

There exist some observations and simulation studies that might give an indication of what happens after infusion starts. As noted by Vinje et al. (2020), the tracer injection rates of, for instance, Mestre et al. (2018), Bedussi et al. (2018) and Iliff, M. Wang, Zeppenfeld et al. (2013) are analogous to an infusion test due to the lower CSF volume in mice. Vinje et al. (2020) states that an infusion of tracer molecules at a rate of 0.15 μl/min into the murine brain is comparable to an infusion test of 1.5 ml/min in humans. The mouse brain has an average volume of 509 mm^3 (Badea, Ali-Sharief and Johnson (2007)). In our simulations, both the control group and the iNPH group have an average cerebral volume of over one litre, a factor 2000 times greater than the murine brain. As a result, we do not believe the numbers can be compared directly, but should instead be indicative of general trends.

Iliff, M. Wang, Zeppenfeld et al. (2013) and Bedussi et al. (2018) both observe tracers entering the brain parenchyma through perivascular pathways. This corroborates our findings that perivascular flow speeds should be higher than extracellular flow speeds before as well as under infusion. Furthermore, Thrane et al. (2013) injected solutes in-vivo into the interstitium of mice and observed velocities with a magnitude of over 1 μm/s, evidencing that significant flow speeds are possible under the right conditions. Infusion tests are not performed from within the brain parenchyma, and we would hence not expect the ISF flow to attain speeds of this magnitude in the extracellular space. Guo, Vardakis et al. (2020) implemented a four-compartment MPET model similar to that of Tully and Ventikos (2011), and used the experimental data from tracer injection in mice to verify that their model responded well to an infusion test. They did not compute compartmental velocities nor the inter-compartmental transfer during the simulation, but did demonstrate that the combined PVS/ECS pressure should follow the curve of the ICP. This trend is also observed for our model. In Section 7.1, we used the same applied CSF pressure for all patients. This pressure was computed using the model of Vinje et al. (2020) and with an infusion rate of 1.5 ml/min. This leads to a plateau pressure of 24.2 mmHg, and, as can be seen from Figure 7.5, Figure 7.6 and Table 7.1, this value was neither exceeded by the pressure within any of the perivascular compartments nor within the ECS. Furthermore, the pressure curves follow the shape of the ICP seen in infusion test, see Figure 4.2.

Sobey et al. (2012), based on Sobey et al. (2010), used a two-compartment poroelastic model to investigate the effects of infusion tests. They used one compartment for CSF and one for blood. The main focus of the article was to extend classical ODE models for ICP during infusion to also account for arterial pulsation. Yet, they also investigated the spatial dependence on the ICP, and discovered that strain, displacement and CSF volume change fell rapidly moving away from the domain boundary. ICP, on the other hand, remained virtually constant throughout the parenchyma. Their domain assumed the brain to be a

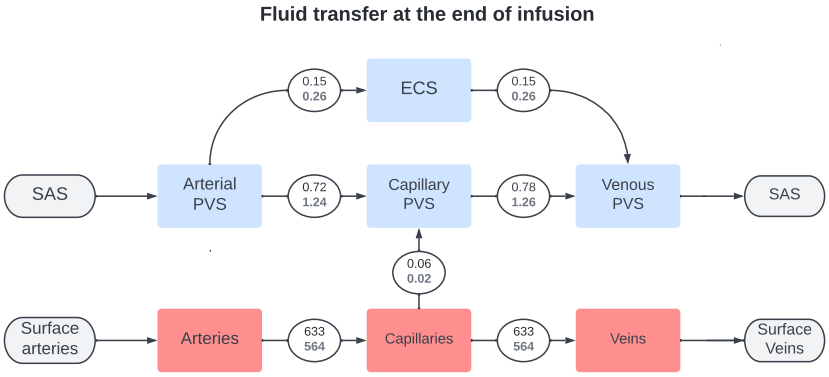

Figure 8.2: Average total fluid transfer rates in ml/min between compartments at the end of simulation. Top numbers show the control average, the grey bottom numbers show the iNPH average values. Blue compartments are filled with CSF/ISF, red compartments with blood. Due to the significant methodological challenges with computing in- and outflow from BC (Kovzar and Lozzi-Kovzar (2017), Józsa et al. (2021)), the in- and outflow through the boundary is not shown. Here, PVS is short for perivascular space, ECS is short for extracellular space and SAS is short for subarachnoid space.

spherical shell of a given thickness, and most of the functionals they computed are different from our quantities of interest. Yet, interestingly, they seem to be in agreement with us when it comes to ICP. While our ECS and PVS pressure is not the same as ICP, we observe little difference in average pressure in the grey and white matter. Although we do have large local pressure gradients in the grey matter, they average out to the same level as the white matter. See for instance Figure 7.17a and Figure 7.17b. The studies of Sobey et al. (2012) can, however, not be used to compare with our results regarding perivascular and extracellular flow, as all CSF is lumped into a single compartment.

When it comes to ISF speeds, our computed values at, or close to, the end of infusion were between 7 and 8 nm/s for the average control patient. The numbers were similar both with and without patient specific boundary conditions. This is higher than what we computed for the system at rest. The same trend is observed for the iNPH patients. For this group the average ISF speed increased by around 10 nm/s after infusion. When using patient specific boundary conditions, the increase in average ISF speed for iNPH patient is higher than for the control group. It is, however, not large enough to be immediately discarded as unphysical. As injection of fluid increases pressure, a higher ISF speed after than before infusion is to be expected, and, expect for a few cases, our average speeds are either within or close to the range of Holter et al. 2017.

It seems clear that the computed pressure fields in Section 7.1 and the functionals derived from them are implausible for the iNPH group. If these results were accurate, the iNPH and control groups would have a near identical reaction to infusion tests. The cerebral CSF system is, however, drastically changed for the iNPH patients compared to that of healthy individuals. For

example, P. K. Eide, L. M. Valnes et al. (2021) found that CSF flow rates and pressure gradients were higher in the sylvan aqueduct for iNPH patients than in healthy adults. The same phenomenon was also observed by Lindstrøm et al. (2018). In Section 7.1, however, the fluid velocities and transfer rates were almost identical between the two groups. While we have not modelled aqueductal CSF flow, the observations of Lindstrøm et al. (2018) and P. K. Eide, L. M. Valnes et al. (2021) nevertheless indicates a systematic change in the CSF flow pattern within the brain, which is not captured by our model.

The data provided by Anders Eklund also casts doubt on the results of Section 7.1 for the iNPH patients. The control group had an average R_{out} of 10.0 mmHg/(ml/min). The corresponding value for the iNPH group was 18.1 mmHg/(ml/min). It should be remarked that the R_{out} factor is a lumped outflow resistance parameter, and cannot represent outflow through many different channels (Vinje et al. (2020)). Still, it is difficult to imagine that penetrating PVS, and by extension the ECS which the PVS communicate with, is not affected by a changed CSF flow pattern from an increased outflow resistance. In Section 7.1, we applied the same boundary condition for CSF pressure, and hence also assumed the same value of R_{out}, on all patients. This contradicts the data provided by Anders Eklund. It is therefore not surprising that the results of Section 7.1 would be unsatisfactory in capturing the response of the iNPH group to infusion tests.

Yet, the results for the iNPH group in Section 7.2 allowing for patient specific boundary conditions is not fully satisfactory either. Vinje et al. (2020), who developed the model we used for CSF pressure in the SAS, gives an upper limit of 23-26 mmHg for ICP before their model assumption of a pressure independent R_{out} no longer applies. This upper limit was computed by Andersson, Malm and Eklund (2008). With an infusion rate of 1.5 ml/min and baseline pressure of 10 mmHg, we would expect from Equation (4.39) to observe an ICP plateau of 25 mmHg in the average control and 37 mmHg in the average iNPH patient. Many patients in both group ended up within the upper bound of Vinje et al. (2020) and Andersson, Malm and Eklund (2008). Some, however, plateaued at a significantly higher level than 25 mmHg. This casts doubt on our model. Yet, Ryding, Kahlon and Reinstrup (2018) computes the outflow resistance of patients whose ICP plateaued at well over 40 mmHg. The authors do not specify a separate method to calculate R_{out} for these patients, suggesting that the resulting pressure curve was similar enough to when ICP plateaues at lower values for the same approach to be used. Hence, the pressure might be incorrectly high only on the boundary for the patients with the strongest response.

Many patients in both groups exhibit implausible fluid transfer rates in the PVS and ECS. In Figure 7.27b we see the total fluid transfer between the venous PVS and its connected compartments. The highest observed inflow rate from the capillary PVS to the venous PVS is over 2.5 ml/min, which is significantly higher than the combined CSF production rate of 1.83 ml/min. We have, when modelling the CSF pressure in the SAS, assumed a one way communication between SAS and CSF. For this assumption to hold true, the perivascular CSF flow has to only constitute a small contribution to the CSF pressure. This is unlikely when PVS flow rates reach well above half of the combined CSF production rate.

In addition, fluid transfer rates are likely exaggerated in several patients,

and it is quite possible that the iNPH group should have lower fluid transfer rates than the control group. For instance, P. K. Eide and Ringstad (2019) found delayed CSF tracer clearance in the entorhinal cortex for iNPH patients compared to their control group. This is the opposite from what we have observed when implementing patient specific boundary conditions. It should, however, be pointed out that P. K. Eide and Ringstad (2019) analysed tracer clearance under normal circumstances and not during infusion. Nevertheless, the fact that the iNPH group cleared the tracers slower than the healthy individuals in this study, could indicate that there are some inaccuracies regarding the material parameters in our model and that modifications are in order. As the CSF pressure undoubtedly is higher in iNPH patients during infusion, we would expect both higher average pressures and pressure gradients in the CSF filled compartments. This is a clear trend in Table 7.6 and Table 7.10, where we can see the average pressure and average pressure gradient is higher in the iNPH group than in the control group in all PVS compartments and the ECS. Yet, higher pressure and larger gradients does not necessarily guarantee higher fluid flow rates. If the tissue is compressed, as suggested by Scollato et al. (2008), it does not seem unreasonable that the permeability of the brain tissue is decreased as well. Hence, it is possible that a decrease in hydraulic conductivity could completely offset the increase in speed and transfer from the increased CSF pressure, or even decrease the fluid speed compared to healthy adults. Such aspects have not been included in our model, but there are articles suggesting that this might be the case, such as Assaf et al. (2006) and Kaczmarek, Subramaniam and Neff (1997). We will discuss possible modifications later in this chapter.

We have not observed increased fluid flow between vascular compartments as the ICP rises during our simulations. Pressure do rise in all vascular compartments, but the fluid transfer rates are not affected. Both before and after infusion, average fluid flow between the vascular compartments were at a rate of 633 ml/min in the control group and 564 ml/m,in in the iNPH group. Cerebral auto-regulation is the phenomenon where the brain is able to regulate the conditions for blood flow to ensure that it is not disrupted by large changes in arterial blood pressure. S. Payne (2016) states that the cerebral autoregulation can handle changes in arterial blood pressure of $\pm$ 50%, and Paulson, Strandgaard and Edvinsson (1990) states cerebral autoregulation is active when arterial blood pressure is in the range of 60-160 mmHg. None of our simulations produced arterial blood pressure exceeding 120 mmHg. Hence, we would not expect our model, if accurate, to have a drastically changed vascular transfer rates during infusion.

Experimental measurements by Ivanov, Kalinina and Levkovich (1981) indicate that blood flow speed in cerebral capillaries is around 0.79 mm/s in the smallest capillaries and 2.43 mm/s in arterioles. We, on the other hand, have computed arterial blood velocities of 2.99 mm/s and 2.74 mm/s for the control and iNPH group respectively. In the capillaries, these numbers were 52.2 μm/s and 47.8 μm/s. Hence, our arterial speeds are slightly larger than the arteriolar blood speeds measured by Ivanov, Kalinina and Levkovich (1981) . Our capillary speeds are, however a factor 10 slower than the measured capillary speeds and slower than the arteriolar speed by a factor of 500. In our model, we have not considered arteriolar and venular flow. The arterioles and venules are the vascular vessels connecting the capillaries to the arteries and veins. Hence the

arteriolar flow is integrated into the arterial and capillary compartments, which might explain some of the discrepancy. Given the measured flow speeds in the arterioles, it seems reasonable to assume a majority of the arterioles are captured in our arterial network. However, our computed capillary flow is still lower than what is observed within the capillaries alone. An underestimation of capillary permeability or porosity, or the uncertainties inherent in measuring these quantities, could play a role in the observed differences, and these parameters should be investigated further.

8.3 Limitations and further work

We will now discuss the limitations of our work. To start, there is an error in how we specified the arterial inflow rate, resulting in an underestimation of vascular pressure. From Chapter 6 we notice that arterial inflow has little effect on extracellular and perivascular pressures. The most important connection between the vascular system and the PVS was, in our model, capillary filtration between the capillaries and capillary PVS. Lower vascular pressure might lead to an under-estimation of the filtration rate.

In Vinje et al. (2020) the authors found that both before and after infusion, the CSF flow in the penetrating PVS only constituted a small part of the total CSF flow. As a result, we chose to model the SAS-PVS fluid exchange as a one-way communication. That being said, our computed transfer rates between compartments at the end of infusion is over 1 ml/min in the control group and 1.5 ml/min in the iNPH group. This means that over half of the combined CSF production rate goes through the PVS in our model for both the control and iNPH group. It is implausible at best that this would not also have a measurable impact on the ICP. It is therefore very likely that some of our results, especially on the higher end of the scale, are exaggerated.

The assumption of linearly dependent R_{out} holds to 25-26 mmHg, as explained by Andersson, Malm and Eklund (2008). Patient NPH2 had an R_{out} of 38.9 mmHg/(ml/min) and a baseline ICP of 11.8 mmHg. With infusion at 1.5 ml/min and a linear increase in pressure, NPH2 would end up with a ICP plateau of 70.2 mmHg. This is almost three times the limit of Andersson, Malm and Eklund (2008). While most control patients and several of the NPH patients stayed within, or just above the linearity limit of 26 mmHg, there also were several that did not. Not taking this into account means a likely overestimation of CSF pressure on the domain boundary.

The interaction between the SAS and the parenchyma during infusion tests warrants further investigation. Although some work exist, like that of Vinje et al. (2020) and Sobey et al. (2012), the degree of communication between the two is still not known. Some possible extensions here include coupling our modified MPET model with the ODE of Vinje et al. (2020) so the communication goes both ways, and simulations where the deformation $\mathbf{u}$ of the brain parenchyma is computed as well. Both ventures might reveal crucial insight into CSF flow patterns and the disease of iNPH.

The sizes of the perivascular channels are unclear, and due to their small sizes measurements are difficult deep within the brain. Furthermore, Mestre et al. (2018) demonstrated that the perivascular spaces in mice collapsed shortly after death. This indicates that accurate measurements needs to be done in-vivo,

further exacerbating the difficulties of measuring the sizes of the PVS. As a result, estimates vary wildly. Tithof et al. (2022) estimated them to have a cross-sectional area of 36 % of that of the vascular system. Kedarasetti, Drew and Costanzo (2021) operated with a PVS with a cross-sectional area equal to 86% of the vascular system, and the tracer experiment of Pizzo et al. (2018) seem to suggest the capillary PVS to be roughly the same size as the cross sectional area of the capillaries. Lastly, if the markings of blood vessels and PVS are to scale, figure 3 in Ray, Iliff and Heys (2019) suggests a perivascular cross-sectional area of 1.72 times that of the blood vessels. The sizes of the PVS vessels are important for accurate modelling of cerebrospinal fluid flow. The permeability of the PVS are inversely proportional to $(r_1/r_2)^4$ (Vinje et al. (2020)), with r_1 being the vascular radius and r_2 being the radius of the combined vascular vessel and PVS. The cross sectional area, however, is proportional to $(r_1/r_2)^2$. Hence, a relative increase in PVS to vascular width has a significant effect on both permeability and porosity of the compartment. This makes accurate measurement of the size of the PVS crucial for a good estimation of fluid speed in the PVS. The lack of and difficulty in obtaining such measurements is indeed a limiting factor of our model.

There exist ample documentation that the white matter of the brain is anisotropic (Le Bihan et al. (2001), Zhao and Ji (2019), Tournier, Mori and Leemans (2011)) and experimental studies has shown that white matter anisotropy is altered in hydrocephalic patients (Assaf et al. (2006)). We have, however, in our model treated the brain as a fully isotropic medium. The danger of over-specification is always present when extending a model, but we believe the assumption of white matter isotropy might have lead to inaccurate flow patterns in the white matter.

We used the same constant compliance for each compartment. In reality, however, compliance is neither constant in time nor through compartments. This is illustrated by e.g. Aoi et al. (2009) who used an ODE to model how the vascular compliance changed when a person went from sitting to standing. Furthermore, Bateman (2000) found the vascular compliance of iNPH patients to be lower than that of healthy individuals before intervention and higher than the healthy control compliance after. Hence, a common compliance for all patients and all compartments is an idealisation which does reflect nature. There is also, to our knowledge, little published work on the compliance in the ECS and penetrating PVS.

We did not perform systematic sensitivity analysis of most parameters in our model. The only parameters to receive a systematic review were arterial inflow, mesh resolution and time step. We also performed tests on several different values for the coefficients β_1, β_2 and β_3, but these were not done systematically and hence are likely not optimised. The uncertainties inherent in many parameters leads to a wide array of possible results. For instance, Ray, Iliff and Heys (2019) found that ECS fluid speed could differ by several orders of magnitude depending on permeability and pressure gradient. This limitation is inherent to biomechanical modelling of the brain, and can only be remedied by extensive research. Inquiries into the mechanical properties of the brain, either by simulation or experiment, is vital to further our understanding of the biomechanical processes governing the cerebral waterscape.

A limitation of poroelastic models such as MPET is the reliance on homogenisation. Homogenisation works by assuming the individual penetrating

porous network are on a smaller length scale than the tissue it penetrates (see e.g. Shipley et al. (2020), Penta and Ambrosi (2015)). Our MRI images have a resolution of 1 mm^3. This resolution makes the homogenisation of the capillaries relatively unproblematic, as they are, on average, only 50 μm apart (Penta and Ambrosi (2015)). The penetrating arteries and veins, are however significantly larger and further apart from each other than the capillaries. In figure 3E in Kirst et al. (2020) we see a 1 mm 2D mapping of the arteries and veins of a murine cerebellum. Within this zone, we observe 2-3 penetrating arteries, and this density seem replicated outside the 1mm zone. While the exact density is hard to infer, the distance between and size of the arteries are significantly lower than 1 mm, which means it would not be able to see these vessels on our MRI images. Yet, a inter-arterial distance of 0.5 mm makes it difficult to justify that the density is high enough for the homogenisation assumption to be entirely accurate. With a finer MRI image, a possible extension to our model is to model the arteries and veins as 1D fluid networks, giving us a 1D-3D model for the entire parenchyma. The increased gain in model accuracy from this approach would, however, come with increased numerical complexity.

A final possible extension of our work is revisiting our assumption of the ventricles being impermeable membranes. Some studies seem to suggest that CSF might leak from the ventricles in hydrocephalus patients (Bradley (2015)). Modelling the ventricular CSF pressure, and the possible fluid interaction with the parenchyma could prove promising.

8.4 Conclusion

Our results in Section 7.1 indicate that the isolated effect of the brain geometry is of little importance in our model. Interpersonal variance was low both within and across groups in pressure, fluid speed and fluid transfer. Looking at our simulations in Section 7.2, we clearly see the effect of the applied boundary conditions. The iNPH group had a much stronger recorded response to an infusion test, and this applied CSF pressure also propagated into the parenchyma as a whole. We believe this, in conjunction with the results in Section 7.1, point towards three things.

First, our results are in, for the most part, agreement with the literature before infusion starts. We computed low fluid speeds in the ECS, and higher flow rates in the PVS. The latter are, however somewhat lower than that of other simulation studies. Still, the trend in our result follows the general consensus on the glymphatic hypothesis, as outlined by Abbott et al. (2018).

Secondly, the applied boundary condition has a significant impact on the perivascular and extracellular compartments, as shown in Section 7.2. Unlike in Section 7.1, the iNPH group shows a stronger response than the control group in Section 7.2. Pressure, fluid speed and fluid transfer rates are increased in the NPH group when patient specific boundary conditions were used. As explained in Section 8.3, there are problematic aspects with the way the patient specific boundary condition was applied. Due to the importance of the boundary condition, it is crucial to rectify these problems. To summarise, we identify two aspects which needs to be improved, namely the one-way communication between PVS and SAS, and the linearity of the outflow resistance. The one way communication is the most important as with our computed transfer rates,

the parenchymal flow would undoubtedly affect SAS pressure. The linearity of R_{out} should also be evaluated, as the assumption might lead to unrealistically high CSF pressure values.

Finally, our results imply that the mechanical parameters used in our model is changed for the NPH patients. Both the internal parameters, namely those listed in Table 4.1, and the external parameters used for CSF pressure need to be altered to model the iNPH group better. The simulations done by Vinje et al. (2020) suggest that the PVS is far from the biggest clearance route from the SAS. Furthermore, our model states that the CSF is cleared back into the SAS after it has gone through the brain. Consequently, increased intraparenchymal flow resistance alone is insufficient to explain the increased ICP measured during infusion tests. Other outflow routes are likely to be changed as well. That being said, the results from Section 7.2 also show that even with patient specific boundary conditions and geometry, our computed pressure fields are still unsatisfactory for the NPH group. Before the onset of infusion, the average pressure, fluid velocity and fluid transfer rate are almost identical in the two groups. This stand in sharp contrast to e.g. Lindstrøm et al. (2018), P. K. Eide and Ringstad (2019), P. K. Eide, L. M. Valnes et al. (2021) and Bateman (2000) who all observe a changed waterscape of the human brain in iNPH patients. Our computational model allow us to study an infusion test within the parenchyma in detail. However, accurate determination of how iNPH changes the mechanical and physical properties on both a microscopic and macroscopic scale warrants further investigation and validation of our model.

List of Figures

2.1 Illustration of the waterscape of the brain. 8
2.2 Illustration of the geometry of a penetrating artery and the surrounding PVS. 10

4.1 Flowchart showing how the compartments are connected together. 18
4.2 ICP pressure graph from a performed infusion test 29
4.3 Linear model relating outflow resistance to the model of Vinje et al. (2020) 30

5.1 Segmentation of lateral ventricles done poorly by FreeSurfer 34
5.2 Illustration of how the segmentation was corrected using FreeView 34
5.3 A possible tail of the right lateral ventricle. 35
5.4 Illustration of what regions were chosen when conducting convergence estimation 36
5.5 Figure showing how the partial mesh looked 37
5.6 Illustration of a mesh with a high resolution, RP64 37
5.7 Image of a mesh with low resolution, RP16 37

6.1 Spatial resolution sensitivity for the ECS pressure using CG1 and CG2 schemes. 39
6.2 Spatial resolution sensitivity for the venous pressure using CG1 and CG2 schemes. 39
6.3 Spatial resolution sensitivity for the venous PVS pressure using CG1 and CG2 schemes 40
6.4 Figure showing venous pressure dependence on temporal resolution 40
6.5 Illustration on ISF pressure on temporal resolution 41
6.6 ECS pressure dependence on arterial bloodflow 42
6.7 Venous dependence on incoming blood flow 43

7.1 Comparison between average ECS pressure and average arterial PVS pressure under same conditions 46
7.2 Comparison between average ECS pressure in the grey and white matter when subjected to the same SAS CSF pressure. 46
7.3 Comparison between average arterial PVS pressure in the grey and white matter when subjected to the same SAS CSF pressure. . . . 47
7.4 Comparison between average arterial pressure in the grey and white matter when subjected to the same SAS CSF pressure. 47

7.5 ECS pressure field in one control and one NPH patient. Same boundary conditions. 48
7.6 Venous PVS pressure field in one control and NPH patient. Same boundary conditions. 48
7.7 Pressure field in venous compartment for one control and one NPH patient. Same boundary conditions. 49
7.8 Comparison between fluid speed in ECS and arterial PVS when subjected to the same CSF boundary condition 51
7.9 Comparison between fluid speed in ECS grey and white matter. . 51
7.10 Comparison between fluid speed in arterial PVS grey and white matter. 52
7.11 Comparison between fluid speed in the arterial compartment in the parenchyma and in the grey matter. 52
7.12 Comparison of fluid transfer rates in the ECS and venous PVS when subjected to the same CSF boundary condition 55
7.13 Comparison of fluid transfer rates in the ECS grey and white matter the same CSF boundary condition 55
7.14 Comparison of fluid transfer rates in the venous PVS grey and white matter the same CSF boundary condition 56
7.15 Comparison fluid transfer rates in the capillary compartment in the entire parenchyma and in the grey matter 56
7.16 Comparison between average ECS pressure and average arterial PVS pressure under patient specific boundary conditions. 60
7.17 Comparison between average ECS pressure in the grey and white matter under patient specific boundary conditions. 60
7.18 Comparison between average arterial PVS pressure in the grey and white matter under patient specific boundary conditions. 61
7.19 Comparison between average arterial PVS pressure in the grey and white matter under patient specific boundary conditions. 61
7.20 The computed ECS pressure fields of two patients toward the end of infusion. One healthy and one NPH patient. 62
7.21 The computed venous PVS pressure fields of two patients toward the end of infusion. One healthy and one NPH patient. 62
7.22 The computed venous pressure fields of two patients toward the end of infusion. One healthy and one NPH patient. 63
7.23 Comparison between fluid speed in ECS and arterial PVS when subjected to patient specific CSF boundary condition 65
7.24 Comparison between fluid speed in ECS grey and white matter, when subjected to patient specific boundary condition. 66
7.25 Comparison between fluid speed in arterial PVS grey and white matter, when subjected to patient specific boundary condition. . . 66
7.26 Comparison between fluid speed in arterial PVS grey and white matter, when subjected to patient specific boundary condition. . . 67
7.27 Figure comparing the fluid exchange rates of the ECS (left) and venous PVS (right) during infusion when patient specific BC were used. 71
7.28 Figure comparing the fluid exchange rates of the ECS grey matter (left) and ECS white matter (right) during infusion when patient specific BC were used. 71

7.29 Figure comparing the fluid exchange rates of the venous PVS grey matter (left) and venous PVS white matter (right) during infusion when patient specific BC were used. 72
7.30 Figure comparing the fluid exchange rates of the capillary grey matter (left) and capillary white matter (right) during infusion when patient specific BC were used. 72

8.1 Overview of fluid flow in the brain before infusion 78
8.2 Overview over fluid flow in the brain during the stabilised phase of an infusion test. 80

List of Tables

4.1 Model parameter overview 23
4.2 Table showing the hydraulic conductivity of each compartment . . 24
4.3 Table showing each nonzero transfer coefficient ω_{ij}. 27
4.4 Table showing our chosen values for the porosities ϕ_i. 27

7.1 Pressure averages at the end of infusion under same applied boundary conditions 49
7.2 Average speed at the end of infusion under same applied boundary conditions 53
7.3 Average pressure gradients at the end of infusion under same applied boundary conditions 53
7.4 Fluid transfer rate at the end of infusion when all patients are subjected to the same CSF pressure 57
7.5 Pressure averages before the start of infusion under patient specific boundary condition 59
7.6 Pressure averages at the end of infusion under patient specific boundary conditions 63
7.7 Average speed before infusion under patient specific boundary conditions 65
7.8 Average speed at the end of infusion under same patient specific boundary conditions 67
7.9 Average pressure gradients before infusion under same patient specific boundary conditions 68
7.10 Average pressure gradients at the end of infusion under patient specific boundary conditions 68
7.11 Fluid transfer rate before infusion when all patients are subjected to patient specific BC 73

7.12 Fluid transfer rate at the end of infusion when all patients are subjected to patient specific BC 73

Bibliography

Abbott, N. J. et al. (2018). 'The role of brain barriers in fluid movement in the CNS: is there a 'glymphatic' system?' eng. In: *Acta neuropathologica* vol. 135, no. 3, pp. 387–407.

Aifantis, E. C. (1979). 'Continuum basis for diffusion in regions with multiple diffusivity'. In: *Journal of Applied Physics* vol. 50, no. 3, pp. 1334–1338.

Aifantis, E. C. and Hill, J. M. (1980). 'On the theory of diffusion in media with double diffusivity I. Basic mathematical results'. In: *The Quarterly Journal of Mechanics and Applied Mathematics* vol. 33, no. 1, pp. 1–21.

Alnæs, M. et al. (2015). 'The FEniCS project version 1.5'. In: *Archive of Numerical Software* vol. 3, no. 100.

Andersson, N., Malm, J. and Eklund, A. (2008). 'Dependency of cerebrospinal fluid outflow resistance on intracranial pressure'. In: *Journal of neurosurgery* vol. 109, no. 5, pp. 918–922.

Andrén, K. et al. (2021). 'Early shunt surgery improves survival in idiopathic normal pressure hydrocephalus'. In: *European Journal of Neurology* vol. 28, no. 4, pp. 1153–1159. eprint: https://onlinelibrary.wiley.com/doi/pdf/10.1111/ene.14671.

Aoi, M. et al. (2009). 'Modeling cerebral blood flow and regulation'. In: *2009 Annual International Conference of the IEEE Engineering in Medicine and Biology Society*. IEEE, pp. 5470–5473.

Assaf, Y. et al. (2006). 'Diffusion tensor imaging in hydrocephalus: initial experience'. In: *American journal of neuroradiology* vol. 27, no. 8, pp. 1717–1724.

Badea, A., Ali-Sharief, A. A. and Johnson, G. A. (2007). 'Morphometric analysis of the C57BL/6J mouse brain'. In: *Neuroimage* vol. 37, no. 3, pp. 683–693.

Bai, M., Elsworth, D. and Roegiers, J.-C. (1993). 'Multiporosity/multipermeability approach to the simulation of naturally fractured reservoirs'. In: *Water Resources Research* vol. 29, no. 6, pp. 1621–1633.

Barichello, T. (2019). *Blood-Brain Barrier*. eng. 1st ed. 2019. Vol. 142. Neuromethods. New York, NY: Springer New York : Imprint: Humana.

Bateman, G. A. (2000). 'Vascular compliance in normal pressure hydrocephalus'. In: *American Journal of Neuroradiology* vol. 21, no. 9, pp. 1574–1585.

Bateman, G. A. and Siddique, S. H. (2014). 'Cerebrospinal fluid absorption block at the vertex in chronic hydrocephalus: obstructed arachnoid granulations or elevated venous pressure?' In: *Fluids and Barriers of the CNS* vol. 11, no. 1, pp. 1–10.

Bedussi, B. et al. (2018). 'Paravascular spaces at the brain surface: Low resistance pathways for cerebrospinal fluid flow'. In: *Journal of Cerebral Blood Flow & Metabolism* vol. 38, no. 4, pp. 719–726.

Biomedical Imaging, A. A. M. C. for (2021). eng.

El-Bouri, W. K. and Payne, S. J. (2015). 'Multi-scale homogenization of blood flow in 3-dimensional human cerebral microvascular networks'. eng. In: *Journal of theoretical biology* vol. 380, pp. 40–47.

Bradley Jr, W. G. (2015). 'CSF Flow in the Brain in the Context of Normal Pressure Hydrocephalus'. eng. In: *American journal of neuroradiology : AJNR* vol. 36, no. 5, pp. 831–838.

Brean, A. and Eide, P. (2008). 'Prevalence of probable idiopathic normal pressure hydrocephalus in a Norwegian population'. In: *Acta neurologica Scandinavica* vol. 118, no. 1, pp. 48–53.

Brinker, T. et al. (2014). 'A new look at cerebrospinal fluid circulation'. In: *Fluids and Barriers of the CNS* vol. 11, no. 1, pp. 1–16.

Chong, P. L. et al. (2022). 'Sleep, cerebrospinal fluid, and the glymphatic system: A systematic review'. In: *Sleep medicine reviews* vol. 61, p. 101572.

Daou, B. et al. (2016). 'Revisiting secondary normal pressure hydrocephalus: does it exist? A review'. In: *Neurosurgical focus* vol. 41, no. 3, E6.

Daversin-Catty, C. et al. (2020). 'The mechanisms behind perivascular fluid flow'. eng ; nor. In: *PloS one* vol. 15, no. 12, e0244442–e0244442.

Deisenhammer, F. et al. (2015). *Cerebrospinal Fluid in Clinical Neurology*. eng. 1st ed. 2015. Cham: Springer International Publishing : Imprint: Springer.

DeSaix, P. et al. (2020). *Openstax Anatomy and Physiology*. URL: https://openstax.org/details/books/anatomy-and-physiology?Book%5C%20details (visited on 27/04/2022).

Dutta-Roy, T., Wittek, A. and Miller, K. (2008). 'Biomechanical modelling of normal pressure hydrocephalus'. eng. In: *Journal of biomechanics* vol. 41, no. 10, pp. 2263–2271.

Eide, P. K. and Ringstad, G. (2019). 'Delayed clearance of cerebrospinal fluid tracer from entorhinal cortex in idiopathic normal pressure hydrocephalus: a glymphatic magnetic resonance imaging study'. In: *Journal of Cerebral Blood Flow & Metabolism* vol. 39, no. 7, pp. 1355–1368.

Eide, P. K. and Sæhle, T. (2010). 'Is ventriculomegaly in idiopathic normal pressure hydrocephalus associated with a transmantle gradient in pulsatile intracranial pressure?' In: *Acta neurochirurgica* vol. 152, no. 6, pp. 989–995.

Eide, P. K., Valnes, L. M. et al. (2021). 'Direction and magnitude of cerebrospinal fluid flow vary substantially across central nervous system diseases'. In: *Fluids and Barriers of the CNS* vol. 18, no. 1, pp. 1–18.

Esmonde, T. and Cooke, S. (2002). 'Shunting for normal pressure hydrocephalus (NPH)'. In: *Cochrane database of systematic reviews*, no. 3.

Evans, L. C. (2010). *Partial differential equations*. eng. 2nd ed. Vol. vol. 19. Graduate studies in mathematics. Providence, R.I: American Mathematical Society.

Faghih, M. M. and Sharp, M. K. (2018). 'Is bulk flow plausible in perivascular, paravascular and paravenous channels?' eng. In: *Fluids and barriers of the CNS* vol. 15, no. 1, pp. 17–17.

Gideon, P. et al. (1994). 'Cerebrospinal fluid flow and production in patients with normal pressure hydrocephalus studied by MRI'. In: *Neuroradiology* vol. 36, no. 3, pp. 210–215.

Guo, L., Li, Z. et al. (2019). 'On the validation of a multiple-network poroelastic model using arterial spin labeling MRI data'. In: *Frontiers in computational neuroscience*, p. 60.

Guo, L., Vardakis, J. C. et al. (2020). 'A multiple-network poroelastic model for biological systems and application to subject-specific modelling of cerebral fluid transport'. In: *International Journal of Engineering Science* vol. 147, p. 103204.

Hablitz, L. M. and Nedergaard, M. (2021). 'The Glymphatic System: A Novel Component of Fundamental Neurobiology'. In: *Journal of Neuroscience* vol. 41, no. 37, pp. 7698–7711.

Hakim, S. and Adams, R. (1965). 'The special clinical problem of symptomatic hydrocephalus with normal cerebrospinal fluid pressure'. eng. In: *Journal of the neurological sciences* vol. 2, no. 4, pp. 307–327.

Hakim, S., Venegas, J. G. and Burton, J. D. (1976). 'The physics of the cranial cavity, hydrocephalus and normal pressure hydrocephalus: mechanical interpretation and mathematical model.' In: *Surgical neurology* vol. 5, no. 3, pp. 187–210.

Holter, K. E. et al. (2017). 'Interstitial solute transport in 3D reconstructed neuropil occurs by diffusion rather than bulk flow'. eng. In: *Proceedings of the National Academy of Sciences - PNAS* vol. 114, no. 37, pp. 9894–9899.

Huo, B.-X., Greene, S. E. and Drew, P. J. (2015). 'Venous cerebral blood volume increase during voluntary locomotion reflects cardiovascular changes'. In: *Neuroimage* vol. 118, pp. 301–312.

Iliff, J. J., Wang, M., Liao, Y. et al. (2012). 'A paravascular pathway facilitates CSF flow through the brain parenchyma and the clearance of interstitial solutes, including amyloid β'. eng. In: *Science translational medicine* vol. 4, no. 147, 147ra111–147ra111.

Iliff, J. J., Wang, M., Zeppenfeld, D. M. et al. (2013). 'Cerebral arterial pulsation drives paravascular CSF–interstitial fluid exchange in the murine brain'. In: *Journal of Neuroscience* vol. 33, no. 46, pp. 18190–18199.

Ito, H. et al. (2001). 'Arterial fraction of cerebral blood volume in humans measured by positron emission tomography'. In: *Annals of nuclear medicine* vol. 15, no. 2, pp. 111–116.

Ivanov, K., Kalinina, M. and Levkovich, Y. I. (1981). 'Blood flow velocity in capillaries of brain and muscles and its physiological significance'. In: *Microvascular research* vol. 22, no. 2, pp. 143–155.

Jin, B.-J., Smith, A. J. and Verkman, A. S. (2016). 'Spatial model of convective solute transport in brain extracellular space does not support a "glymphatic" mechanism'. In: *Journal of General Physiology* vol. 148, no. 6, pp. 489–501.

Józsa, T. I. et al. (2021). 'On the sensitivity analysis of porous finite element models for cerebral perfusion estimation'. In: *Annals of Biomedical Engineering* vol. 49, no. 12, pp. 3647–3665.

Kabani, N. et al. (2001). 'Measurement of cortical thickness using an automated 3-D algorithm: a validation study'. In: *Neuroimage* vol. 13, no. 2, pp. 375–380.

Kaczmarek, M., Subramaniam, R. P. and Neff, S. R. (1997). 'The hydromechanics of hydrocephalus: steady-state solutions for cylindrical geometry'. In: *Bulletin of mathematical biology* vol. 59, no. 2, pp. 295–323.

Kahlon, B., Sundbärg, G. and Rehncrona, S. (2005). 'Lumbar infusion test in normal pressure hydrocephalus'. eng. In: vol. 111, no. 6, pp. 379–384.

Kedarasetti, R., Drew, P. J. and Costanzo, F. (2021). 'Arterial vasodilation drives convective fluid flow in the brain: a poroelastic model'. In: *bioRxiv*.

Kim, D.-J. et al. (2015). 'Thresholds of resistance to CSF outflow in predicting shunt responsiveness'. In: *Neurological Research* vol. 37, no. 4, pp. 332–340.

Kinoshita, K. et al. (2006). 'Importance of cerebral perfusion pressure management using cerebrospinal drainage in severe traumatic brain injury'. In: *Brain Edema XIII*. Springer, pp. 37–39.

Kirst, C. et al. (2020). 'Mapping the fine-scale organization and plasticity of the brain vasculature'. In: *Cell* vol. 180, no. 4, pp. 780–795.

Kovzar, I. and Lozzi-Kovzar, D. (2017). 'Flux determination using finite elements: global vs. local calculation'. In: *Technical Gazette* vol. 24, no. 1, pp. 247–252.

Langtangen, H. P. and Mardal, K.-A. (2019). *Introduction to Numerical Methods for Variational Problems*. eng. Vol. 21. Texts in Computational Science and Engineering (21). Cham: Springer International Publishing AG.

Le Bihan, D. et al. (2001). 'Diffusion tensor imaging: concepts and applications'. In: *Journal of Magnetic Resonance Imaging: An Official Journal of the International Society for Magnetic Resonance in Medicine* vol. 13, no. 4, pp. 534–546.

Lee, E., Wang, J. and Mezrich, R. (1989). 'Variation of lateral ventricular volume during the cardiac cycle observed by MR imaging.' In: *American journal of neuroradiology* vol. 10, no. 6, pp. 1145–1149.

Lee, S.-P. et al. (2001). 'Relative changes of cerebral arterial and venous blood volumes during increased cerebral blood flow: implications for BOLD fMRI'. In: *Magnetic Resonance in Medicine: An Official Journal of the International Society for Magnetic Resonance in Medicine* vol. 45, no. 5, pp. 791–800.

Lindstrøm, E. K. et al. (2018). 'Cerebrospinal fluid volumetric net flow rate and direction in idiopathic normal pressure hydrocephalus'. eng ; nor. In: *NeuroImage clinical* vol. 20, pp. 731–741.

Linninger, A. A. et al. (2009). 'A mathematical model of blood, cerebrospinal fluid and brain dynamics'. eng. In: *Journal of mathematical biology* vol. 59, no. 6, pp. 729–759.

Logg, A., Mardal, K.-A. and Wells, G. (2012). *Automated solution of differential equations by the finite element method: The FEniCS book*. Vol. 84. Springer Science & Business Media.

Malm, J. and Eklund, A. (2006). 'Idiopathic normal pressure hydrocephalus'. eng. In: *Practical neurology* vol. 6, no. 1, pp. 14–27.

Malm, J., Kristensen, B. et al. (1995). 'The predictive value of cerebrospinal fluid dynamic tests in patients with the idiopathic adult hydrocephalus syndrome'. In: *Archives of neurology* vol. 52, no. 8, pp. 783–789.

Mardal, K.-A. and Logg, A. (2021). *Lectures on the Finite Element Method*. eng. URL: https://kent-and.github.io/mek4250/book_jan13_2021.pdf.

Mardal, K.-A., Rognes, M. E. et al. (2022). *Mathematical Modeling of the Human Brain: From Magnetic Resonance Images to Finite Element Simulation*.

Mehta, P. D. et al. (2000). 'Plasma and cerebrospinal fluid levels of amyloid β proteins 1-40 and 1-42 in Alzheimer disease'. In: *Archives of neurology* vol. 57, no. 1, pp. 100–105.

Merlini, M., Wanner, D. and Nitsch, R. M. (2016). 'Tau pathology-dependent remodelling of cerebral arteries precedes Alzheimer's disease-related mi-

crovascular cerebral amyloid angiopathy'. In: *Acta neuropathologica* vol. 131, no. 5, pp. 737–752.
Mestre, H. et al. (2018). 'Flow of cerebrospinal fluid is driven by arterial pulsations and is reduced in hypertension'. eng. In: *Nature communications* vol. 9, no. 1, pp. 4878–4878.
Mládek, A. et al. (2022). 'Prediction of Shunt Responsiveness in Suspected Patients With Normal Pressure Hydrocephalus Using the Lumbar Infusion Test: A Machine Learning Approach'. In: *Neurosurgery* vol. 90, no. 4, pp. 407–418.
Paulson, O., Strandgaard, S. and Edvinsson, L. (1990). 'Cerebral autoregulation.' In: *Cerebrovascular and brain metabolism reviews* vol. 2, no. 2, pp. 161–192.
Payne, S. (2016). *Cerebral autoregulation: control of blood flow in the brain*. Springer.
Penn, R. D. and Linninger, A. (2009). 'The physics of hydrocephalus'. In: *Pediatric neurosurgery* vol. 45, no. 3, pp. 161–174.
Penta, R. and Ambrosi, D. (2015). 'The role of the microvascular tortuosity in tumor transport phenomena'. In: *Journal of theoretical biology* vol. 364, pp. 80–97.
Perles-Barbacaru, A. T. and Lahrech, H. (2007). 'A New Magnetic Resonance Imaging Method for Mapping the Cerebral Blood Volume Fraction: The Rapid Steady-State T 1 Method'. In: *Journal of Cerebral Blood Flow & Metabolism* vol. 27, no. 3, pp. 618–631.
Peterson, K. A. et al. (2016). 'The effect of shunt surgery on neuropsychological performance in normal pressure hydrocephalus: a systematic review and meta-analysis'. eng. In: *Journal of neurology* vol. 263, no. 8, pp. 1669–1677.
Pizzo, M. E. et al. (2018). 'Intrathecal antibody distribution in the rat brain: surface diffusion, perivascular transport and osmotic enhancement of delivery'. In: *The Journal of physiology* vol. 596, no. 3, pp. 445–475.
Qvarlander, S. et al. (2017). 'Cerebrospinal fluid and blood flow patterns in idiopathic normal pressure hydrocephalus'. In: *Acta neurologica Scandinavica* vol. 135, no. 5, pp. 576–584.
Raghunandan, A. et al. (2021). 'Bulk flow of cerebrospinal fluid observed in periarterial spaces is not an artifact of injection'. eng. In: *eLife* vol. 10.
Ray, L., Iliff, J. J. and Heys, J. J. (2019). 'Analysis of convective and diffusive transport in the brain interstitium'. In: *Fluids and Barriers of the CNS* vol. 16, no. 1, pp. 1–18.
Relkin, N. et al. (2005). 'Diagnosing idiopathic normal-pressure hydrocephalus'. In: *Neurosurgery* vol. 57, no. suppl_3, S2–4.
Ringstad, G. et al. (2018). 'Brain-wide glymphatic enhancement and clearance in humans assessed with MRI'. eng. In: *JCI insight* vol. 3, no. 13.
Ryding, E., Kahlon, B. and Reinstrup, P. (2018). 'Improved lumbar infusion test analysis for normal pressure hydrocephalus diagnosis'. eng. In: *Brain and behavior* vol. 8, no. 11, e01125–n/a.
Scollato, A. et al. (2008). 'Changes in aqueductal CSF stroke volume and progression of symptoms in patients with unshunted idiopathic normal pressure hydrocephalus'. In: *American journal of neuroradiology* vol. 29, no. 1, pp. 192–197.
Shipley, R. J. et al. (2020). 'A four-compartment multiscale model of fluid and drug distribution in vascular tumours'. In: *International Journal for Numerical Methods in Biomedical Engineering* vol. 36, no. 3, e3315.

Sobey, I. et al. (2010). 'Multi-fluid poro-elastic modelling of the CSF infusion test'. In: pp. 362–365.

Sobey, I. et al. (2012). 'Simulation of cerebral infusion tests using a poroelastic model'. In: *Int. J. Numer. Anal. Model., Ser. B* vol. 3, pp. 52–64.

Thavarajasingam, S. G. et al. (2021). 'Clinical predictors of shunt response in the diagnosis and treatment of idiopathic normal pressure hydrocephalus: a systematic review and meta-analysis'. eng. In: *Acta neurochirurgica* vol. 163, no. 10, pp. 2641–2672.

Thrane, V. R. et al. (2013). 'Paravascular microcirculation facilitates rapid lipid transport and astrocyte signaling in the brain'. In: *Scientific reports* vol. 3, no. 1, pp. 1–5.

Tithof, J. et al. (2022). 'A network model of glymphatic flow under different experimentally-motivated parametric scenarios'. In: *iScience*, p. 104258.

Toma, A. K. et al. (2013). 'Systematic review of the outcome of shunt surgery in idiopathic normal-pressure hydrocephalus'. In: *Acta neurochirurgica* vol. 155, no. 10, pp. 1977–1980.

Tournier, J.-D., Mori, S. and Leemans, A. (2011). 'Diffusion tensor imaging and beyond'. In: *Magnetic resonance in medicine* vol. 65, no. 6, p. 1532.

Tripathi, M. and Vibha, D. (2009). 'Reversible dementias'. In: *Indian journal of psychiatry* vol. 51, no. Suppl1, S52.

Tully, B. and Ventikos, Y. (2011). 'Cerebral water transport using multiple-network poroelastic theory: application to normal pressure hydrocephalus'. eng. In: *Journal of fluid mechanics* vol. 667, pp. 188–215.

Vallet, A. et al. (2020). 'Biomechanical response of the CNS is associated with frailty in NPH-suspected patients'. In: *Journal of Neurology* vol. 267, no. 5, pp. 1389–1400.

Valnes, L.-M. and Schreiner, J. (2021). *SVMTK*. URL: https://github.com/SVMTK/SVMTK (visited on 01/06/2021).

Vanneste, J. et al. (1992). 'Shunting Normal-Pressure Hydrocephalus - Do the Benefits Outweigh the Risks - A Multicenter Study And Literature-Review'. eng. In: *Neurology* vol. 42, no. 1, pp. 54–59.

Vinje, V. et al. (2020). 'Intracranial pressure elevation alters CSF clearance pathways'. eng. In: *Fluids and barriers of the CNS* vol. 17, no. 1, pp. 29–29.

Wang, Z. et al. (2020). 'Pathogenesis and pathophysiology of idiopathic normal pressure hydrocephalus'. In: *CNS neuroscience & therapeutics* vol. 26, no. 12, pp. 1230–1240.

Williams, M. A. et al. (2022). 'Safety and effectiveness of the assessment and treatment of idiopathic normal pressure hydrocephalus in the Adult Hydrocephalus Clinical Research Network'. In: *Journal of Neurosurgery* vol. 1, no. aop, pp. 1–13.

Winkler, A. M. et al. (2010). 'Cortical thickness or grey matter volume? The importance of selecting the phenotype for imaging genetics studies'. In: *Neuroimage* vol. 53, no. 3, pp. 1135–1146.

Xie, L. et al. (2013). 'Sleep Drives Metabolite Clearance from the Adult Brain'. eng. In: *Science (American Association for the Advancement of Science)* vol. 342, no. 6156, pp. 373–377.

Zagzoule, M. and Marc-Vergnes, J.-P. (1986). 'A global mathematical model of the cerebral circulation in man'. In: *Journal of biomechanics* vol. 19, no. 12, pp. 1015–1022.

Zhao, W. and Ji, S. (2019). 'White matter anisotropy for impact simulation and response sampling in traumatic brain injury'. In: *Journal of neurotrauma* vol. 36, no. 2, pp. 250–263.